Department Chemie
Fachgebiet Theoretische Chemie
Technische Universität München

PARAGAUSS — A Parallel Implementation of the Density Functional Method: Symmetrized and Open-Shell Variants of the TDDFT Method and Application to Optical Spectra of Adsorbed Metal Species

Sergey Bosko

Vollständiger Abdruck der von der Fakultät für Chemie der Technischen Universität München zur Erlangung des akademischen Grades eines

Doktors der Naturwissenschaften (Dr. rer. nat.)

genehmigten Dissertation.

Vorsitzender:	Univ.-Prof. Dr. U. K. Heiz
Prüfer der Dissertation:	
1.	Univ.-Prof. Dr. N. Rösch
2.	Univ.-Prof. Dr. M. Kleber

Die Dissertation wurde am 30.11.2007 bei der Technischen Universität München eingereicht und durch die Fakultät für Chemie am 09.01.2008 angenommen.

Thanks

I would like to thank Professor Notker Rösch, Alexey Matveev, Lyudmila Moskaleva and Sven Krüger.

Also I would like to thank my friends and colleagues: Ajanta and Ramesh Deka, Alena Kremleva, Elena and Aleksey Shor, Alexander Genest, Florian Schlosser, Alexander Voityuk, Amjad Mohammed Basha, Chuenchit Bussai, Anela Ivanova, Chan Intam, Siham Naima Derrar, Egor Vladimirov, Georgi Vayssilov, Grigoriy Shamov, Hristiyan Aleksandrov, Konstantin Neyman, Kok Hwa Lim, Manuela Metzner, Miquel Huix i Rotllant, Jevgeni Starikow, Vladimir Nasluzov, Petko Petkov, Qiao Sun, Viktor Vysotskiy, Raghunathan Ramakrishnan, Rupashree Shyama Ray, Shane Parker, Dmitrii Ganyushin, Guoming Xiong, Khatcharin Siriwong, Mathias Winkler, Olga Zakharieva, Parawan Chuichay, Grzegorz Jezierski, Zhaoxu Chen.

I thank my parents and my brother for everything.

I dedicate this thesis to all people who are very important for me and who support me with love and understand, who believe in me.

Contents

List of Abbreviations

a.u.	atomic units
ALDA	adiabatic local density approximation
CPKS	coupled perturbed Kohn–Sham
DF	density functional
DFT	density functional theory
HF	Hartree–Fock
HOMO	highest occupied molecular orbital
KS	Kohn–Sham
LCGTO	linear combination of Gaussian type orbitals
LDA	local density approximation
GGA	generalized gradients approximation
LUMO	lowest unoccupied molecular orbital
MO	molecular orbital
RI	resolution of the identity
SCF	self consistent field
TDHF	time-dependent Hartree–Fock
TDDFT	time-dependent density functional theory
TDLDA	time-dependent local density approximation
XC	aexchange-correlation
irrep	irreducible representation

List of Symbols

$\hat{A}$, $\hat{a}$	many-electron operator, one-electron operator
$A([f(x)]; x, y)$	A is a functional of $f(x)$ and a function of x, y
$\boldsymbol{r}$	space (position) vector
$\sigma = \uparrow, \downarrow$	spin coordinates
$\hat{T}$	operator of the kinetic energy of the electrons
$\hat{Q}$	electron-electron Coulomb interaction
v_{KS}	KS potential
$\Psi(t)$	general time-dependent N-electron wave function
$\Psi^{(0)}$	general time-independent wave function
E	energy of the system in state $\Psi^{(0)}$
$\varphi_q(\boldsymbol{r}), \varphi_{q\sigma}(\boldsymbol{r})$	q-th KS orbital, q-th KS spin-orbital
ϵ_q	energy of the KS orbital $\varphi_q(\boldsymbol{r})$
$\boldsymbol{E}(t)$	electric field amplitude vector and its absolute value
$\hat{H}^{(0)}$	0th order Hamiltonian operator
$\hat{H}^{(1)}$	1st order Hamiltonian operator
$V(t)$, $v(t)$	time-dependent external many/one-electron potential
ρ	electron density of the system
i, j, k	indices denoting cartesian coordinate directions x, y, z
a	indices denoting occupied KS orbitals
s	indices denoting unoccupied KS orbitals
q, q'	indices denoting general (occupied and unoccupied) KS orbitals

Chapter 1

Introduction

The investigation of optical spectra of molecules and nanoparticles is very useful for characterizing a variety of systems that are of importance for a wide range of applications, like optical and electronic devices, optical data storage, biosensors, magnetism. A particularly challenging field of timely interest is the investigation and interpretation of optical properties of nanosystems [1–4].

Optical transitions of metal clusters provide characteristic signatures that can be exploited in experimental characterization techniques. In addition, recognition of the potential of optical properties of metal nanoclusters for the design of new materials with desired optical response is growing [5]. Such systems may be used in tagging and anticounterfeiting (or "labeling") technology, plasmonics, optical communications, and optical information processing [6]. Therefore, detailed information about the optical spectra of metal particles is of strong interest for practical applications.

The theoretical investigation of the optical spectra of molecules and nanoparticles is a very complex task, which has become feasible due to methods based on Time-Dependent Density Functional Theory (TDDFT) [7–10].

TDDFT extends the ideas of ground state of Density Functional Theory (DFT) to the treatment of excitations and more general time-dependent phenomena. The fundamental variable of TDDFT is the density $\rho(\boldsymbol{r}, t)$ of electrons which varies in time t and space $\boldsymbol{r}$. The standard way to obtain the density is with the help of a fictitious system of non-interacting electrons, the Kohn-Sham (KS) system. These electrons move in an effective potential: the time-dependent Kohn-Sham potential. The exact form of this potential is unknown and therefore has to be approximated.

The response approach to time-dependent density-functional theory [7, 11] is formally based on the application of time-dependent perturbation theory. Perturbation theory allows one to calculate so-called response properties that are of a certain order k in the strength of an applied time-dependent external electric field $\boldsymbol{E}(t)$. Usually only an electric field is considered, which may be a superposition of more contributions that are periodic in time (monochromatic fields). Each contribution is characterized by a certain frequency ω and can be visualized as the electric field of an "ideal laser light".

If an electronic system, e.g. an atom or a molecule, is perturbed by such electric field, then the electron density $\rho(\boldsymbol{r}, t)$ of the system is "deformed": the system responds to the perturbation. Ultimately, the TDDFT response formalism results in the so-called Coupled Perturbed Kohn-Sham (CPKS) equations [12] of order k which completely determine the k-th order density response of the electronic system to the external electric field.

The first-order electron density response can be used to calculate singlet–singlet and singlet–triplet excitation energies as well as components $\alpha_{ij}(\omega)$ of the dynamic, frequency-dependent polarizability tensor. In the TDDFT response formalism, the calculation can be done with help of the first-order CPKS equation.

In this thesis, the implementation of the TDDFT module of the program package PARAGAUSS is presented. In the course of this work, a previously separate TDDFT module [11] was significantly augmented in several ways.

First, common gradient-corrected exchange-correlation functionals (GGA XC) have been added: Becke-Perdew (BP) [13,14], Perdew-Wang (PW91) [15,16], and functionals derived from the Perdew-Burke-Ernzernhof (PBE) functional [17–19], significantly extending the options beyond previously available functionals that represented various types of local density approximations (LDA), such as X_α [20] and Vosko-Wilk-Nusair LDA (VWN) [21]. Second, the TDDFT module was also extended to permit treatment of open-shell systems (spin-unrestricted formalism).

The previously implemented algorithm [11] for evaluating matrix elements of the exchange-correlation contribution to the response kernel invokes the resolution of the identity (RI). In several applications we found this procedure to be not reliable. Therefore, third, we implemented a direct numerical integration for the matrix elements in question which resulted in a numerically more stable and accurate procedure.

The density functional program PARAGAUSS [22] makes full use of molecular symmetry [23–25]. Symmetry constraints for more than 70 point groups can be exploited in SCF calculations. In this spirit, forth, the symmetry adaptation was also introduced for the TDDFT module, in each step of the response calculation: evaluation of Coulomb and exchange-correlation kernels, solution of the Casida eigenvalue problem, and evaluation of the dipole oscillator strengths. The use of symmetry in TDDFT calculations of transition energies and oscillator strengths resulted in significant time savings, reducing the computational costs by factors of two to ten. Moreover, the labels of irreducible representations allow an easier interpretation of results and they facilitate the correct assignment of spectral lines. Thus far, only few DFT programs fully exploit the advantages of symmetry in TDDFT calculations, e.g. Amsterdam Density Functional Code ADF [26], TurboMole [27].

Fifth, and finally, we introduced an option to reduce the active space of the particle-hole excitations in the response calculations and to exclude core electron levels. We were able to demonstrate that with a judicious reduction of the active space it is possi-

ble to achieve sufficiently accurate results for valence excitations at a fraction of the cost. A practical method for computing such transition energies was obtained by removing core electron levels from the active space. We also studied conditions for choosing optimal orbital and auxiliary basis sets in the response calculations.

All new features were developed targeting parallel computers and employing efficient parallel algorithms. The correctness and performance of the new TDDFT module was tested on a variety of well studied systems, mainly involving small coinage metal clusters. The results were compared with published data [28,29].

The following three chapters represent the body of this thesis. In Chapter 2, the formalism of TDDFT is briefly sketched together with aspects of symmetrization of response calculations. Chapter 3 describes the implementation of all new features as listed above in the TDDFT module of the density functional program PARAGAUSS. Chapter 4 presents an application of the newly developed TDDFT tool. Results for the electronic spectra of coinage metal atoms and dimers in the gas phase are compared to the spectra when these systems are adsorbed at regular and defect sites of MgO(001). This systematic evaluation of the optical absorption spectra extends earlier adsorption studies of our group [30–34]. Finally, Chapter 5 provides a summary of the thesis and an outlook.

Chapter 2

The formalism of time-dependent Density Functional Theory

2.1 The time-dependent Schrödinger equation

In spectroscopy, the starting point is a system in some stationary state, which then is exposed to electromagnetic radiation (light). Then one records whether the system undergoes a transition to another stationary state. Radiation induces a time-dependent potential energy term $\hat{H}_1(t)$ in the Hamiltonian. Therefore, one has to resort to the time-dependent Schrödinger equation. The most convenient approach is an approximate solution of the time-dependent equations by means of the time-dependent perturbation theory [35].

Let the system be described by the time-independent Hamiltonian $\hat{H}^{(0)}$ in absence of radiation (or other time-depen dent perturbations), and let $\hat{H}^{(1)}(t)$ be the time-dependent perturbation. The time-independent Schrödinger equation for the unperturbed problem is

$$\hat{H}^{(0)}\Psi^{(0)} = E\Psi^{(0)} \tag{2.1}$$

where $\Psi^{(0)}$ is the wave function of a stationary state and E the corresponding energy. If the electronic system is subject to an external, time-dependent perturbation $\hat{H}^{(1)}(t)$ switched on at a time t_0, we can describe the system by a time-dependent wave function $\Psi(t)$ which is the solution of the time-dependent Schrödinger equation

$$i\frac{\partial}{\partial t}\Psi(t) = \left[\hat{H}^{(0)} + \hat{H}^{(1)}(t)\right]\Psi(t) \tag{2.2}$$

The many-electron time-independent Hamiltonian $\hat{H}^{(0)}$ is

$$\hat{H}^{(0)} = \hat{T} + \hat{Q} + \hat{V}_{eN}. \tag{2.3}$$

It contains the kinetic energy operator $\hat{T}$ of the N_e electrons, the operator $\hat{Q}$ is the electrostatic Coulomb interaction, and the operator $\hat{V}_{eN}$ which is the potential of the

interaction with the electrostatic field of the N_N nuclear charges Z_A at location $\boldsymbol{R}_A$:

$$\hat{T} = -\frac{1}{2}\sum_{n=1}^{N_e}\boldsymbol{\nabla}_n^2, \quad \hat{Q} = \sum_{n<m}^{N_e}\frac{1}{|\boldsymbol{r}_n - \boldsymbol{r}_m|}, \quad \hat{V}_{eN} = -\sum_{n=1}^{N_e}\sum_{A=1}^{N_N}\frac{Z_A}{|\boldsymbol{r}_n - \boldsymbol{R}_A|}. \tag{2.4}$$

Here, $\boldsymbol{r}_n$ and $\boldsymbol{r}_m$ are the coordinates of the electrons n and m and $\boldsymbol{\nabla}_n^2$ is the square of the nabla operator acting on coordinates of electron n. Hartree atomic units are used here and in the following.

According to perturbation theory, if the perturbation $\hat{H}^{(1)}(t)$ is sufficiently weak, we can write the time-dependent wave function $\Psi(t)$ as a series of contributions $\Psi^{(l)}$ of order l:

$$\Psi(t) = \sum_{l=0}^{\infty}\Psi^{(l)}(t), \tag{2.5}$$

where the first term $\Psi^{(0)}$ is an arbitrary, stationary many-electron state of the unperturbed system at $t = t_0$, typically an eigenfunction of $\hat{H}^{(0)}$.

Now we will introduce some basic equations to develop the TDDFT formalism. Measurable quantities accessible in experiments, observables B are calculated as *expectation values* of the corresponding quantum mechanical operators $\hat{B}$. For the unperturbed system one has:

$$B^{(0)} = \langle\Psi^{(0)}|\hat{B}|\Psi^{(0)}\rangle. \tag{2.6}$$

In order to investigate how the expectation value of observable values B changes with time in the perturbed system, it is useful to study the difference

$$\delta B(t) = \langle\Psi(t)|\hat{B}|\Psi(t)\rangle - \langle\Psi^{(0)}|\hat{B}|\Psi^{(0)}\rangle = \langle\Psi(t)|\hat{B}|\Psi(t)\rangle - B^{(0)} \tag{2.7}$$

which is known as the *response* of observable B to the external perturbation $\hat{H}_1$ and shows how the value $B(t)$ of the observable B deviates from the initial (ground state) value $B^{(0)}$.

Upon substitution of the wave function $\Psi(t)$ in Eq. (2.7) by the series for the perturbed wave function, Eq. (2.5), one obtain a series for the response of observable B:

$$\delta B(t) = B^{(1)}(t) + \ldots \tag{2.8}$$

with

$$B^{(1)}(t) = \langle\Psi^{(0)}|\hat{B}|\Psi^{(1)}\rangle + \langle\Psi^{(1)}|\hat{B}|\Psi^{(0)}\rangle, \tag{2.9}$$

The first term $B^{(1)}(t)$ is so-called first-order or linear response term. Second- and higher order terms describe the nonlinear response which has not addressed in this work.

We can use the first term of the response of the observable B, Eq. (2.9), to calculate the first-order response $\rho^{(1)}(\boldsymbol{r}, t)$ of density ρ. The response of the density is the key

quantity in the time-dependent density functional response theory

$$\rho^{(1)}(\boldsymbol{r},t) = \langle \Psi^{(0)}|\hat{\rho}|\Psi^{(1)}\rangle + \langle \Psi^{(1)}|\hat{\rho}|\Psi^{(0)}\rangle, \tag{2.10}$$

where the density operator is

$$\hat{\rho} = \sum_{n=1}^{N_e} \delta(\boldsymbol{r} - \boldsymbol{r}'_n). \tag{2.11}$$

2.2 Time-dependent perturbation theory

First we briefly recall the variation-of-constants approach for the treatment of time-dependent perturbations [36].

We assume that the perturbation Hamiltonian $\hat{H}^{(1)}(t)$ in the time-dependent Schrödinger equation, Eq. (2.2), is a bounded operator in the separable Hilbert space of the unperturbed Hamiltonian $\hat{H}^{(0)}$. We focus on the perturbation of a bound state. We also assume that the system at very early times $t \to -\infty$ was initially unperturbed. This unperturbed initial system can be described with the help of the normalized eigenfunction Φ_a, which can be obtain directly by solving the time-independent Schrödinger equation. Thus, the general requirement for the perturbation Hamiltonian $\hat{H}^{(1)}(t)$ is $\hat{H}^{(1)} \to 0$ for $t \to -\infty$.

According to variation-of-constants procedure [36], we start with a spectral expansion of the state eigenfunction $\Psi(t)$ in the complete series of solutions $\Phi_{q'}$ with the corresponding energies $E_{q'}$ of the time-independent Schrödinger equation for Hamiltonian $\hat{H}^{(0)}$:

$$\Psi(t) = \sum_{q'=0}^{\infty} b_{q'}(t)\Phi_{q'}e^{-iE_{q'}t}. \tag{2.12}$$

Inserting this spectral expansion into the time-dependent Schrödinger equation, Eq. (2.2), we obtain an exact equation of motion for the expansion coefficients $b_q(t)$

$$\frac{\partial b_q}{\partial t} = -i\sum_{q'=0}^{\infty} b_{q'}(t)\hat{H}^{(1)}_{qq'}(t)e^{-i\Delta_{qq'}t}, \tag{2.13}$$

where $\Delta_{qq'} = E_q - E_{q'}$, where E_q and $E_{q'}$ are the corresponding energies of the state eigenfunctions Φ_q and $\Phi_{q'}$ of the time-independent Schrödinger equation. The first integral of this equation is readily obtained as

$$b_q(t) = \delta_{qa} - i\int_{-\infty}^{t} dt' \sum_{q'=0}^{\infty} b_{q'}(t')\hat{H}^{(1)}_{qq'}(t')e^{i\Delta_{qq'}t'}. \tag{2.14}$$

for the initial condition $\Psi(t) \to \Phi_a$ for $t \to -\infty$.

We use the perturbation expansion

$$b_q(t) = \sum_{n=0}^{\infty} b_q^{(n)}(t) \tag{2.15}$$

with the requirements $b_q^{(0)}(t) = \delta_{qa}$ and $b_q^{(n)}(t \to -\infty) = 0$ for $n \neq 0$, which ensure that the chosen initial conditions can be satisfied independently of the strength of the perturbation. Finally, we obtain the coupled equations

$$\frac{\partial b_q^{(n)}}{\partial t} = -i \sum_{q'=0}^{\infty} b_{q'}^{(n-1)}(t) \hat{H}_{qq'}^{(1)}(t) e^{i\Delta_{qq'}t}. \tag{2.16}$$

$$b_q^{(n)}(t) = -i \int_{-\infty}^{t} dt' \sum_{q'=0}^{\infty} b_{q'}^{(n-1)}(t') \hat{H}_{qq'}^{(1)}(t') e^{i\Delta_{qq'}t'}. \tag{2.17}$$

The first two orders of this hierarchy of approximations to $b_q(t)$ read

$$b_q^{(0)}(t) = \delta_{qa}, \tag{2.18}$$

$$b_q^{(1)}(t) = -i \int_{-\infty}^{t} dt' \hat{H}_{qq'}^{(1)}(t') e^{i\Delta_{qq'}t'}, \tag{2.19}$$

For the wave function, Eq. (2.5), with help of Eq. (2.12), we can introduce the following perturbation expansion:

$$\Psi^{(l)}(t) = \sum_{q'=0}^{\infty} b_{q'}^{(l)}(t) \Phi_{q'} e^{-iE_{q'}t}. \tag{2.20}$$

For $l = 0$ and $l = 1$, in other words for the first two components of the perturbed function, we obtain

$$\Psi^{(0)}(t) = \Phi_a e^{-iE_{q'}t}, \tag{2.21}$$

$$\Psi^{(1)}(t) = \sum_{q'=0}^{\infty} b_{q'}^{(1)}(t) \Phi_{q'} e^{-iE_{q'}t}. \tag{2.22}$$

2.3 Dipole interaction with external electric fields

Next, we specify the external perturbation $\hat{H}^{(1)}(t)$. We apply a uniform electric field in the dipole approximation, in which the effect of the radiation is incorporated into the interaction term $\hat{H}^{(1)}(t)$ that is separated from all other contributions to the field-free molecular Hamiltonian $\hat{H}^{(0)}$.

We model the perturbation by a superposition of adiabatically switched on monochromatic electric fields and we choose the appropriate perturbation operator

as

$$\hat{H}^{(1)}(t) = \hat{\boldsymbol{\mu}} \cdot \boldsymbol{E}(t) = -\sum_{n=1}^{N_e} \boldsymbol{r}_n \cdot \boldsymbol{E}(t) \tag{2.23}$$

with

$$\boldsymbol{E}(t) = \frac{1}{2}\int_{-\infty}^{\infty} d\omega \boldsymbol{E}(\omega) e^{i\omega t} e^{\eta t}, \tag{2.24}$$

where the convergence factor $e^{\eta t}$ ensures that the perturbation is switched on adiabatically for $t \to -\infty$ in the appropriate limit of $\eta \to 0$. The factor $1/2$ accounts for the fact that the integration is also done over negative frequencies.

The perturbation Hamiltonian thus is a sum

$$\hat{H}^{(1)}(t) = \sum_{n=1}^{N_e} v(\boldsymbol{r}_n, t) \tag{2.25}$$

of one-electron operators

$$v(\boldsymbol{r}, t) = \frac{1}{2}\int_{-\infty}^{\infty} d\omega\, v(\boldsymbol{r}, \omega) e^{i\omega t} e^{\eta t} \tag{2.26}$$

with

$$v(\boldsymbol{r}, \omega) = -\boldsymbol{r} \cdot \boldsymbol{E}(\omega) \tag{2.27}$$

Ultimately, we want to treat linear optical phenomena which arise from the interaction of multiple monochromatic fields

$$\boldsymbol{E}(t) = \sum_l \boldsymbol{E}(\omega_l) \cos(\omega_l t). \tag{2.28}$$

We now substitute in the general time-dependent perturbation expressions the electric perturbation for the perturbation Hamiltonian $\hat{H}^{(1)}(t)$, taking into account that $\Delta_{qq'} = E_q - E_{q'}$.

$$b_q^{(0)}(t) = \delta_{qq'}, \tag{2.29}$$

$$b_q^{(1)}(t) = -\frac{1}{2}\int d\omega \frac{V_{qq'}(\omega)}{\Delta_{qq'} + (\omega - i\eta)} \exp\left[i(\Delta_{qq'} + \omega - i\eta)t\right], \tag{2.30}$$

Here we have introduced the abbreviation

$$V_{qq'} = \langle \Phi_q | \sum_{n=1}^{N_e} v(\boldsymbol{r}_n, \omega) | \Phi_{q'} \rangle \tag{2.31}$$

for the perturbation amplitudes.

2.4 Systems of non-interacting electrons in external electric fields

The final expression for the density response

$$\rho^{(1)}(\boldsymbol{r},t) = \langle \Psi^{(0)}|\hat{\rho}|\Psi^{(1)}\rangle + \langle \Psi^{(1)}|\hat{\rho}|\Psi^{(0)}\rangle \tag{2.32}$$

holds for a Kohn–Sham system of N_e non-interacting electrons. Under the influence of a single-particle potential $v(\boldsymbol{r}_i)$, such a system is described by the Hamiltonian operator

$$\hat{H}^{(0)}_{\mathrm{KS}} = \sum_{n=1}^{N_e} \left(-\frac{1}{2}\boldsymbol{\nabla}_n^2 + v(\boldsymbol{r}_n) \right), \tag{2.33}$$

which is the sum of one-electron contributions. The time-independent many-electron Schrödinger equation reduces to equivalent one-electron equations:

$$\left[-\frac{1}{2}\boldsymbol{\nabla}^2 + v(\boldsymbol{r}) \right] \varphi_n(\boldsymbol{r}) = \epsilon_n \varphi_n(\boldsymbol{r}) \tag{2.34}$$

The solutions Φ for such a system can be taken as Slater determinants constructed from the N_e occupied one-electron orbitals φ_a satisfying Eq. (2.34):

$$\Phi = \frac{1}{\sqrt{N_e!}} \det \left| \varphi_1(\boldsymbol{r}_1)\varphi_2(\boldsymbol{r}_2)...\varphi_{N_e}(\boldsymbol{r}_{N_e}) \right|. \tag{2.35}$$

For the remainder of this thesis the indices a are used for occupied one-electron orbitals, indices s used for unoccupied one-electron orbitals, and q, q' denote general, i.e. many-electronic wave functions.

In this section we assume a closed-shell system for which we now have to obtain the response of the density. The simplest approach is to apply time-dependent perturbation theory directly at the level of the one-electron orbitals $\varphi_n(\boldsymbol{r})$. All many-electron operators are replaced by the corresponding one-electron operators, and a sum over the occupied one-electron wave functions $\varphi_a(\boldsymbol{r})$ and a sum over the unoccupied one-electron levels $\varphi_s(\boldsymbol{r})$.

Now we recall expression Eq. (2.32) for $\rho^{(1)}(t)$. With the help of the formulae for $\Psi^{(0)}$, Eq. (2.21), and $\Psi^{(1)}$, Eq. (2.22), the first part of Eq. (2.32) can be rearranged as

$$\langle \Psi^{(0)}|\hat{\rho}|\Psi^{(1)}\rangle = \sum_{q=0}^{\infty} b_q^{(1)}(t)\langle \Phi_a|\hat{\rho}|\Phi_q\rangle e^{i\Delta_{aq}t}, \tag{2.36}$$

where $\Delta_{aq} = E_a - E_q$ **,** here we recall, that Φ_a and Φ_q are the eigenstate functions of the time-independent system and E_a and E_q are the energies of those corresponding states. With help of Eq. (2.30) for $b_q^{(1)}$ we obtain for the first-order perturbation due to

an electric field:

$$\langle \Psi^{(0)}|\hat{\rho}|\Psi^{(1)}\rangle = -\frac{1}{2}\sum_{q=0}^{\infty}\rho_{aq}(\boldsymbol{r})\int d\omega \frac{V_{qa}(\omega)}{\Delta_{qa}+(\omega-i\eta)}e^{i(\omega-i\eta)t}, \tag{2.37}$$

where $\rho_{aq} = \langle\Phi_a|\hat{\rho}|\Phi_q\rangle$, and $\Delta_{qa} = -\Delta_{aq}$. The perturbation amplitude $V_{qa}(\omega)$ is given by Eq. (2.31).

Exploiting the hermiticity condition $v^{\dagger}(\omega) = v(-\omega)$, we find for the Hermitian conjugate of Eq. (2.37) in analogous fashion

$$\langle \Psi^{(1)}|\hat{\rho}|\Psi^{(0)}\rangle = -\frac{1}{2}\sum_{q=0}^{\infty}\rho_{qa}(\boldsymbol{r})\int d\omega \frac{V_{aq}(-\omega)}{\Delta_{qa}+(\omega+i\eta)}e^{-i(\omega+i\eta)t} \tag{2.38}$$

where we used the fact that one has for the matrix element of the perturbation potential:

$$V^{*}_{qa}(\omega) = \langle\Phi_a|\sum_{n=1}^{N_e} v^{\dagger}(\boldsymbol{r}_n,\omega)|\Phi_q\rangle = \langle\Phi_a|\sum_{n=1}^{N_e} v(\boldsymbol{r}_n,-\omega)|\Phi_q\rangle = V_{aq}(-\omega) \tag{2.39}$$

Finally, the first-order density response is obtained as

$$\rho^{(1)}(\boldsymbol{r},t) = -\frac{1}{2}e^{\eta t}\sum_{q=0}^{\infty}\int d\omega \left\{\frac{\rho_{aq}V_{qa}(\omega)}{\Delta_{qa}+(\omega-i\eta)} + \frac{\rho_{qa}V_{aq}(\omega)}{\Delta_{qa}-(\omega-i\eta)}\right\}e^{i\omega t}, \tag{2.40}$$

where in the last step $-\omega$ has been substituted for ω in the second term. By substituting the Slater determinants, Eq. (2.35), into the first-order density response, Eq. (2.40), and applying perturbation theory directly at the level of the one-electron orbitals, we finally obtain the following equation for the response of the density:

$$\rho^{(1)}(\boldsymbol{r},t) = -e^{\eta t}\sum_{a}^{\text{occ}}\sum_{s}^{\text{unocc}}\int d\omega \left\{\frac{\rho_{as}(\boldsymbol{r})v_{sa}(\omega)}{\Delta_{sa}+(\omega-i\eta)} + \frac{\rho_{sa}(\boldsymbol{r})v_{as}(\omega)}{\Delta_{sa}-(\omega-i\eta)}\right\}e^{i\omega t}. \tag{2.41}$$

Here we had assumed for simplicity that our system has a closed-shell electronic structure. Note, that in the last equation for the response of the density, Eq. (2.41), all many-electron operators are exchanged with the corresponding one-electron operators, and a sum over occupied one-electron orbitals φ_a is used instead of the initial many electron wave function Φ_a. In this context of one-electron wave functions the quantities $\Delta_{sa} = \epsilon_s - \epsilon_a$ are differences of one-electron eigenvalues, ϵ_a designating Kohn–Sham energies of occupied levels and ϵ_s Kohn–Sham energies of unoccupied levels, and the density amplitudes $\rho_{as}(\boldsymbol{r})$ can be rewritten as

$$\rho_{as}(\boldsymbol{r}) = \langle\varphi_a|\varphi_s\rangle = \varphi^{*}_a(\boldsymbol{r})\varphi_s(\boldsymbol{r}), \tag{2.42}$$

where we used $\hat{\rho} = \sum_{n=1}^{N_e}\delta(\boldsymbol{r}-\boldsymbol{r}'_n)$. The potential due to a perturbation by a superpo-

sition of monochromatic electric fields is

$$v_{as}(\omega) = \langle \varphi_a | \hat{\boldsymbol{\mu}} \cdot \boldsymbol{E}(\omega) | \varphi_s \rangle = - \sum_{j=x,y,z} E_j(\omega) \int d^3\boldsymbol{r} \varphi_a^*(\boldsymbol{r})\, r_j\, \varphi_s(\boldsymbol{r}). \tag{2.43}$$

Let us define the first-order density response function $\chi_{\mathrm{KS}}^{(1)}$ of the Kohn–Sham system of non-interacting electrons as

$$\chi_{\mathrm{KS}}^{(1)}(\boldsymbol{r}, \boldsymbol{r}', \omega, \eta) = \sum_{a}^{\mathrm{occ}} \sum_{s}^{\mathrm{unocc}} \frac{4\Delta_{sa}}{\Delta_{sa}^2 - (\omega - i\eta)^2} \varphi_a(\boldsymbol{r}) \varphi_s(\boldsymbol{r}) \varphi_a(\boldsymbol{r}') \varphi_s(\boldsymbol{r}'), \tag{2.44}$$

then one can rewrite Eq. (2.41) to read:

$$\rho^{(1)}(\boldsymbol{r}, t) = \sum_{j=x,y,z} \int d\omega \int d^3\boldsymbol{r}' \chi_s^{(1)}(\boldsymbol{r}, \boldsymbol{r}', \omega, \eta) r_j E_j(\omega) e^{i\omega t} \tag{2.45}$$

A variant of this formalism for open-shell systems can be found in Appendix A.

2.5 Time-dependent density functional theory

Time-dependent density functional theory is based on the Runge–Gross theorem. It establishes a one-to-one correspondence between the time-dependent density $\rho(\boldsymbol{r}, t)$ and the external potential $v(\boldsymbol{r}, t)$ [8]:

Densities $\rho(\boldsymbol{r}, t)$ and $\rho'(\boldsymbol{r}, t)$ evolving from a common initial state $\Psi(t \longrightarrow -\infty) = \Phi$ under the influence of two potentials $v(\boldsymbol{r}, t)$ and $v'(\boldsymbol{r}, t)$ are always different, provided that the potentials differ by more than a purely time-dependent function (independent of $\boldsymbol{r}$):

$$v(\boldsymbol{r}, t) \neq v'(\boldsymbol{r}, t) + c(t) \tag{2.46}$$

With such a one-to-one correspondence between density $\rho(\boldsymbol{r}, t)$ and external potential $v(\boldsymbol{r}, t)$, one can proceed to a time-dependent generalization of the Kohn–Sham scheme [37] for our given, interacting many-electron system. For this, one needs further assumptions. First, one has to assume v-representability for the density $\rho(\boldsymbol{r}, t)$ of this interacting many-electron system [10], i.e., one assumes that a time-dependent one-electron potential $v_{\mathrm{KS}}(\boldsymbol{r}, t)$ exists, which, if acting on a system of non-interacting electrons, creates a density that equals $\rho(\boldsymbol{r}, t)$. Such a system will be referred to as Kohn–Sham system in the following, and the potential $v_{\mathrm{KS}}(\boldsymbol{r}, t)$ as Kohn–Sham potential. According to the Runge–Gross theorem, $v_{\mathrm{KS}}(\boldsymbol{r}, t)$ is unique [8]. The corresponding Kohn–Sham equation is

$$i\frac{\partial}{\partial t}\varphi_n(\boldsymbol{r}, t) = \left(-\frac{1}{2}\boldsymbol{\nabla}^2 + v_{\mathrm{KS}}([\rho]\,; \boldsymbol{r}, t) \right) \varphi_n(\boldsymbol{r}, t). \tag{2.47}$$

The density of the Kohn–Sham reference system of the non-interacting electrons is

$$\rho(\boldsymbol{r},t) = \sum_{n=1}^{N_e} |\varphi_n(\boldsymbol{r},t)|^2 . \tag{2.48}$$

It is advantageous to separate the one-electron potential $v_{\mathrm{KS}}(\boldsymbol{r},t)$ into three major contributions [7]:

$$v_{\mathrm{KS}}([\rho]\,;\boldsymbol{r},t) = v(\boldsymbol{r},t) + u(\boldsymbol{r},t) + v_{\mathrm{XC}}([\rho]\,;\boldsymbol{r},t). \tag{2.49}$$

Here, $v(\boldsymbol{r},t)$ is the external potential acting on the interacting physical system. It is augmented by the Coulomb potential of the total density:

$$u(\boldsymbol{r},t) = \int d^3r' \frac{\rho(\boldsymbol{r}',t)}{|\boldsymbol{r}-\boldsymbol{r}'|}, \tag{2.50}$$

and the, in general, unknown exchange-correlation potential $v_{\mathrm{XC}}([\rho]\,;\boldsymbol{r},t)$.

2.6 Application of response theory to TDDFT

An important class of molecular response properties, e.g., excitation energies, is completely determined once the density response of the corresponding order is known. As above, see Sec. 2.4, we consider a system under the influence of a time-dependent electric field, that is switched on adiabatically. The density $\rho(\boldsymbol{r},t)$ of such a system is time-dependent. According to the Runge–Gross theorem, we can make a functional Taylor expansion of $\rho(\boldsymbol{r},t)$ with respect to the external potential $v(\boldsymbol{r},t)$:

$$\rho(\boldsymbol{r},t) = \rho^{(0)}(\boldsymbol{r}) + \rho^{(1)}(\boldsymbol{r},t) + \rho^{(2)}(\boldsymbol{r},t) + \ldots \tag{2.51}$$

Clearly $\rho^{(0)}(\boldsymbol{r})$ is the unperturbed ground state density and the function

$$\delta\rho(\boldsymbol{r},t) = \rho(\boldsymbol{r},t) - \rho^{(0)}(\boldsymbol{r}) \tag{2.52}$$

is the total density response. To simplify the notation in the following, we introduce space-time variables:

$$\boldsymbol{x} \equiv (\boldsymbol{r},t), \quad \boldsymbol{y} \equiv (\boldsymbol{r}',t'), \quad d^4\boldsymbol{x} = d^3\boldsymbol{r}d\boldsymbol{t}, \quad d^4\boldsymbol{y} = d^3\boldsymbol{r}'d\boldsymbol{t}'. \tag{2.53}$$

The first term of the density response series, Eq. (2.51), of the first-order in external-potential $v(\boldsymbol{x})$ is defined as the integral

$$\rho^{(1)}(\boldsymbol{x}) = \int d^4\boldsymbol{y}\chi^{(1)}(\boldsymbol{x},\boldsymbol{y})v(\boldsymbol{y}) \tag{2.54}$$

where we introduced the first-order density response function of the interacting many-electron system $\chi^{(1)}$. The response function is formally the first-order functional

derivative of the density with respect to the external potential:

$$\chi^{(1)}(\boldsymbol{x},\boldsymbol{y}) = \left.\frac{\delta\rho(\boldsymbol{x})}{\delta v(\boldsymbol{y})}\right|_{v^{(0)}} \tag{2.55}$$

Reflecting their definitions as functional derivatives, the density response functions $\chi^{(1)}(\boldsymbol{x},\boldsymbol{y})$ describe the change of the electronic density at $\boldsymbol{x}$ induced by the external perturbation potential v, at $\boldsymbol{y}$. The initial potential $v^{(0)} = v([\rho^{(0)}];\boldsymbol{r})$ is a functional of the unperturbed ground state density $\rho^{(0)}$.

The Runge–Gross theorem applies equally to the real system of interacting electrons as to the model Kohn–Sham system of non-interacting electrons. Therefore we can use the same algebra for the time-dependent system of the non-interacting Kohn–Sham system.

Thus, we now apply time-dependent perturbation theory, see Sec. 2.2, to the Kohn–Sham system of non-interacting electrons. The response of the density is

$$\delta\rho(\boldsymbol{x}) = \rho^{(1)}_{\mathrm{KS}}(\boldsymbol{x}) + \rho^{(2)}_{\mathrm{KS}}(\boldsymbol{x}) + \ldots \tag{2.56}$$

Here $\rho^{(l)}_{\mathrm{KS}}$ denotes the l-th order of the density response of the Kohn–Sham system with respect to the time-dependent part $v^{\mathrm{TD}}_{\mathrm{KS}}(\boldsymbol{x})$ of the Kohn–Sham potential, treated as perturbation of the time-independent initial potential. The first leading term of the density response is given by

$$\rho^{(1)}_{\mathrm{KS}}(\boldsymbol{x}) = \int d^4\boldsymbol{y}\chi^{(1)}_{\mathrm{KS}}(\boldsymbol{x},\boldsymbol{y})v^{\mathrm{TD}}_{\mathrm{KS}}(\boldsymbol{y}) \tag{2.57}$$

The first-order density response function of the Kohn–Sham system is formally the first-order functional derivative of the Kohn–Sham density with respect to the variation of the external potential:

$$\chi^{(1)}_{\mathrm{KS}}(\boldsymbol{x},\boldsymbol{y}) = \left.\frac{\delta\rho(\boldsymbol{x})}{\delta v^{\mathrm{TD}}_{\mathrm{KS}}(\boldsymbol{y})}\right|_{v_0} \tag{2.58}$$

The function $\chi^{(1)}_{\mathrm{KS}}$ describes how the density of the auxiliary Kohn–Sham system of non-interacting electrons changes, if the time-dependent perturbation $v^{\mathrm{TD}}_{\mathrm{KS}}$ is applied.

The perturbation $v^{\mathrm{TD}}_{\mathrm{KS}}$ of the external potential that acts on the ground state Kohn–Sham system can also be treated in the framework of response theory if one introduces as an expansion in the real perturbation of the external potential $v(\boldsymbol{x})$:

$$v^{\mathrm{TD}}_{\mathrm{KS}}(\boldsymbol{x}) = v_{\mathrm{KS}}(\boldsymbol{x}) - v^{(0)}_{\mathrm{KS}}(\boldsymbol{r}) = v^{(1)}_{\mathrm{KS}}(\boldsymbol{x}) + v^{(2)}_{\mathrm{KS}}(\boldsymbol{x}) + \ldots \tag{2.59}$$

Now we insert the time-dependent perturbation of the Kohn–Sham potential, Eq. (2.59), in the first leading term of the density response of the Kohn–Sham system, Eq.

(2.57), and obtain the expansion

$$\rho_{\mathrm{KS}}^{(1)}(\boldsymbol{x}) = \int d^4\boldsymbol{y}\, \chi_{\mathrm{KS}}^{(1)}(\boldsymbol{x},\boldsymbol{y}) v_{\mathrm{KS}}^{(1)}(\boldsymbol{y}) + \int d^4\boldsymbol{y}\, \chi_{\mathrm{KS}}^{(1)}(\boldsymbol{x},\boldsymbol{y}) v_{\mathrm{KS}}^{(2)}(\boldsymbol{y}) + \dots \tag{2.60}$$

The only term of first order in the equation of the Kohn–Sham density response, Eq. (2.60), is equivalent to the linear response of the density of the physical interacting system

$$\rho^{(1)}(\boldsymbol{x}) = \rho_{\mathrm{KS}}^{(1)}(\boldsymbol{x}). \tag{2.61}$$

Thus, the linear response of the physical interacting system can be expressed via properties of the Kohn–Sham system only:

$$\rho^{(1)}(\boldsymbol{x}) = \int d^4\boldsymbol{y}\, \chi_{\mathrm{KS}}^{(1)}(\boldsymbol{x},\boldsymbol{y}) v_{\mathrm{KS}}^{(1)}(\boldsymbol{y}). \tag{2.62}$$

From the functional Taylor expansion for the perturbation of the external potential, Eq. (2.59), the first-order response of the Kohn–Sham potential $v_{\mathrm{KS}}^{(1)}(\boldsymbol{x})$ is defined as the functional derivative of $v_{\mathrm{KS}}(\boldsymbol{x})$ with respect to the real, external perturbation $v(\boldsymbol{x})$:

$$v_{\mathrm{KS}}^{(1)}(\boldsymbol{x}) = \int d^4\boldsymbol{y}\, \frac{\delta v_{\mathrm{KS}}(\boldsymbol{x})}{\delta v(\boldsymbol{y})} v(\boldsymbol{y}). \tag{2.63}$$

Using the definition of the Kohn–Sham potential, Eq. (2.33),

$$v_{\mathrm{KS}}(\boldsymbol{x}) = v(\boldsymbol{x}) + v_{\mathrm{UXC}}(\boldsymbol{x}) = v(\boldsymbol{x}) + \int d^3\boldsymbol{r}' \frac{\rho(\boldsymbol{r}',t)}{|\boldsymbol{r}-\boldsymbol{r}'|} + v_{\mathrm{XC}}(\boldsymbol{x}), \tag{2.64}$$

the functional derivatives in Eq. (2.63) can be evaluated by means of the chain rule:

$$\begin{aligned} v_{\mathrm{KS}}^{(1)}(\boldsymbol{x}) &= \int d^4\boldsymbol{y} \left[\delta(\boldsymbol{x}-\boldsymbol{y}) + \int d^4\boldsymbol{y}' \frac{\delta v_{\mathrm{UXC}}(\boldsymbol{x})}{\delta\rho(\boldsymbol{y}')} \frac{\delta\rho(\boldsymbol{y}')}{\delta v(\boldsymbol{y})} \right] v(\boldsymbol{y}) \\ &= v(\boldsymbol{x}) + \int d^4\boldsymbol{y}' \frac{\delta v_{\mathrm{UXC}}(\boldsymbol{x})}{\delta\rho(\boldsymbol{y}')} \int d^4\boldsymbol{y} \frac{\delta\rho(\boldsymbol{y}')}{\delta v(\boldsymbol{y})} v(\boldsymbol{y}). \end{aligned} \tag{2.65}$$

In the last equation, the inner integral evaluates to the first-order density response $\rho^{(1)}(\boldsymbol{y})$ as given by Eqs. (2.54) and (2.55). For the functional derivative in the outer integral we introduce the time-dependent Coulomb-exchange-correlation kernel $f_{\mathrm{UXC}}(\boldsymbol{x},\boldsymbol{y})$:

$$f_{\mathrm{UXC}}(\boldsymbol{x},\boldsymbol{y}) = \frac{\delta v_{\mathrm{UXC}}(\boldsymbol{x})}{\delta\rho(\boldsymbol{y})} = \frac{1}{|\boldsymbol{r}-\boldsymbol{r}'|} + \frac{\delta v_{\mathrm{XC}}(\boldsymbol{x})}{\delta\rho(\boldsymbol{y})} = f_{\mathrm{U}} + f_{\mathrm{XC}} \tag{2.66}$$

Thus, for the first-order response of the Kohn–Sham potential we have arrived at a relation between the physical perturbation $v(\boldsymbol{x})$ and the first-order perturbation of the

Kohn–Sham potential $v_{\mathrm{KS}}^{(1)}(\boldsymbol{x})$:

$$v_{\mathrm{KS}}^{(1)}(\boldsymbol{x}) = v(\boldsymbol{x}) + \int d^4\boldsymbol{y}\, f_{\mathrm{UXC}}(\boldsymbol{x},\boldsymbol{y})\, \rho^{(1)}(\boldsymbol{y}). \tag{2.67}$$

Finally, the so-called coupled perturbed Kohn–Sham (CPKS) equations for the first-order density response $\rho^{(1)}$ arises if one combines Eqs. (2.62) and (2.67) into a single equation [11]:

$$\rho^{(1)}(\boldsymbol{x}) = \int d^4\boldsymbol{y}\, \chi_{\mathrm{KS}}^{(1)}(\boldsymbol{x},\boldsymbol{y}) \left(v(\boldsymbol{y}) + \int d^4\boldsymbol{y}' f_{\mathrm{UXC}}(\boldsymbol{y},\boldsymbol{y}')\rho^{(1)}(\boldsymbol{y}') \right). \tag{2.68}$$

Note that this is an integral equation for the density response $\rho^{(1)}(\boldsymbol{x})$ which appears both on the left-hand and the right-hand sides.

2.7 Properties of the exchange-correlation kernel

The response of a system at time t can only depend on the state of the system at times $t' < t$. The response of the system to an external perturbation must be independent of the point in time t_0, at which the perturbation was switched on. This follows from the invariance of the unperturbed system with respect to translation in time. The response function must be invariant with respect to temporal translations, and can therefore only depend on differences $t - t'$. These facts may be reflected in the integral expressions for the first-order density response of the Kohn–Sham- and the real systems, Eq. (2.62),

$$\rho^{(1)}(\boldsymbol{r},t) = \int d^3\boldsymbol{r}' \int dt' \chi_{\mathrm{KS}}^{(1)}(\boldsymbol{r},\boldsymbol{r}',t-t') v_{\mathrm{KS}}^{(1)}(\boldsymbol{r}',t')\theta(t-t'), \tag{2.69}$$

Here we have introduced the step function

$$\theta(t-t') = \begin{cases} 1 & t < t' \\ 0 & t \geq t' \end{cases}$$

to explicitly exclude the integration over "future" times $t' \geq t$.

An analogous argument holds for the response function of the Kohn–Sham potential $v_{\mathrm{KS}}^{(1)}$ regarding a density variation $\rho^{(1)}$, Eq. (2.67). Hence the response kernel must satisfy

$$f_{\mathrm{UXC}}(\boldsymbol{r},t,\boldsymbol{r}',t') = f_{\mathrm{UXC}}(\boldsymbol{r},\boldsymbol{r}',t-t')\theta(t-t'). \tag{2.70}$$

2.8 The coupled perturbed Kohn–Sham equation for the density response in the frequency domain

To derive the expression for the electronic excitation energies within the first-order response regime of TDDFT, we first derive the equivalent coupled perturbed Kohn–Sham equation (CPKS), Eq. (2.64), for the frequency-domain representation of the linear density response $\rho^{(1)}(\boldsymbol{r},\omega)$. In the following algebra we will omit the infinitesimal quantity η by setting it formally to zero.

First we introduce the Fourier transformation [38] of the first-order response density $\rho^{(1)}$,

$$\rho^{(1)}(\boldsymbol{r},t) = \int d\omega\, \rho^{(1)}(\boldsymbol{r},\omega) e^{i\omega t}, \tag{2.71}$$

of the first-order response function $\chi^{(1)}_{\mathrm{KS}}$,

$$\chi^{(1)}_{\mathrm{KS}}(\boldsymbol{r},\boldsymbol{r}',t-t')\theta(t-t') = \int d\omega\, \chi^{(1)}_{\mathrm{KS}}(\boldsymbol{r},\boldsymbol{r}',\omega) e^{i\omega(t-t')}, \tag{2.72}$$

and of the Coulomb-exchange-correlation kernel f_{UXC}:

$$f_{\mathrm{UXC}}(\boldsymbol{r},\boldsymbol{r}',t-t')\theta(t-t') = \int d\omega\, f_{\mathrm{UXC}}(\boldsymbol{r},\boldsymbol{r}',\omega) e^{i\omega(t-t')}. \tag{2.73}$$

Using these definitions we can express the CPKS equation in the frequency domain by substituting them into the time-dependent CPKS, Eq. (2.68), and integrating over time. This procedure yields the frequency-dependent form of the CPKS equation,

$$\rho^{(1)}(\boldsymbol{r},\omega) = \int d^3\boldsymbol{r}' \chi^{(1)}_{\mathrm{KS}}(\boldsymbol{r},\boldsymbol{r}',\omega) \left(v(\boldsymbol{r}',\omega) + \int d^3\boldsymbol{r}''\, f_{\mathrm{UXC}}(\boldsymbol{r}',\boldsymbol{r}'',\omega)\rho^{(1)}(\boldsymbol{r}'',\omega) \right), \tag{2.74}$$

that is to be compared with the time-dependent form of the response equation, Eq. (2.68). The corresponding simple form of time-dependent CPKS equation reads

$$\rho^{(1)} = \int d^3\boldsymbol{r}\, \chi^{(1)}_{\mathrm{KS}} \left(v + \int d^3\boldsymbol{r}'\, f_{\mathrm{UXC}}\, \rho^{(1)} \right) \tag{2.75}$$

2.9 The coupled perturbed Kohn–Sham equation in matrix form

Now we turn to the derivation of the matrix-based CPKS equation, starting from the frequency-dependent form of the CPKS equation, Eq. (2.74). We consider the density response of a system to an applied electric field $\rho^{(1)}(\boldsymbol{r},\omega)$; therefore, we can choose the KS orbitals φ_a and φ_s as real quantities. As we will also discuss open-shell systems, the spin index σ will be taken into account.

First we will introduce the function $\Phi_{as\sigma}$ as a product of occupied Kohn–Sham or-

bital $\varphi_{a\sigma}(\boldsymbol{r})$ and unoccupied Kohn–Sham orbital $\varphi_{s\sigma}(\boldsymbol{r})$:

$$\Phi_{as\sigma}(\boldsymbol{r}) = \varphi_{a\sigma}(\boldsymbol{r})\varphi_{s\sigma}(\boldsymbol{r}). \tag{2.76}$$

The linear response density $\rho^{(1)}(\boldsymbol{r},\omega)$ is expressed by products of the function $\Phi_{as\sigma}$ with coefficients $x_{as\sigma}(\omega)$

$$\rho^{(1)}(\boldsymbol{r},\omega) = \sum_{\sigma}^{\text{spin}} \sum_{a}^{\text{occ}} \sum_{s}^{\text{unocc}} x_{as\sigma}(\omega)\, \Phi_{as\sigma}(\boldsymbol{r}). \tag{2.77}$$

The first-order response function, Eq. (2.44), see also Appendix A, is an expansion over orbital products:

$$\chi^{(1)}_{\text{KS}}(\boldsymbol{r},\boldsymbol{r}',\omega) = \sum_{\sigma}^{\text{spin}} \sum_{a}^{\text{occ}} \sum_{s}^{\text{unocc}} \frac{2\Delta_{sa\sigma}}{\Delta^2_{sa\sigma} - \omega^2} \Phi_{as\sigma}(\boldsymbol{r})\Phi_{as\sigma}(\boldsymbol{r}'), \tag{2.78}$$

where $\Delta_{sa\sigma} = \epsilon_{s\sigma} - \epsilon_{a\sigma}$ is a difference of one-electron Kohn–Sham energies of occupied levels $\epsilon_{a\sigma}$ and one electron Kohn–Sham energies of unoccupied levels $\epsilon_{s\sigma}$. The external perturbation potential is represented in the finite basis by the matrix of coefficients:

$$v_{as\sigma}(\omega) = \int d^3\boldsymbol{r}'\, \Phi_{as\sigma}(\boldsymbol{r}')v(\boldsymbol{r}',\omega), \tag{2.79}$$

For the potential response kernel f_{UXC} we introduce the four-index matrix elements:

$$K_{as\sigma,a's'\sigma'} = \int d^3\boldsymbol{r} \int d^3\boldsymbol{r}'\, \Phi_{a's'\sigma'}(\boldsymbol{r}')\, f_{\text{UXC}}(\boldsymbol{r},\boldsymbol{r}',\omega)\, \Phi_{as\sigma}(\boldsymbol{r}), \tag{2.80}$$

With these basis set definitions of the linear response density, Eq. (2.77), the first-order response function, Eq. (2.78), the external perturbation potential, Eq. (2.79), and the potential response kernel f_{UXC}, Eq. (2.80), the CPKS equation in frequency dependent form, Eq. (2.75), may be cast into the linear equation:

$$x_{as\sigma} = \frac{2\Delta_{sa\sigma}}{\Delta^2_{sa\sigma} - \omega^2} \left(v_{as\sigma} + \sum_{a's'\sigma'} K_{as\sigma,a's'\sigma'}\, x_{a's'\sigma'} \right). \tag{2.81}$$

Here we introduced the matrix representation of the Kohn–Sham response function χ_{KS}:

$$\chi_{sa\sigma} = \frac{2\Delta_{sa\sigma}}{\Delta^2_{sa\sigma} - \omega^2}, \tag{2.82}$$

The overall structure of the matrix-vector equation, Eq. (2.81), involving the coefficients x, Kohn–Sham response function χ, the perturbation v, and Kohn–Sham potential response kernel K is the same as in form of integral equation of coupled Kohn–Sham Eq. (2.68), and frequency domain form of coupled Kohn–Sham, Eq. (2.74):

$$x = \chi(v + Kx) \tag{2.83}$$

The vector and matrix symbols used here were obtained by omitting the indices $as\sigma$ etc. and the corresponding summation symbols.

2.10 Reduction of the coupled perturbed Kohn–Sham equation to the Casida eigenvalue problem

For practical calculations, it is advantageous, to rewrite the CPKS equation, Eq. (2.83), by grouping the terms that depend on the expansion coefficients $x_{as\sigma}$ of the density response on the left-hand side. The structure of the resulting equation is that of an inhomogeneous linear equation:

$$(1 - \chi K)x = \chi v. \tag{2.84}$$

To leave only the true inhomogeneity, the perturbation v, on the right-hand side, we multiply this equation by χ^{-1} and obtain

$$(\chi^{-1} - K)x = v, \tag{2.85}$$

Note that all terms in this linear equation are in fact frequency-dependent.

The resonances of the system occur when some small but non-zero perturbation $v \to 0$ induces an infinitely large response x. Therefore, the nontrivial solutions of the corresponding homogeneous equation are of special interest:

$$(\chi^{-1} - K)x = 0, \tag{2.86}$$

By inserting the matrix form of the (inverse) response function, Eq. (2.82), and after the variable substitution $x = \sqrt{\Delta}y$, we obtain

$$\sqrt{\Delta}\left(\frac{\Delta^2 - \omega^2}{2\Delta} - K\right)\sqrt{\Delta}y = 0 \tag{2.87}$$

After some rearrangement, one arrives at the Casida eigenvalue problem [7]:

$$(\Delta^2 + 2\sqrt{\Delta}K\sqrt{\Delta})y = \omega^2 y \tag{2.88}$$

where K does, in principle, depend on the frequency ω. In explicit form, it reads:

$$\sum_{a's'\sigma'}\left(\delta_{ss'}\delta_{aa'}\delta_{\sigma\sigma'}\Delta^2_{sa\sigma} + 2\sqrt{\Delta_{sa\sigma}}K_{as\sigma,a's'\sigma'}\sqrt{\Delta_{s'a'\sigma'}}\right)y_{a's'\sigma'} = \omega^2 y_{as\sigma} \tag{2.89}$$

The excitation energies (resonances) ω can be calculated from the eigenvalues ω^2. The density response and the dipole oscillator strength can be obtained from the corresponding eigenvector $y_{as\sigma}$.

The eigenvalue problem for the response matrix M

$$M = \Delta^2 + 2\Delta^{1/2} K \Delta^{1/2}. \tag{2.90}$$

can be recast into finding its spectral representation:

$$M = \sum_n y_n \omega_n^2 y_n^\dagger. \tag{2.91}$$

Here the y_n is the n-th normalized eigenvector of M and ω_n^2 is the corresponding eigenvalue, Eq. (2.88).

2.11 Oscillator strengths

The linear response of the dipole moment can be written with the help of the linear response of the density, Eq. (2.77), in the following way:

$$\boldsymbol{d}^{(1)} = \int d^3\boldsymbol{r}\, \rho^{(1)}(\boldsymbol{r})\boldsymbol{r} = \sum_{as\sigma} x_{as\sigma} \int d^3\boldsymbol{r}\, \boldsymbol{r}\, \Phi_{as\sigma}(\boldsymbol{r}). \tag{2.92}$$

By definition, the dipole vector transition matrix elements are [35]:

$$\boldsymbol{d}_{as\sigma} = \int d^3\boldsymbol{r} \varphi_{a\sigma}(\boldsymbol{r})\, \boldsymbol{r}\, \varphi_{s\sigma}(\boldsymbol{r}) = \int d^3\boldsymbol{r}\, \boldsymbol{r}\, \Phi_{as\sigma}(\boldsymbol{r}). \tag{2.93}$$

Note, that $\boldsymbol{d}_{as\sigma} = (d_{x,as\sigma}, d_{y,as\sigma}, d_{z,as\sigma})$. Now, with the help of the equation for the dipole vector, Eq. (2.93), the linear response of the dipole moment is given by the sum:

$$\boldsymbol{d}^{(1)} = \sum_{as\sigma} x_{as\sigma} \boldsymbol{d}_{as\sigma}. \tag{2.94}$$

In classical electrodynamics [39] the intensity of emission is proportional to the square of the dipole moment variation:

$$I = \frac{2}{3c^3} |\ddot{\boldsymbol{d}}|^2 \tag{2.95}$$

In spectroscopy one operates instead with a related quantity, the so-called oscillator strength, which is given by [40–42]

$$f(\omega) = \frac{2}{3} \sum_{i=x,y,z} |\sum_{as\sigma} x_{as\sigma}(\omega) d_{i,as\sigma}|^2. \tag{2.96}$$

2.12 Symmetry adapted CPKS equation

In Section 2.9, we derived the matrix form of the CPKS equation, Eq. (2.88), by introducing a finite basis set of molecular orbitals. The actual expansions of the various operators were, in fact, carried out over orbital products of the type $\Phi_{as\sigma}(\boldsymbol{r}) =$

$\varphi_{a\sigma}(\boldsymbol{r})\varphi_{s\sigma}(\boldsymbol{r})$. If a system exhibits a point group symmetry, then the molecular orbitals can be classified according to the irreducible representations Γ_i of that particular point group and the partners γ_i of the irreducible representation (see Section 3.2 below). Accordingly, we will denote the occupied orbitals by $\varphi_{a\sigma}^{\Gamma_a\gamma_a}(\boldsymbol{r})$ and the unoccupied orbitals by $\varphi_{s\sigma}^{\Gamma_s\gamma_s}(\boldsymbol{r})$. The *symmetrized* orbital products will be formed as linear combination of pair products with the help of Clebsch–Gordon coefficients $C^{\tau\Gamma\gamma}_{\Gamma_a\gamma_a,\Gamma_s\gamma_s}$ [43]. The symbol τ is reserved for the rare case when there are several ways to reduce the direct product of two irreducible representations, Γ_a and Γ_s, to irreducible representation Γ. The Clebsch–Gordon coefficients are universal coefficients to form symmetry adapted product functions from symmetry adapted functions. With help of Clebsch–Gordon coefficients we can symmetrize the product of the occupied and occupied orbitals in the following way:

$$\Phi_{as\sigma}^{\tau\Gamma\gamma}(\boldsymbol{r}) = \sum_{\gamma_a\gamma_s} C^{\tau\Gamma\gamma}_{\Gamma_a\gamma_a,\Gamma_s\gamma_s}\varphi_{a\sigma}^{\Gamma_a\gamma_a}(\boldsymbol{r})\varphi_{s\sigma}^{\Gamma_s\gamma_s}(\boldsymbol{r}). \tag{2.97}$$

We will use this symmetry adapted form of the orbital products, Eq. (2.97), along the lines of Section 2.10, where the matrix form of the CPKS equation, Eq. (2.83), was derived. With Eq. (2.97), we introduce the four-component Coulomb-exchange-correlation kernel $K_{as\sigma,a's'\sigma'}$, Eq. (2.80). It allows us to split the four-component Coulomb-exchange-correlation kernel $K_{as\sigma,a's'\sigma'}$ into symmetry-irreducible blocks, see Appendix B. As the Coulomb-exchange-correlation kernel $f_{\mathrm{UXC}}(r,r')$ is defined by the full electron density of the system, which is a totally symmetric quantity, the Coulomb-exchange-correlation kernel is totally symmetric as well. Let us consider the matrix element of the potential response kernel $f_{\mathrm{UXC}}(\boldsymbol{r},\boldsymbol{r}')$ in the basis of symmetrized products of molecular orbitals $\Phi_{as\sigma}^{\tau\Gamma\gamma}$, Eq. (2.97):

$$\int d^3\boldsymbol{r}\int d^3\boldsymbol{r}'\ \Phi_{as\sigma}^{\tau\Gamma\gamma} f_{\mathrm{UXC}}\Phi_{a's'\sigma}^{\tau'\Gamma\gamma} = \frac{1}{\dim\Gamma}\sum_{\gamma}\langle\Phi_{as\sigma}^{\tau\Gamma\gamma}|f_{\mathrm{UXC}}|\Phi_{a's'\sigma}^{\tau'\Gamma\gamma}\rangle. \tag{2.98}$$

where the summation is over the partner index γ; division by the dimension $\dim\Gamma$ of the irreducible representation Γ yields an average. According to the selection rules, only those integrals are non-zero where the product functions $\Phi_{as\sigma}^{\tau\Gamma\gamma}$ and $\Phi_{a's'\sigma}^{\tau\Gamma\gamma}$ belong to the same irreducible representation Γ and the same partner γ.

Thus far we labelled the configuration space by the meta-index as which includes the index of the occupied orbital a and the index of the unoccupied orbital s; the spin index σ was treated separately. This meta-index ranges over the number of pairs N_aN_s. In the symmetry adapted formalism, we will use the meta-index $p = as(\Gamma_a\Gamma_s)\tau\Gamma$ which includes the irreducible representation Γ_a for the occupied orbitals $\varphi_{a\sigma}^{\Gamma_a\gamma_a}$, $\gamma_a = 1..\dim\Gamma_a$ and the irreducible representation Γ_s for the unoccupied orbitals $\varphi_{s\sigma}^{\Gamma_s\gamma_s}$, $\gamma_s = 1..\dim\Gamma_s$. The multiplicity index τ is reserved for the case when there are several instances of irreducible representation Γ in the direct product Γ_a and

Γ_s. With the meta-indices $p = as(\Gamma_a\Gamma_s)\tau\Gamma$ and $p' = a's'(\Gamma_{a'}\Gamma_{s'})\tau'\Gamma$ the Casida eigenvalue equation, Eq. (2.89), factorizes into several smaller eigenvalue problems for each sub-block M^Γ of M, Eq. (2.90), see Appendix B.

$$\sum_{p'\sigma'} M^\Gamma_{p\sigma,p'\sigma'} y^\Gamma_{p'\sigma'} = \omega^2 y^\Gamma_{p\sigma}. \tag{2.99}$$

Another application of the symmetry framework is symmetry adaption of the oscillator strengths, Eq. (2.96). For this purpose, we first form linear combinations of the Cartesian components of the dipole vector $\boldsymbol{d}$, Eq. (2.93), that belong to the irreducible representation Γ, partner γ and index τ:

$$\boldsymbol{d}^{\tau\Gamma\gamma}_{as\sigma} = \int d^3\boldsymbol{r}\, \Phi^{(\Gamma_a\Gamma_s)\tau\Gamma}_{as\sigma}\, \boldsymbol{r}^{\tau\Gamma\gamma}. \tag{2.100}$$

Here we introduce the symmetry-adapted components of the position vector $\boldsymbol{r}$ which are just linear combinations of Cartesian components with symmetry adaption coefficients $C_i^{\tau\Gamma\gamma}$:

$$\boldsymbol{r}^{\tau\Gamma\gamma} = \sum_{i=x,y,z} C_i^{\tau\Gamma\gamma}\, r_i. \tag{2.101}$$

The universal symmetry adaption coefficients $C_i^{\tau\Gamma\gamma}$ are the same for vector-like quantities.

The oscillator strengths f_n, Eq. (2.96), expressed in terms of symmetry adapted quantities, are given by:

$$f_n = \frac{2}{3} \sum_{\tau\Gamma\gamma} |d^{\tau\Gamma\gamma\dagger} \sqrt{\Delta_n} y^\Gamma_n|^2. \tag{2.102}$$

Chapter 3

Implementation of a time-dependent density functional formalism in the program PARAGAUSS

3.1 Casida eigenvalue problem: open-shell and closed-shell cases

Time-dependent density functional theory (TDDFT) is an exact reformulation of time-dependent quantum mechanics, where the fundamental variables are no longer the many-body wave-function but the density. The time-dependent density is determined by solving an auxiliary set of Schrödinger equations for a system of non-interacting electrons: the Kohn–Sham equations.

The symmetry constraints allow one to factorize the Casida eigenvalue problem, Section 2.12, into several independent problems distinguished by the symmetry (irrep) Γ of the solution vector y_n^Γ, Eq. (2.88), that corresponds to the n-th excited molecular term of symmetry Γ. In the following formalism we will often deal with equations, vectors, and matrices for some particular irrep, sometimes omitting the irrep label Γ. One should always keep in mind that the same type of equations involving similar structures needs to be repeated for each irrep to obtain all possible solutions.

The eigenvalue equation for an open-shell system to be solved in order to calculate excitation energies has been obtained in the previous chapter, Eq. (2.89):

$$\sum_{p'\sigma'} \left(\delta_{pp'}\delta_{\sigma\sigma'}\Delta_{p\sigma}^2 + 2\sqrt{\Delta_{p\sigma}} K_{p\sigma,p'\sigma'} \sqrt{\Delta_{p'\sigma'}} \right) y_{p'\sigma'} = \omega^2 y_{p\sigma} \tag{3.1}$$

where $\Delta_{p\sigma} = \epsilon_{a\sigma}^{\Gamma_a} - \epsilon_{s\sigma}^{\Gamma_s}$ is a difference of KS-eigenvalues $\epsilon_{a\sigma}^{\Gamma_a}$ and $\epsilon_{s\sigma}^{\Gamma_s}$. Here we use the meta-index p to label the configuration space pairs $p = (a, s)$ with molecular orbital a in the occupied part of the spectrum and molecular orbital s in the unoccupied part of

the spectrum. The response kernel $K_{p\sigma,p'\sigma'}$ is given by its matrix elements:

$$\begin{aligned} K_{p\sigma,p'\sigma'} &= (n_{s'\sigma'}^{\Gamma_{s'}} - n_{a'\sigma'}^{\Gamma_{a'}}) \\ &\times \int d^3\boldsymbol{r} \int d^3\boldsymbol{r}' \Phi_{as\sigma}^{(\Gamma_a\Gamma_s)\tau\Gamma}(\boldsymbol{r}) \left(\frac{1}{|\boldsymbol{r}-\boldsymbol{r}'|} + f_{\mathrm{XC}}^{\sigma\sigma'} \right) \Phi_{a's'\sigma'}^{(\Gamma_{a'}\Gamma_{s'})\tau\Gamma}(\boldsymbol{r}') \end{aligned} \tag{3.2}$$

Here the function $\Phi_{as\sigma}^{(\Gamma_a\Gamma_s)\tau\Gamma}$ is the symmetry adapted product of two ground-state Kohn–Sham orbitals: occupied $\varphi_{a\sigma}^{\Gamma_a\gamma_a}$ and unoccupied $\varphi_{s\sigma}^{\Gamma_s\gamma_s}$; $n_{a\sigma}^{\Gamma_a}$ and $n_{s\sigma}^{\Gamma_s}$ are the occupation numbers of the orbitals a and s with spin orientation σ. Symbols Γ_a and Γ_s denote the corresponding irreducible representations.

It is convenient to think of the configuration space index p as of a pair of energy level indices, $a\Gamma_a$ and $s\Gamma_s$. More specifically, the symbol $p = as(\Gamma_a\Gamma_s)\tau\Gamma$ is a meta-index, which includes the irreducible representation Γ_a for orbital $\varphi_{a\sigma}^{\Gamma_a\gamma_a}$ and irreducible representation Γ_s for $\varphi_{s\sigma}^{\Gamma_s\gamma_s}$. To calculate the excitation energies, we will consider the eigenvalue problem for the subblock M^{Γ} of the whole matrix M, Eq. (2.90). The two irreps Γ_a and Γ_s are assumed to be coupled into the resulting irrep Γ. The symbol τ is reserved for the rare case when there are several ways to reduce the direct product of two irreps, Γ_a and Γ_s, to irrep Γ.

For the closed-shell systems the Casida eigenvalue problem may be further factorized into two independent problems for so-called singlet-singlet and singlet-tripled transitions (see Appendix C for details). The additional symmetry that allows one to do that is the symmetry between spin-up and spin-down orbitals, $\varphi_{i\uparrow} = \varphi_{i\downarrow}$ in the case of a closed-shell system, and the corresponding relations for the integrals involving these orbitals. The eigenvalue equation for the closed-shell ground state and so-called singlet-singlet transitions reads as follows:

$$\sum_{p'} \left(\delta_{pp'}\Delta_p^2 + 4\sqrt{\Delta_p}(K_{p\uparrow,p'\uparrow} + K_{p\uparrow,p'\downarrow})\sqrt{\Delta_{p'}} \right) u_{p'} = \omega^2 u_p, \tag{3.3}$$

where the eigenvectors u_p of the reduced eigenvalue problem are related to the two "up" and "down" ranges of the true eigenvectors, $y_{p\uparrow}$ and $y_{p\downarrow}$, by:

$$\begin{cases} y_{p\uparrow} = & u_p/\sqrt{2} \\ y_{p\downarrow} = & u_p/\sqrt{2} \end{cases} \tag{3.4}$$

The reduced eigenvalue problem for the singlet-triplet excitations from the closed-shell ground state reads:

$$\sum_{p'} \left(\delta_{pp'}\Delta_p^2 + 4\sqrt{\Delta_p}(K_{p\uparrow,p'\uparrow} - K_{p\uparrow,p'\downarrow})\sqrt{\Delta_{p'}} \right) v_{p'} = \omega^2 v_p, \tag{3.5}$$

where the eigenvectors v_p of the reduced eigenvalue problem are related to the two "up" and "down" ranges of the true eigenvectors, $y_{p\uparrow}$ and $y_{p\downarrow}$, by:

$$\begin{cases} y_{p\uparrow} = & \nu_p/\sqrt{2} \\ y_{p\downarrow} = & -\nu_p/\sqrt{2} \end{cases} \tag{3.6}$$

The different signs in Eqs. (3.4) and (3.6) reflect the distinguishing feature of the two solution classes: for the singlet-singlet solutions due to Eq. (3.4), one has $\rho^{(1)}_{\uparrow} = \rho^{(1)}_{\downarrow} = \rho^{(1)}/2$. On the other hand for the singlet-triplet solution, Eq. (3.6), $\rho^{(1)}_{\uparrow} = -\rho^{(1)}_{\downarrow}$ which implies that $\rho^{(1)} = 0$.

The eigenvalue problems for excitations from the open-shell ground state, Eq. (3.1), for singlet-singlet, Eq. (3.3), and singlet-triplet, Eq. (3.5), excitations from the closed-shell ground state are of dimension $N_a N_s$, where N_a is the number of the occupied Kohn–Sham orbitals, and N_s is the number of the unoccupied Kohn–Sham orbitals. The dimension of configuration space can be reduced by taking into account only relevant ranges of occupied or/and unoccupied parts of the spectrum. Nevertheless, the dimension of such a problem can easily reach tens of thousands. Eigenvalue problems of this size can only be treated by iterative procedures seeking only some (e.g. the lowest) eigenvalues and corresponding eigenvectors. An iterative eigensolver requires repetitive multiplications of the trial vector by the matrix. This allows one to avoid explicit construction and *storage* of the whole matrix; the memory requirements to store a matrix of the typical size may be unbearable.

The only non-trivial and dense part of the matrix defining eigenvalue problem in Eqs (3.1), (3.3), and (3.5) is the representation of the potential response kernel $K_{as\sigma,a's'\sigma'}$. To further facilitate the repetitive application of the matrix-vector multiplications in the iterative solution of the eigenvalue problem, we first will factorize the four-index integrals $K_{as\sigma,a's'\sigma'}$, Eq. (3.2), with help of the resolution of the identity into the three-index integrals and two-index integrals.

3.1.1 Resolution of the identity and its application to the Coupled Perturbed Kohn–Sham equation

The evaluation of the two-electron four-index integrals over Gaussian-type basis functions is a significant component of the overall cost of many *ab initio* algorithms. One method of the approximation in the calculation of the four-index integrals is to use the resolution of the identity [44, 45] to express the four-index integrals via a smaller number of three-index quantities.

The resolution of the identity approach to the factorization of four-index integrals is based on the equality:

$$\langle as|a's'\rangle = \sum_k \langle as|k\rangle\langle k|a's'\rangle \tag{3.7}$$

which holds if the identity resolution is exact:

$$1 = \sum_k |k\rangle\langle k|. \tag{3.8}$$

In practice, both Eq. (3.7) and Eq. (3.8) hold only approximately. The ultimate goal of a strategy on the basis of the resolution of the identity is to avoid at all computing the four-index integrals, but use the associativity of matrix multiplications when applying the response kernel to trial vectors. This procedure will be explained in Section 3.1. More general, the resolution of the identity in non-orthogonal or dual bases may be expressed as

$$1 \simeq \sum_k |k\rangle\langle\bar{k}| = \sum_{kk'} |k\rangle (Q^{-1})_{kk'} \langle k'| \tag{3.9}$$

where we introduced the dual basis

$$\langle\bar{k}| = \sum_{k'} (Q^{-1})_{kk'} \langle k'| \tag{3.10}$$

defined with the inverse Q^{-1} of the overlap matrix Q:

$$Q_{kk'} = \langle k|k'\rangle \tag{3.11}$$

Non-orthogonal or dual bases factorization of the integrals leads to

$$\begin{aligned} \langle as|K|a's'\rangle &\simeq \sum_{kk'} \langle as|k\rangle\langle\bar{k}|K|\bar{k}'\rangle\langle k'|a's'\rangle \\ &= \sum_{kk'}\sum_{ll'} \langle as|k\rangle (Q^{-1})_{kk'} \langle k'|K|l\rangle (Q^{-1})_{ll'} \langle l'|a's'\rangle \end{aligned} \tag{3.12}$$

We will use a variant of the resolution of the identity (RI) with Coulomb metric to factorize the four-index integrals $K_{p\sigma,p'\sigma'}$, Eq. (3.2), in an efficient way [46,47]. The use of the Coulomb metric will be indicated by round brackets and a double bar:

$$Q_{kk'} := (k||k') = \int \frac{k(\boldsymbol{r})k'(\boldsymbol{r}')}{|\boldsymbol{r}-\boldsymbol{r}'|} d^3\boldsymbol{r} d^3\boldsymbol{r}'. \tag{3.13}$$

We will replace the four-index integrals $\langle as\sigma|K|a's'\sigma'\rangle$ by the approximate expression [45]:

$$\begin{aligned} \langle as\sigma|K|a's'\sigma'\rangle &\simeq \sum_{kk'} (as\sigma||k)\langle\bar{k}|K|\bar{k}'\rangle(k'||a's'\sigma') \\ &= \sum_{kk'}\sum_{ll'} (as\sigma||k)(Q^{-1})_{kk'}\langle k'|K|l\rangle(Q^{-1})_{ll'}(l'||a's'\sigma') \end{aligned} \tag{3.14}$$

where we used the inverse Q^{-1} of the Coulomb "overlap" matrix Q, Eq. (3.13). The functional core of the factorization of Eq. (3.14) consists of the two-index matrix elements of the response kernel K:

$$\langle k|K|k'\rangle = \langle k|\frac{1}{|\boldsymbol{r}-\boldsymbol{r}'|} + f_{\mathrm{XC}}^{\sigma\sigma'}|k'\rangle = Q_{kk'} + \langle k|f_{\mathrm{XC}}^{\sigma\sigma'}|k'\rangle. \tag{3.15}$$

The first term on the right-hand side is again the Coulomb repulsion integral $Q_{kk'}$, Eq. (3.13). The second term is the two-index exchange-correlation integral:

$$R_{k\sigma,k'\sigma'} = \langle k|f_{\mathrm{XC}}^{\sigma\sigma'}|k'\rangle. \tag{3.16}$$

Calculation of the exchange-correlation part of the partial response kernel K has been implemented in two variants: by direct grid integration and approximate resolution of identity followed by grid integration. In the first method with the direct grid integration of the XC-part of the potential response kernel K, Eq. (2.98), the latter is defined by:

$$\begin{aligned}\langle as\sigma|K|a's'\sigma'\rangle &= \sum_{klk'l'}(as\sigma||k)(Q^{-1})_{kl}Q_{ll'}(Q^{-1})_{l'k'}(k'||a's'\sigma') + \langle as\sigma|f_{\mathrm{XC}}^{\sigma\sigma'}|a's'\sigma'\rangle \\ &= \sum_{kk'}(as\sigma||k)(Q^{-1})_{kk'}(k'||a's'\sigma') + \langle as\sigma|f_{\mathrm{XC}}^{\sigma\sigma'}|a's'\sigma'\rangle. \end{aligned}\tag{3.17}$$

Here, $Q_{kk'}$ again is the Coulomb interaction, Eq. (3.13), which is used as a norm function for the resolution of the identity. The four-index exchange-correlation integrals,

$$F_{p\sigma,p'\sigma'} = \langle as\sigma|f_{\mathrm{XC}}^{\sigma\sigma'}|a's'\sigma'\rangle. \tag{3.18}$$

are, in fact, never evaluated, but instead we evaluate the product of four-index exchange-correlation integrals and a trial vector, see Section 3.3.4.

A summary of the integrals that need to be calculated and of the algorithms will be given in the next sections.

3.1.2 Approximations to the potential response kernel

For our purpose it is convenient to view the three-index Coulomb integral $(as\sigma||k)$ as a rectangular matrix $L_{p\sigma,k}$ with meta-index $p\sigma = as\sigma$ and k.

$$L_{p\sigma,k} = (p\sigma||k). \tag{3.19}$$

According to the approximation to the four-index integrals, Eq. (3.14), and with the help of the three-index Coulomb matrix, Eqs. (3.19), two-index exchange-correlation integral, (3.16), and two-index Coulomb matrix as a metric, (3.13), we can describe the eigenvalue problems for open-shell and closed-shell systems by a common expression:

$$[\Delta^2 + c\sqrt{\Delta}[LTL^\dagger + F]\sqrt{\Delta}]y = \omega^2 y. \tag{3.20}$$

The matrices L, T, and F as well as constant c have different expressions for open-shell,

closed-shell in case of singlet–singlet and singlet–triplet transitions. Table 3.1 shows the settings for each of the variants.

Table 3.1: Settings for the approximations to the potential response kernel, Eq. (3.20)

	c	L	T	F
RI-XC				
Closed-shell: S→S	4	$(as\|\|k)$	$Q^{-1}(Q+R_{\uparrow\uparrow}+R_{\uparrow\downarrow})Q^{-1}$	0
Closed-shell: S→T	4	$(as\|\|k)$	$Q^{-1}(R_{\uparrow\uparrow}-R_{\uparrow\downarrow})Q^{-1}$	0
Open shell	2	$(as\sigma\|\|k)$	$Q^{-1}(Q+R_{\sigma\sigma'})Q^{-1}$	0
Direct XC				
Closed-shell: S→S	4	$(as\|\|k)$	Q^{-1}	$F_{\uparrow\uparrow}+F_{\uparrow\downarrow}$
Closed-shell: S→T	4	$(as\|\|k)$	Q^{-1}	$F_{\uparrow\uparrow}-F_{\uparrow\downarrow}$
Open-shell	2	$(as\sigma\|\|k)$	Q^{-1}	$F_{\sigma\sigma'}$

To calculate the excitation energies of the system one has to evaluate:

- matrix L of three-index coulomb integrals, Eq. (3.19)
- matrix Q of two-index coulomb integrals, Eq. (3.13)
- matrix $R_{\sigma\sigma'}$ of two-index exchange-correlation integrals, Eq. (3.16)

In the case of direct grid integration, instead of the matrix $R_{\sigma\sigma'}$, one has to evaluate repeatedly the product of matrix $F_{\sigma\sigma'}$ of four-index exchange-correlation integrals, Eq. (3.18), with a trial vector $y_{as\sigma}$, see Section 3.3.4.

The detailed explanation of the three-, four- and two-index integrals calculation will be given in the following sections.

3.1.3 Solving the Casida eigenvalue equation in PARAGAUSS

Once the matrices L and T, Table 3.1, have been constructed from the ground state integrals, the eigenvalue problem, Eq. (3.20), can be solved for the excitation energies ω. However the dimension of this eigenvalue problem can be very large; it grows with the number N_{as} of the occupied-virtual pairs of Kohn–Sham electron levels. On the other hand, often only the lowest $N_\omega \ll N_{as}$ excitation energies are of physical interest. One possible way to address such an eigenvalue problem is to use an iterative eigensolver of Davidson [48, 49] or Lanczos [50].

E. R. Davidson developed a method that uses perturbation theory to take advantage of the sparsity and the diagonal dominance of the matrices appearing in quantum chemistry [48, 49]. For the present purpose of solving the Casida matrix eigenvalue problem, a modified and extended version of Davidson's iterative subspace algorithm

in the implementation of Stathopoulos and Fischer [51] is used. The main operation in the Davidson algorithm is the multiplication of a set of test vectors with the matrix $M = \Delta^2 + \sqrt{\Delta}K\sqrt{\Delta}$ that defines the eigenvalue problem. In the previous section we showed how to factorize the only non-trivial part of matrix M, the potential response kernel, into a product of three matrices: $K = LTL^\dagger$. This design choice allows the implementation of the matrix-based CPKS method into the program PARAGAUSS parallel algorithm without ever building the full matrix $LTL^\dagger$. In Appendix F a schematic overview over the program PARAGAUSS is given.

Only an estimate for the diagonal elements diag(M) is required to initiate the algorithm. The implementation of the Davidson algorithm due to Stathopoulos and Fischer is optimized to jointly iterate a set ("block") of eigenvectors. To simplify the notation in the following discussion only a single eigenvector y is considered.

The task of calculating the diagonal elements of matrix $LTL^\dagger$ can be parallelized over n processors, if the $N_p \times N_k$ matrix L is split row-wise, i.e. along dimension N_p, into $N_p^{(i)} \times N_k$ submatrices L_i with $N_p^{(i)} = N_p/n$, where i is the index of processors. On each processor the $N_p^{(i)} \times N_p^{(i)}$ the diagonal elements of the matrix $L_i T L_i^\dagger$ are calculated and sent to the master processor.

However, the most important and time-consuming operation of the algorithm is the repeated evaluation of the product of a trial vector $\tilde{y}$ with the matrix M, Eq. (2.90). Again the evaluation of the products $\Delta^2\tilde{y}$ or $\sqrt{\Delta}\tilde{y}$ is straightforward, and the difficulty lies in the parallel evaluation of $(LTL^\dagger)\tilde{y}$. First of all, the associativity of the matrix multiplication is employed to evaluate the product "right-to-left":

$$(LTL^\dagger)\tilde{y} = L(T(L^\dagger\tilde{y})) \tag{3.21}$$

Second, in order to exploit multiple processors, the matrix L and trial vector $\tilde{y}$ are split row-wise along dimension N_p into submatrices L_i and trial vector $\tilde{y}_i$ as described in the previous paragraph. In the first step on each processor the product $(L_i)^\dagger\tilde{y}_i$ of submatrix and test vector is evaluated according to Fig. 3.1(a). The n resulting vectors $(L_i)^\dagger\tilde{y}_i$ of length N_k are collected on the master processor, where the matrix-vector product $b = \sum_i T(L_i^\dagger\tilde{y}_i)$ is evaluated. The intermediate vector b then will be used for the matrix-vector product $L_i b$. These vectors of lengths N_p are sent to the master processor (see Fig. 3.1(b)) where they are combined to the final vector $(LTL^\dagger)\tilde{y}$.

The convergence of the iteratively determined estimate $y^{(j)}$ to the true eigenvector y is verified in the Davidson eigensolver of Stathopoulos and Fischer [51] by requiring that $||y^{(j)} - y^{(j-1)}||_\infty$ is below a certain threshold δ, where $||\delta x||_\infty = \max_{p=1,N_{as}} ||\delta x_p||$. This is the primary measure of the eigenvector convergence. The second measure is the magnitude of the residuals,

$$||Res(y^{(j)})|| \simeq ||M - \omega^2||\,||y^{(j)} - y||.$$

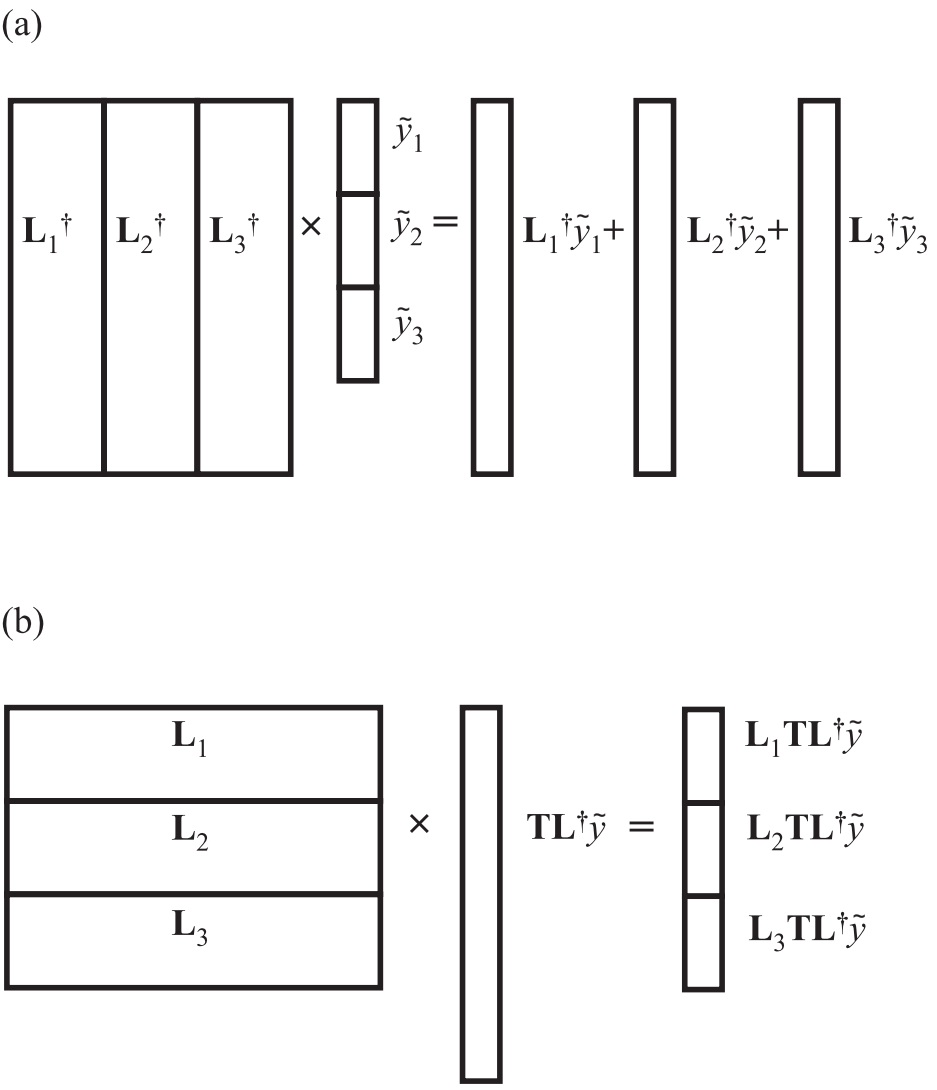

Figure 3.1: Parallel evaluation of the multiplication $(LTL^\dagger)\tilde{y}$ in PARAGAUSS

The norm of the residual is a useful convergence criterion, but it does not measure the relative error of the numerical calculation of eigenpairs. The eigenvalues of the problem are iteratively improved along with the solution vectors y until convergence.

3.2 Basis set approach to Casida equation: symmetrization of the auxiliary and orbital basis sets

In this section we will elaborate the construction of basis functions. In PARAGAUSS the basis functions are linear combinations of atomic orbitals each of which is a product of two atom-centered functions that describe the angular and the radial part, respectively. The construction of symmetrized orbital and fitting basis functions as well as contracted orbital basis set functions is described in detailed in Refs. [52] and [23]. In the present thesis, the symmetry adaptation of orbital and fitting basis functions has been extended to all irreps. Previously, for SCF the fitting basis functions have been implemented only for totally symmetric irreducible representation.

The primitive Gaussian basis functions are parametrized by an exponent α of the factor $e^{-\alpha r^2}$. Spherical harmonics are characterized by angular and magnetic quantum numbers l and m, respectively. The magnetic quantum number m is restricted by $-l \leq m \leq l$. Each atomic basis function is centered as some position $\boldsymbol{a}_{ue}$.

The locations $\boldsymbol{a}_{ue}$ of the atoms carrying the primitive basis function are characterized by two indices. The first index is the unique atom index u. The second index is an index denoting symmetry equivalent atoms e. Those atoms whose positions can be transformed into each other by symmetry operations starting from atom u are referred to as "symmetry equivalent". The third index denotes angular momentum l. The angular momentum function are referred to as $s, p, d, ...$-type functions. The fourth index is the magnetic quantum number m, which ranges from $-l$ to l. The fifth index is Gaussian exponent α; it determines the radial extension of the basis function.

The general form of a primitive basis function is

$$\chi_{uelm\alpha}(\boldsymbol{r}) = n_{l\alpha}\ [\boldsymbol{r} - \boldsymbol{a}_{ue}]_{lm}\ \exp\left(-\alpha\left|\boldsymbol{r} - \boldsymbol{a}_{ue}\right|^2\right), \tag{3.22}$$

where $[\boldsymbol{r} - \boldsymbol{a}_{ue}]_{lm}$ denotes a real spherical harmonic [23, 52]. The normalization factor $n_{l\alpha}$

$$n_{l\alpha} = \left(\frac{2\alpha}{\pi}\right)^{3/4}\left(\frac{(4\alpha)^l}{(2l-1)!!}\right)^{1/2} \tag{3.23}$$

is chosen such that $\langle\chi|\chi\rangle = 1$.

The primitive fitting basis functions $f_{uelm\alpha}(\boldsymbol{r})$ differ only by their normalization factor:

$$f_{uelm\alpha}(\boldsymbol{r}) = (2\alpha)^l\ \ [\boldsymbol{r} - \boldsymbol{a}_{ue}]_{lm}\ \exp\left(-\alpha\left|\boldsymbol{r} - \boldsymbol{a}_{ue}\right|^2\right), \tag{3.24}$$

with the real solid harmonic $[\boldsymbol{r} - \boldsymbol{a}_{ue}]_{lm}$ [52] which is used to describe the angular part. Since real solids harmonics $[\boldsymbol{r} - \boldsymbol{a}_{ue}]_{lm}$ are used in PARAGAUSS, the primitive basis functions and, thus, the final basis functions as well are real.

Contracted basis functions $g_{uelmc}(\boldsymbol{r})$ are linear combinations of primitive basis functions $\chi_{uelm\alpha}(\boldsymbol{r})$ with different exponents α and the same angular momentum quantum numbers (l and m) on the same center (u, e) with predetermined contraction coefficients d_{lc}^{α}:

$$g_{uelmc}(\boldsymbol{r}) = \sum_{\alpha} d_{lc}^{\alpha}\ \chi_{uelm\alpha}(\boldsymbol{r}) \tag{3.25}$$

The contracted basis function is characterized by unique atom u, equivalent atom e, angular momentum l, magnetic number m and contraction index c.

Symmetry adapted basis functions are linear combinations of contracted basis functions of the same unique atom u, angular momentum l and contraction index c. Orbital basis functions $g_{uelmc}(\boldsymbol{r})$ of different magnetic quantum number m located on different symmetry-equivalent atoms e are combined to form symmetry adapted basis functions

$\varphi_{ulc}^{\tau\Gamma\gamma}(\boldsymbol{r})$ characterized by an irreducible representations Γ and a partner index γ. The multiple independent instances of the same symmetry $\Gamma\gamma$ originated from the angular momentum shell of a group of symmetry equivalent atoms will be denoted by *"independent function"* index τ.

The symmetrization of basis functions has been done with help of symmetry adaption coefficients $C_{uelm}^{\tau\Gamma\gamma}$. Those coefficients are linear combinations independent of the contraction index c. They are precalculated in a separate symmetry part of the code PARAGAUSS [53]. The symmetry adapted orbital basis functions are given by

$$\varphi_{ulc}^{\tau\Gamma\gamma}(\boldsymbol{r}) = \sum_{e}\sum_{m} C_{uelm}^{\tau\Gamma\gamma}\; g_{uelmc}(\boldsymbol{r}) \tag{3.26}$$

The auxiliary symmetry adapted basis functions $k_{ul\alpha}^{\tau\Gamma\gamma}$ are constructed along the same lines as symmetry adapted orbital basis functions $\varphi_{ulc}^{\tau\Gamma c}$, but with one exception. The totally symmetric fitting function of s and r^2-type for historical reasons are normalized differently:

$$k_{u0\alpha}^{A_1} = \frac{1}{N}\sum_{i=1}^{N} f_{ui00\alpha}(\boldsymbol{r} - \boldsymbol{a}_{ui}), \tag{3.27}$$

where N is the number of symmetry equivalent atoms. For the SCF calculations in PARAGAUSS only totally symmetric fitting basis functions are in use, but for TDDFT calculations the symmetry adaption of fitting basis function has been implemented for all irreducible representations and partner indexes. The symmetrized fitting basis function are characterized by unique atom u, angular momentum l, exponent α, irreducible representation Γ, partner γ, and independent function index τ. A contraction of the fitting basis was not applied and not implemented in this study.

3.3 Integral calculation in PARAGAUSS for the Casida eigenvalue problem

3.3.1 Symmetry adaption of three-index Coulomb integrals

In this section we explain the strategy for evaluating and symmetry adapting the three-index Coulomb integrals as implemented in the parallel density functional code PARAGAUSS. Evaluation of the primitive three-index Coulomb integrals follows [53]; the symmetry adaption for use in TDDFT module has been a part of this thesis.

One of the fundamental algorithmic idea exploited by PARAGAUSS for calculating the primitive matrix elements is to start with matrix elements between s-type basis functions [23, 52] and then derive matrix elements for basis functions of higher angular momenta. Matrix elements between primitive l-type basis functions are calculated by applying differential operators of the form $[\boldsymbol{\nabla}_a]_{l\nu}$ to s-type matrix elements. Here

the square brackets with angular momentum quantum numbers denote real solid harmonic of the argument enclosed. The differential operators $[\boldsymbol{\nabla}]_{l\nu}$ are defined by formally replacing variables x, y, z by $\partial/\partial x$, $\partial/\partial y$,and $\partial/\partial z$ in the definition of $[\boldsymbol{r}]_{l\nu}$. The differential operators $[\boldsymbol{\nabla}_a]_{l\nu}$ are defined similarly by using the derivatives of the corresponding Cartesian coordinates $\partial/\partial a_x$, $\partial/\partial a_y$, and $\partial/\partial a_z$.

Let the primitive orbital basis functions χ_a and χ_b be centered at $\boldsymbol{a}$ and $\boldsymbol{b}$ and the primitive fitting basis function f centered at $\boldsymbol{c}$. Then the Coulomb integrals are given by [53]:

$$\begin{aligned}\left(\chi_{al_a\nu_a\alpha}\,\chi_{bl_b\nu_b\beta}||f_{cl_c\nu_c\gamma}\right) &= \left(\alpha^{l_a}(2l_a-1)!!\beta^{l_b}(2l_b-1)!!\right)^{-1/2} \\ &\times [\boldsymbol{\nabla}_a]_{l_a\nu_a}[\boldsymbol{\nabla}_b]_{l_b\nu_b}[\boldsymbol{\nabla}_c]_{l_c\nu_c} \\ &\times \left(\chi_{a00\alpha}\,\chi_{b00\beta}||f_{c00\gamma}\right)\end{aligned} \tag{3.28}$$

The expression for the integral between s-type basis functions to be differentiated is:

$$\left(\chi_{a00\alpha}\,\chi_{b00\beta}||f_{c00\gamma}\right) = S_{00}^{00}\frac{2\pi}{\gamma}\sqrt{\frac{\alpha+\beta}{\alpha+\beta+\gamma}}I_0\left(\frac{(\alpha+\beta)\gamma}{\alpha+\beta+\gamma}d^2\right), \tag{3.29}$$

where we introduced the distance vector

$$\boldsymbol{d} = \frac{\alpha\boldsymbol{a}+\beta\boldsymbol{b}}{\alpha+\beta} - \boldsymbol{c} \tag{3.30}$$

and used the symbol S_{00}^{00} for the overlap integral of two s-type Gaussians [52]:

$$S_{00}^{00} = \left(\frac{4\alpha\beta}{(\alpha+\beta)^2}\right)^{3/4} e^{-\frac{\alpha\beta}{\alpha+\beta}(\boldsymbol{a}-\boldsymbol{b})^2}. \tag{3.31}$$

The series of functions $I_n(\tau)$ is related to the incomplete gamma function. An important property of these functions is that differentiating each member of the series yields next higher-order member:

$$\frac{\partial^l}{\partial\tau^l}I_n(\tau) = (-1)^l I_{n+l}(\tau) \tag{3.32}$$

Finally, the general expression for the three-index integral, Eq. (3.28), with three l-type basis functions can be given in compact form:

$$\left(\chi_{al_a\nu_a\alpha}\,\chi_{bl_b\nu_b\beta}||f_{cl_c\nu_c\gamma}\right) = P\left(\frac{(\alpha+\beta)\gamma}{\alpha+\beta+\gamma}\right)^{l_c}\sum_{l=0}^{l_a+l_b} I_{l_c+l}[\frac{(\alpha+\beta)\gamma}{\alpha+\beta+\gamma}d^2]Z_{\nu_a,\nu_b,\nu_c}^{l_a,l_b,l_c,l}(\boldsymbol{a},\boldsymbol{b},\boldsymbol{c}), \tag{3.33}$$

where we introduced the normalization factor

$$P = \frac{2\pi}{\gamma}\sqrt{\frac{(\alpha+\beta)/(\alpha+\beta+\gamma)}{\pi\alpha^l(2l_a-1)!!\beta^l(2l_b-1)!!}}. \tag{3.34}$$

The auxiliary quantity $Z^{l_a,l_b,l_c,l}_{\nu_a,\nu_b,\nu_c}(\boldsymbol{a},\boldsymbol{b},\boldsymbol{c})$ carries three pairs of angular momentum indices and an additional "radial" index l. We will symmetrize the auxiliary quantity $Z^{l_a,l_b,l_c,l}_{\nu_a,\nu_b,\nu_c}(\boldsymbol{a},\boldsymbol{b},\boldsymbol{c})$ in the following way

$$Z^{l_a,l_b,l_c,l\Gamma\gamma}_{\nu_a,\nu_b}(\boldsymbol{a},\boldsymbol{b}) = \sum_e \sum_{\nu_c} C^{l\Gamma\gamma}_{\nu_c}(\boldsymbol{c}_e)\, Z^{l_a,l_b,l_c,l}_{\nu_a,\nu_b,\nu_c}(\boldsymbol{a},\boldsymbol{b},\boldsymbol{c}_e) \tag{3.35}$$

where Γ and γ denote the irreducible representation and partner of the symmetry-adapted fitting function. Here $C^{l\Gamma\gamma}_{\nu_c}(\boldsymbol{c}_e)$ are symmetrization coefficients for the contribution of the particular symmetry-equivalent atom $\boldsymbol{c}_e$ to the symmetry-adapted fitting functions, e is the index of symmetry equivalent atoms. For the SCF integrals only the totally symmetric fitting basis functions have to be considered, but for the TDDFT module we have to calculate the three-index integrals according to all irreducible representation and partners.

The symmetry adaption of the integrals with s- and r^2-type fitting basis functions is performed using renormalized symmetrization coefficients $\tilde{C}^{0A_1}_0 = \frac{1}{\sqrt{N_e}} C^{0A_1}_0$, where N_e is the number of symmetry-equivalent atoms. This ensures the historical normalization of the totally symmetric fitting functions, Eq. (3.27). After symmetry adaption, the Coulomb integrals, Eqs. (3.29) and (3.33), should be contracted over the exponents of the orbital basis. Then the symmetry adaption of the orbital basis is applied to obtain the integrals over symmetrized molecular basis functions. Each batch of integrals is then stored on disk in a separate file.

In order to understand how the integral batches can be combined into a single (three-dimensional) "matrix" L, Eq. (3.19), one needs a mapping of the batch indices on some range of integers. The indices of the unique atom types u, of the angular momentum l, of the contracted exponents c, and for the additional independent function degree of freedom τ all can be mapped by a bijective projection to a single meta-index i: i.e. $\{ulcn\} \rightarrow \{i\}$. The full identity of a basis function includes the index of the irreducible representation Γ and the partner γ, and can be represent by the three-tuple $\{i\Gamma\gamma\}$. The particular choice of the mapping is documented by the pseudo-code in Algorithm 1.

The parallelization strategy used in the three-index integral calculation is to distribute the tasks of integral evaluation to processors in batches corresponds to pairs of atomic shells $(u_1 l_1)$ and $(u_2 l_2)$. Here u_1 and u_2 are the indices of unique atoms, l_1 and l_2 are two angular momentums of those particular unique atoms.

The nontrivial step of symmetrizing of the Coulomb three-index integral can be performed with the help of the equation for the molecular orbitals, Eq. (3.26), and Clebsch–Gordon coefficients $C^{\tau\Gamma\gamma}_{\Gamma_a\gamma_a,\Gamma_s\gamma_s}$. The symmetry reduced three-index Coulomb integrals is

$$L^{\tau\Gamma}_{as\sigma,k} = \frac{1}{\dim\Gamma} \sum_{\gamma} \sum_{\gamma_a\gamma_s} C^{\tau\Gamma\gamma}_{\Gamma_a\gamma_a,\Gamma_s\gamma_s} (\varphi^{\Gamma_a\gamma_a}_{a\sigma}\, \varphi^{\Gamma_s\gamma_s}_{s\sigma} || g^{\Gamma\gamma}_k). \tag{3.36}$$

Algorithm 1 Pseudo-code defining the meta-index for fitting basis functions

!! INPUT: u as unique atom, integrals in form integral(irrep)%l(l)%m(b,a,c,n,m1,m2,pa)
!! OUTPUT: int_3c(a,b,i,m2,m1)

```
i:=0
forall Γ = 1...N_Γ do:     !! loop over irreps of fitting basis functions
 forall γ = 1... dim Γ do: !! loop over partners
  forall l do:        !! angular momentum loop
   forall c do:       !! contracted exponents loop
    forall τ do:      !! independent functions loop
     i:=i+1
     storage(...,i) = (... ...||ulτΓγ)
    done forall       !! over τ
   done forall        !! over c
  done forall         !! over l
 done forall          !! over γ
done forall           !! over Γ
```

The three-index Coulomb integral, Eq. (3.36), will be stored in files named by a pair of shell indices $(u_a l_a)$, and $(u_s l_s)$, as well as a triple of the irreducible representation indices $(\Gamma_a \Gamma_s)\tau\Gamma$, where τ is the multiplicity index.

After the SCF calculations in the response part of PARAGAUSS, the matrix L will be assembled from these batches of symmetry-reduced three-index integrals. The batches of the Coulomb integrals will be read from separate files on disk and combined into one matrix. After that the Coulomb integrals will be transformed into the basis of KS-eigenvectors with respect to the two orbital indices. The evolution of the Coulomb three-index integrals in a typical calculation is schematically displayed on Figure 3.2.

3.3.2 Symmetry adaption of the two-index Coulomb integrals

In this section we discuss the evaluation strategy and the symmetry adaption of the two-index Coulomb repulsion integrals between fitting functions. In this work the use of fitting functions in PARAGAUSS had to be extended to functions of any symmetry. This is due to the fact that the density response to a general perturbation is not necessarily totally symmetric, whereas the ground state density by definition is totally symmetric.

The primitive two-index Coulomb repulsion integral Q_{ss} of two unnormalised s-type fitting basis functions, $e^{-k(\boldsymbol{r}-\boldsymbol{a})^2}$ and $e^{-k'(\boldsymbol{r}-\boldsymbol{b})^2}$ can be written in the form

$$Q_{ss} = \left(\boldsymbol{a}k||\boldsymbol{b}k'\right) \;=\; \frac{2\pi^{5/2}}{kk'(k+k')^{1/2}} I_0(2\zeta x) \tag{3.37}$$

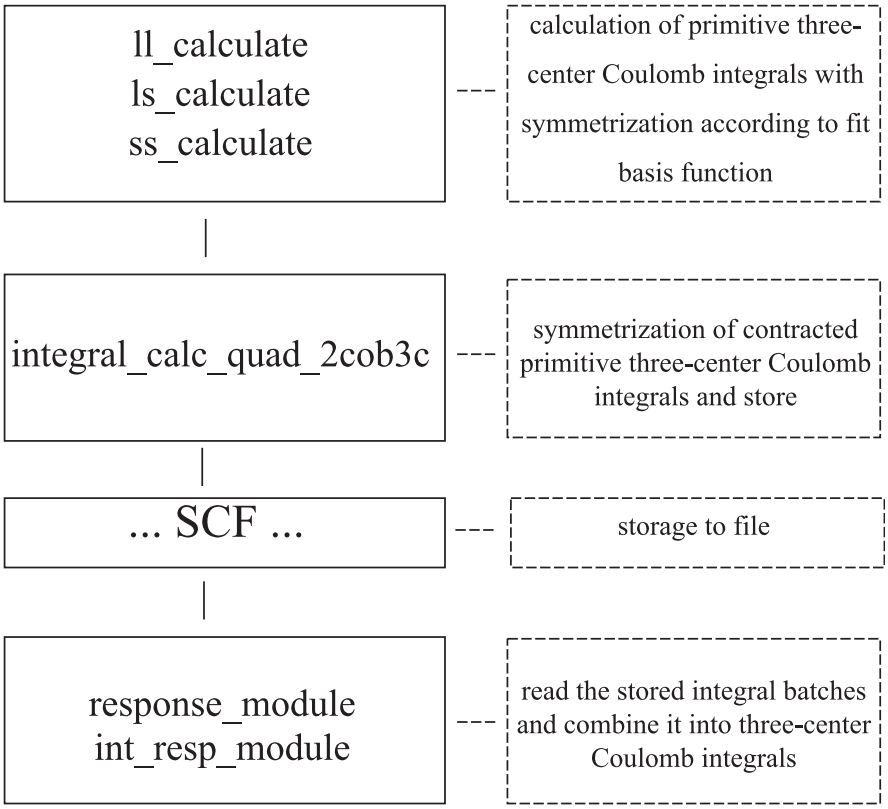

Figure 3.2: Calculation of three-index Coulomb integrals

where

$$\zeta = \frac{kk'}{k+k'}; \quad x = d^2/2; \quad \boldsymbol{d} = \boldsymbol{a} - \boldsymbol{b}. \tag{3.38}$$

In order to describe the corresponding expressions for r^2-type functions, we first note that it can be obtained by parameter differentiation:

$$r^2 e^{-kr^2} = -\frac{\partial}{\partial k} e^{-kr^2}. \tag{3.39}$$

Therefore, by applying parameter differentiation to the expression for the *ss*-Coulomb integral, Q_{ss}, Eq. (3.37), we get the Coulomb integral between an *s*- and an r^2-type fitting functions, $e^{-k(\boldsymbol{r}-\boldsymbol{a})^2}$ and, $r^2 e^{-k'(\boldsymbol{r}-\boldsymbol{b})^2}$:

$$\begin{aligned} Q_{sr} &= -\frac{\partial}{\partial k'} Q_{ss} \\ &= \frac{2\pi^{5/2}}{kk'(k+k')^{3/2}} \left[\left(\frac{3}{2} + \frac{k}{k'} \right) I_0(2\zeta x) + \frac{k}{k'} 2\zeta x I_1(2\zeta x) \right]. \end{aligned} \tag{3.40}$$

For the Coulomb integral Q_{rs} between the r^2- and the *s*-type fitting basis functions, $r^2 e^{-k(\boldsymbol{r}-\boldsymbol{a})^2}$ and $e^{-k'(\boldsymbol{r}-\boldsymbol{b})^2}$ one has to just interchange k and k' in Eq. (3.40). And the Coulomb integral Q_{rr} between the two r^2-type fitting basis functions is obtained by

double parameter differentiation of the Coulomb ss-integral Q_{ss}:

$$\begin{aligned} Q_{rr} &= \frac{\partial^2}{\partial k \partial k'} Q_{ss} \\ &= \frac{2\pi^{5/2}}{kk'(k+k')^{5/2}} \\ &\times \left[\frac{3}{2}\left(\frac{k}{k'}+\frac{k'}{k}+\frac{5}{2}\right) I_0 + \frac{3}{2}\left(\frac{k}{k'}+\frac{k'}{k}\right) 2\zeta x I_1 + (2\zeta x)^2 I_2\right] \end{aligned} \tag{3.41}$$

Having expressed those equations for the different two-index Coulomb integrals Q_{ss}, Q_{sr}, and Q_{rr} as pure functions of $x = d^2/2$, it is easy to apply the parameter differentiation with respect to the two atomic centers $\boldsymbol{a}$ and $\boldsymbol{b}$ in order to obtain the (unnormalised) integrals between general l-type fitting function

$$\begin{aligned} (\boldsymbol{a} l_a m_a k || \boldsymbol{b} l_b m_b k') &= (-1)^{l_a+l_b} [\boldsymbol{\nabla}_a]_{l m_a} [\boldsymbol{\nabla}_b]_{l m_b} Q_{ss}(d^2/2) \\ &= (-1)^{l_a} [\boldsymbol{\nabla}]_{l m_a} [\boldsymbol{\nabla}]_{l m_b} Q_{ss}(d^2/2) \\ &= (-1)^{l_a} \sum_{l=\max(l_a l_b)}^{l_a+l_b} Q_{ss}^{(l)}(d^2/2) Z_{m_a m_b}^{l_a\, l_b\, l}(\boldsymbol{d}) \end{aligned} \tag{3.42}$$

Here we first replaced $\boldsymbol{\nabla}_a$ and $\boldsymbol{\nabla}_b$ by $\boldsymbol{\nabla} = \partial/\partial \boldsymbol{d}$ with the appropriate sign. To obtain the two-index Coulomb integral for general l-type fitting function Q_{ll}, we will use ss-Coulomb integral Q_{ss} and the l-derivatives of Q_{ss} e.g. $Q_{ss}^{(l)}$. The auxiliary quantity $Z_{m_a m_b}^{l_a\, l_b\, l}(\boldsymbol{d})$ carries two pairs of angular momentum indices and an additional "radial" index l. Since Q_{ss} contains the incomplete gamma function I_n, the derivatives $Q_{ss}^{(l)}$ will be obtained from the equation (see Eq. (3.32)):

$$\frac{\partial^l}{\partial x^l} I_n(2\zeta x) = (-1)^l (2\zeta)^l I_{n+l}(2\zeta x) \tag{3.43}$$

The primitive two-center Coulomb integrals $(\boldsymbol{a}_i l_a m_a k || \boldsymbol{b}_j l_b m_b k')$ for all pairs (i, j) of the symmetry equivalent atoms should be symmetrized, packed and stored. The transition to the Coulomb integrals over the symmetrized fitting functions is done by invoking summation with symmetry adaption coefficients:

$$\begin{aligned} (g_{\boldsymbol{a} l_a k}^{\tau\Gamma} || g_{\boldsymbol{b} l_b k'}^{\tau'\Gamma}) &= \frac{1}{\dim \Gamma} \sum_{\gamma} \\ &\times \sum_{i m_a} \sum_{j m_b} C_{i\, l_a m_a}^{\tau\Gamma\gamma} C_{j\, l_b m_b}^{\tau'\Gamma\gamma} (\boldsymbol{a}_i l_a m_a k || \boldsymbol{b}_j l_b m_b k') \end{aligned} \tag{3.44}$$

Here, $\dim \Gamma$ is the number of partners of an irreducible representation Γ. Note that the summation is performed over all pairs of the symmetry-equivalent atoms i and j. This is different from the special totally symmetric case of the ground state calculation in SCF part, where we would replace the summation over all pairs of symme-

try equivalent atoms by a sum over so-called symmetry nonequivalent distance vectors [23, 52–54]. The resulting batch of two-index Coulomb integrals is stored in a file named after the shell indices $(u_a l_a)$ and $(u_b l_b)$ and irreducible representation Γ.

The expression for the symmetry reduced integrals corresponding to a given symmetry irreducible representation Γ is written as the average over symmetry partners. It is stored in upper triangular form.

3.3.3 Evaluation of the two-index exchange-correlation integrals

The exchange-correlation integrals are evaluated by numeric quadrature on a space grid. The integrals required for TDDFT are calculated after the SCF convergence is reached on the same numerical grid as the XC contributions during SCF iterations. The grid quadrature, essentially a summation over grid points, is parallelized over the grid points. The expression for the symmetry reduced integrals corresponding to a given symmetry representation can be written as the average over symmetry partners:

$$R^{\Gamma}_{k\sigma\, k'\sigma'} = \frac{1}{\dim \Gamma} \sum_{\gamma} \langle k\Gamma\gamma | f^{\sigma\sigma'}_{\mathrm{XC}} | k'\Gamma\gamma \rangle. \tag{3.45}$$

The exchange-correlation kernel $f^{\sigma\sigma'}_{\mathrm{XC}}$ reflects the first-order change in the time-dependent XC-part of the KS-potential due to the density shift $\delta\rho$:

$$f^{\sigma\sigma'}_{\mathrm{XC}}(\boldsymbol{r}, \boldsymbol{r}') = \frac{\delta v^{\sigma}_{\mathrm{XC}}(\boldsymbol{r})}{\delta \rho^{\sigma'}(\boldsymbol{r}')}. \tag{3.46}$$

In order to obtain a practical computational scheme, we will use the so-called adiabatic local density approximation (ALDA). The adiabatic approximation for LDA can be explained as a limiting case of a slowly varying density and potential, both in time as well as in space dimensions. These conditions are rarely fulfilled in real systems of interest; therefore this is a dramatic approximation to TDDFT [10]. However, from the very beginning of TDDFT until today only a few attempts have been made to improve adiabatic approximation for the potential response kernel $f^{\sigma\sigma'}_{\mathrm{XC}}$ [10]. On the other hand, the adiabatic approximation for LDA can be extended to the GGA case. According to this approximation the response kernel is reduced to a spatially local, real function, evaluated at the ground state density $\rho_0(\boldsymbol{r})$:

$$f^{\sigma\sigma'}_{\mathrm{XC}}(\boldsymbol{r}, \boldsymbol{r}') = \delta(\boldsymbol{r} - \boldsymbol{r}') \left. \frac{\delta v^{\sigma}_{\mathrm{XC}}(\rho(\boldsymbol{r}))}{\delta \rho^{\sigma'}(\boldsymbol{r})} \right|_{\rho=\rho_0} \tag{3.47}$$

The LDA exchange-correlation functionals for use within the TDDFT framework has been made available in the program package PARAGAUSS in a previous work [11]. A part of the current work was to extend the adiabatic approximation to the generalized gradient approximation.

The essence of the "generalization" in GGA in comparison to LDA is that the GGA exchange-correlation functional depends not only on density ρ (as LDA), but also on the density gradient $\boldsymbol{\nabla}\rho$. The energy functional expression for the second-order functional derivative of the GGA exchange-correlation functional is obtained from XC energy density ϵ_{XC}, Eq. (3.50), by differentiation with respect to the density ρ and the density gradient $\boldsymbol{\nabla}\rho$ [55]:

$$f_{\mathrm{XC}} = \left(\frac{\partial^2}{\partial\rho^2} - \boldsymbol{\nabla}\frac{\partial^2}{\partial\rho\partial\boldsymbol{\nabla}\rho} + \nabla_i\nabla_j\frac{\partial^2}{\partial\nabla_i\rho\partial\nabla_j\rho} \right)\epsilon_{\mathrm{XC}}, \tag{3.48}$$

The general form of the exchange-correlation energy can be written as

$$E_{\mathrm{XC}}[\rho] = \int d^3\boldsymbol{r}\, \epsilon_{\mathrm{XC}}(\rho_\uparrow, \rho_\downarrow, \boldsymbol{\nabla}\rho_\uparrow, \boldsymbol{\nabla}\rho_\downarrow). \tag{3.49}$$

Here ϵ_{XC} is the exchange-correlation energy density per volume, which in PARAGAUSS depends on electron densities of different spins $\rho_\uparrow$, and $\rho_\downarrow$, and the squares of the gradients of electron densities $\gamma_{\uparrow\uparrow} = |\boldsymbol{\nabla}\rho_\uparrow|^2$, $\gamma_{\downarrow\downarrow} = |\boldsymbol{\nabla}\rho_\downarrow|^2$, and $\gamma_{\uparrow\downarrow} = (\boldsymbol{\nabla}\rho_\uparrow\boldsymbol{\nabla}\rho_\downarrow) = (\boldsymbol{\nabla}\rho_\downarrow\boldsymbol{\nabla}\rho_\uparrow)$.

$$\epsilon_{\mathrm{XC}} = \epsilon_{\mathrm{XC}}(\rho_\uparrow, \rho_\downarrow, \gamma_{\uparrow\uparrow}, \gamma_{\downarrow\downarrow}, \gamma_{\uparrow\downarrow}). \tag{3.50}$$

In Appendix D the relation between the first- and second-order derivatives with respect to $\boldsymbol{\nabla}\rho$ and γ is derived. After the mathematical transformation of the integral $R^{\Gamma}_{k\sigma\,k'\sigma'}$, Eq. (3.45), with a XC-kernel of the form of adiabatic approximation for LDA or GGA, Eq. (3.47), we obtain the final equation for $R_{k\sigma\,k'\sigma'}$:

$$\begin{aligned}
R_{k\sigma\,k'\sigma'} &= \int kk' \left(\frac{\partial^2}{\partial\rho_\sigma\partial\rho_{\sigma'}} \right)\epsilon_{\mathrm{XC}}\, d^3\boldsymbol{r} \\
&+ \int (\boldsymbol{\nabla}k\boldsymbol{\nabla}k') \left(\frac{\partial}{\partial\gamma_{\sigma'\sigma}} + \frac{\partial}{\partial\gamma_{\sigma\sigma'}} \right)\epsilon_{\mathrm{XC}}\, d^3\boldsymbol{r} \\
&+ \sum_{\tau}\int \left(\boldsymbol{\nabla}\left(kk'\right)\boldsymbol{\nabla}\rho_\tau\right) \left(\frac{\partial^2}{\partial\rho_\sigma\partial\gamma_{\sigma'\tau}} + \frac{\partial^2}{\partial\rho_\sigma\partial\gamma_{\tau\sigma'}} \right)\epsilon_{\mathrm{XC}}\, d^3\boldsymbol{r} \\
&+ \sum_{\tau\tau'}\int (\boldsymbol{\nabla}k\boldsymbol{\nabla}\rho_\tau)\left(\boldsymbol{\nabla}k'\boldsymbol{\nabla}\rho_{\tau'}\right) \\
&\times \left(\frac{\partial^2}{\partial\gamma_{\sigma\tau}\partial\gamma_{\sigma'\tau'}} + \frac{\partial^2}{\partial\gamma_{\tau\sigma}\partial\gamma_{\sigma'\tau'}} + \frac{\partial^2}{\partial\gamma_{\sigma\tau}\partial\gamma_{\tau'\sigma'}} + \frac{\partial^2}{\partial\gamma_{\tau\sigma}\partial\gamma_{\tau'\sigma'}} \right)\epsilon_{\mathrm{XC}}\, d^3\boldsymbol{r}.
\end{aligned} \tag{3.51}$$

The summation over spin indices τ and τ' can be explicitly carried out for each particular choice of the integral indices σ and σ'. In the most general case of an open-shell system, Eq. (3.45), for the spin state variables $\sigma = \uparrow$ and $\sigma' = \uparrow$ one obtains the following

expression:

$$\begin{aligned} R_{k\uparrow k'\uparrow} &= \int k \left(\frac{\partial^2 \epsilon_{\mathrm{XC}}}{\partial \rho_\uparrow^2}\right) k' \, d^3\boldsymbol{r} \\ &+ 2\int \boldsymbol{\nabla} k \left(\frac{\partial \epsilon_{\mathrm{XC}}}{\partial \gamma_{\uparrow\uparrow}}\right) \boldsymbol{\nabla} k' \, d^3\boldsymbol{r} \\ &+ \int \boldsymbol{\nabla}\left(kk'\right) \left(2\boldsymbol{\nabla}\rho_\uparrow \frac{\partial^2 \epsilon_{\mathrm{XC}}}{\partial \rho_\uparrow \partial \gamma_{\uparrow\uparrow}} + \boldsymbol{\nabla}\rho_\downarrow \frac{\partial^2 \epsilon_{\mathrm{XC}}}{\partial \rho_\uparrow \partial \gamma_{\uparrow\downarrow}}\right) d^3\boldsymbol{r} \\ &+ 4\int \left(\boldsymbol{\nabla} k \boldsymbol{\nabla}\rho_\uparrow\right) \left(\frac{\partial^2 \epsilon_{\mathrm{XC}}}{\partial \gamma_{\uparrow\uparrow}^2}\right) \left(\boldsymbol{\nabla}\rho_\uparrow \boldsymbol{\nabla} k'\right) \, d^3\boldsymbol{r} \\ &+ 2\int \left(\boldsymbol{\nabla} k \boldsymbol{\nabla}\rho_\uparrow\right) \left(\frac{\partial^2 \epsilon_{\mathrm{XC}}}{\partial \gamma_{\uparrow\uparrow} \partial \gamma_{\uparrow\downarrow}}\right) \left(\boldsymbol{\nabla}\rho_\downarrow \boldsymbol{\nabla} k'\right) \, d^3\boldsymbol{r} \\ &+ 2\int \left(\boldsymbol{\nabla} k \boldsymbol{\nabla}\rho_\downarrow\right) \left(\frac{\partial^2 \epsilon_{\mathrm{XC}}}{\partial \gamma_{\uparrow\uparrow} \partial \gamma_{\uparrow\downarrow}}\right) \left(\boldsymbol{\nabla}\rho_\uparrow \boldsymbol{\nabla} k'\right) \, d^3\boldsymbol{r} \\ &+ \int \left(\boldsymbol{\nabla} k \boldsymbol{\nabla}\rho_\downarrow\right) \left(\frac{\partial^2 \epsilon_{\mathrm{XC}}}{\partial \gamma_{\uparrow\downarrow}^2}\right) \left(\boldsymbol{\nabla}\rho_\downarrow \boldsymbol{\nabla} k'\right) \, d^3\boldsymbol{r}, \end{aligned} \tag{3.52}$$

In another essential case of open-shell systems with spin state variables $\sigma = \uparrow$ and $\sigma' = \downarrow$ the expression for the two-index exchange correlation integral becomes

$$\begin{aligned} R_{k\uparrow k'\downarrow} &= \int k \left(\frac{\partial^2 \epsilon_{\mathrm{XC}}}{\partial \rho_\uparrow \partial \rho_\downarrow}\right) k' \, d^3\boldsymbol{r} \\ &+ \int \boldsymbol{\nabla} k \left(\frac{\partial \epsilon_{\mathrm{XC}}}{\partial \gamma_{\uparrow\downarrow}}\right) \boldsymbol{\nabla} k' \, d^3\boldsymbol{r} \\ &+ \int \boldsymbol{\nabla}\left(kk'\right) \left(2\boldsymbol{\nabla}\rho_\downarrow \frac{\partial^2 \epsilon_{\mathrm{XC}}}{\partial \rho_\uparrow \partial \gamma_{\downarrow\downarrow}} + \boldsymbol{\nabla}\rho_\uparrow \frac{\partial^2 \epsilon_{\mathrm{XC}}}{\partial \rho_\uparrow \partial \gamma_{\uparrow\downarrow}}\right) d^3\boldsymbol{r} \\ &+ 4\int \left(\boldsymbol{\nabla} k \boldsymbol{\nabla}\rho_\uparrow\right) \left(\frac{\partial^2 \epsilon_{\mathrm{XC}}}{\partial \gamma_{\uparrow\uparrow} \partial \gamma_{\downarrow\downarrow}}\right) \left(\boldsymbol{\nabla}\rho_\downarrow \boldsymbol{\nabla} k'\right) \, d^3\boldsymbol{r} \\ &+ 2\int \left(\boldsymbol{\nabla} k \boldsymbol{\nabla}\rho_\uparrow\right) \left(\frac{\partial^2 \epsilon_{\mathrm{XC}}}{\partial \gamma_{\uparrow\uparrow} \partial \gamma_{\uparrow\downarrow}}\right) \left(\boldsymbol{\nabla}\rho_\uparrow \boldsymbol{\nabla} k'\right) \, d^3\boldsymbol{r} \\ &+ 2\int \left(\boldsymbol{\nabla} k \boldsymbol{\nabla}\rho_\downarrow\right) \left(\frac{\partial^2 \epsilon_{\mathrm{XC}}}{\partial \gamma_{\downarrow\downarrow} \partial \gamma_{\uparrow\downarrow}}\right) \left(\boldsymbol{\nabla}\rho_\downarrow \boldsymbol{\nabla} k'\right) \, d^3\boldsymbol{r} \\ &+ \int \left(\boldsymbol{\nabla} k \boldsymbol{\nabla}\rho_\uparrow\right) \left(\frac{\partial^2 \epsilon_{\mathrm{XC}}}{\partial \gamma_{\uparrow\downarrow}^2}\right) \left(\boldsymbol{\nabla}\rho_\downarrow \boldsymbol{\nabla} k'\right) \, d^3\boldsymbol{r}. \end{aligned} \tag{3.53}$$

In the special case of a closed-shell system we can exploit the consequences of the equalities

$$\rho_\uparrow = \rho_\downarrow = \frac{\rho}{2};\ \boldsymbol{\nabla}\rho_\uparrow = \boldsymbol{\nabla}\rho_\downarrow = \frac{\boldsymbol{\nabla}\rho}{2};\ \gamma_{\uparrow\uparrow} = \gamma_{\downarrow\downarrow} = \gamma_{\uparrow\downarrow} = \frac{|\boldsymbol{\nabla}\rho|^2}{4} \tag{3.54}$$

and simplify the Eqs. (3.52) and (3.53), by grouping equivalent contributions. The two-

index exchange-correlation integrals $R_{k\uparrow k'\uparrow}$ in the closed shell case simplifies to:

$$\begin{aligned} R_{k\uparrow k'\uparrow} &= \int k \left(\frac{\partial^2 \epsilon_{\mathrm{XC}}}{\partial \rho_\uparrow^2} \right) k' \, d^3\boldsymbol{r} \\ &+ 2 \int \boldsymbol{\nabla} k \left(\frac{\partial \epsilon_{\mathrm{XC}}}{\partial \gamma_{\uparrow\uparrow}} \right) \boldsymbol{\nabla} k' \, d^3\boldsymbol{r} \\ &+ \int \boldsymbol{\nabla} \left(kk' \right) \boldsymbol{\nabla} \rho \left(\frac{\partial^2 \epsilon_{\mathrm{XC}}}{\partial \rho_\uparrow \partial \gamma_{\uparrow\uparrow}} + \frac{1}{2} \frac{\partial^2 \epsilon_{\mathrm{XC}}}{\partial \rho_\uparrow \partial \gamma_{\uparrow\downarrow}} \right) d^3\boldsymbol{r} \\ &+ \int \left(\boldsymbol{\nabla} k \boldsymbol{\nabla} \rho \right) \left(\frac{\partial^2 \epsilon_{\mathrm{XC}}}{\partial \gamma_{\uparrow\uparrow}^2} + \frac{\partial^2 \epsilon_{\mathrm{XC}}}{\partial \gamma_{\uparrow\uparrow} \partial \gamma_{\uparrow\downarrow}} + \frac{1}{4} \frac{\partial^2 \epsilon_{\mathrm{XC}}}{\partial \gamma_{\uparrow\downarrow}^2} \right) \left(\boldsymbol{\nabla} \rho \boldsymbol{\nabla} k' \right) \, d^3\boldsymbol{r} \end{aligned} \tag{3.55}$$

The two-index exchange-correlation integrals $R_{k\uparrow k'\downarrow}$ in the closed shell case is similarly simplified to:

$$\begin{aligned} R_{k\uparrow k'\downarrow} &= \int k \left(\frac{\partial^2 \epsilon_{\mathrm{XC}}}{\partial \rho_\uparrow \partial \rho_\downarrow} \right) k' \, d^3\boldsymbol{r} \\ &+ \int \boldsymbol{\nabla} k \left(\frac{\partial \epsilon_{\mathrm{XC}}}{\partial \gamma_{\uparrow\downarrow}} \right) \boldsymbol{\nabla} k' \, d^3\boldsymbol{r} \\ &+ \int \boldsymbol{\nabla} \left(kk' \right) \boldsymbol{\nabla} \rho \left(\frac{\partial^2 \epsilon_{\mathrm{XC}}}{\partial \rho_\uparrow \partial \gamma_{\downarrow\downarrow}} + \frac{1}{2} \frac{\partial^2 \epsilon_{\mathrm{XC}}}{\partial \rho_\uparrow \partial \gamma_{\uparrow\downarrow}} \right) d^3\boldsymbol{r} \\ &+ \int \left(\boldsymbol{\nabla} k \boldsymbol{\nabla} \rho \right) \left(\frac{\partial^2 \epsilon_{\mathrm{XC}}}{\partial \gamma_{\uparrow\uparrow} \partial \gamma_{\downarrow\downarrow}} + \frac{\partial^2 \epsilon_{\mathrm{XC}}}{\partial \gamma_{\uparrow\uparrow} \partial \gamma_{\uparrow\downarrow}} + \frac{1}{4} \frac{\partial^2 \epsilon_{\mathrm{XC}}}{\partial \gamma_{\uparrow\downarrow}^2} \right) \left(\boldsymbol{\nabla} \rho \boldsymbol{\nabla} k' \right) \, d^3\boldsymbol{r} \end{aligned} \tag{3.56}$$

In practice, there are more terms to integrate as in the implementation we expand the gradient of the product $\boldsymbol{\nabla}(kk')$ in the third line of Eqs. (3.52), (3.53), (3.55), and (3.56) by using the formula:

$$\boldsymbol{\nabla} \left(kk' \right) = \left(\boldsymbol{\nabla} k \right) k' + k \left(\boldsymbol{\nabla} k' \right) . \tag{3.57}$$

In practice the integrals are of course evaluated approximately by a numerical quadrature on the grid of points.

3.3.4 Representing exact exchange-correlation response kernel in the basis of orbital products.

The purpose of the resolution of identity introduced in Section 3.1.1 is an attempt to replace the (four-index) matrix representation of the potential response kernel in the basis of orbital *products* by an *approximate* but more economic (two-index) matrix representation in the basis of fitting functions. The construction of the latter was discussed in the preceding section (Section 3.3.3). However, this approximation performs differently when applied to the Coulomb or XC-part of the potential response kernel.

The two-electron response kernel $K = K_{\mathrm{H}} + K_{\mathrm{XC}}$ can be thought of as a Taylor

coefficient of the second-order term in the DFT energy expansion series over density response $\delta\rho$. As such it should be positively definite at the minimum of the energy functional (defined on the sub-domain of N-representable densities [7,9]). Technically it is separated in the positive definite Coulomb part and the "negative" XC-part that, in particular, compensates for self-interaction [7,9]. Moreover, in the adiabatic LDA approximation, the dominating exchange kernel has a weak singularity at low densities far from the nuclei $K_X = -C\rho^{-2/3}$. Although the RI method, also called "density fitting technique", appears to work well for the Coulomb part, it also appears to be hard to preserve the positiveness of the total response kernel by representing XC-kernel in an arbitrary chosen auxiliary basis sets. In the resolution of the identity approach, the auxiliary basis for the XC-kernel is dual to that for density response $\delta\rho$, see Appendix E. In the case of the highly non-local Coulomb metric the dual basis of extended systems becomes extremely delocalized when starting from localized atomic density fitting functions; this may entail numerical instabilities. The direct approach of representing the XC-response kernel in the basis of orbital products, on the other hand, appears to cancel nicely the weak singularity of the LDA exchange and does not lead to numerical instabilities.

Combining Coulomb matrix Q, Eq. (3.17), and matrix $F_{p\sigma,p'\sigma'}$ of direct grid integration for XC potential response kernel, Eq. (3.18), and using the meta-index $p = (as)$ for orbital pairs, we obtain the response matrix $M_{p\sigma,p'\sigma'}$, Eq. (2.90), in the following form:

$$M_{p\sigma,p'\sigma'} = \delta_{pp'}\delta_{\sigma\sigma'}\Delta^2_{p\sigma} + 2\sqrt{\Delta}[Q_{p\sigma,p'\sigma'} + F_{p\sigma,p'\sigma'}]\sqrt{\Delta} \tag{3.58}$$

The Coulomb part $Q_{p\sigma,p'\sigma'}$ is calculated with the resolution of the identity, as shown before in Section 3.1.1.

The matrix element of the exchange-correlation response kernel between two basis functions of the product space $\Phi_{p\sigma}$ ans $\Phi_{p'\sigma'}$ is, formally, given by the integral:

$$F_{p\sigma,p'\sigma'} = \langle \Phi_{p\sigma} | f_{\mathrm{XC}}^{\sigma\sigma'} | \Phi_{p'\sigma'} \rangle. \tag{3.59}$$

In the simplest case, without symmetry, $\Phi_{p\sigma}$ is the product of two molecular orbitals $\varphi_{a\sigma}(\boldsymbol{r})\varphi_{s\sigma}(\boldsymbol{r})$, Eq. (2.76). A basis of the product space in the symmetry-adapted case can be given by

$$\Phi^{\tau\Gamma\gamma}_{p\sigma}(\boldsymbol{r}) = \sum_{\gamma_a\gamma_s} C^{\tau\Gamma\gamma}_{\Gamma_a\gamma_a,\Gamma_s\gamma_s} \varphi^{\Gamma_a\gamma_a}_{a\sigma}(\boldsymbol{r})\varphi^{\Gamma_s\gamma_s}_{s\sigma}(\boldsymbol{r}). \tag{3.60}$$

where $C^{\tau\Gamma\gamma}_{\Gamma_a\gamma_a,\Gamma_s\gamma_s}$ are the Clebsch–Gordon coefficients.

Comparing the expressions for $F_{p\sigma,p'\sigma'}$, Eq. (3.59), and for $R_{k\sigma,k'\sigma'}$, Eq. (3.45), it follows that the derivations in Section 3.3.3 for R-integrals formally also hold for F-integrals. In particular, the expression on the right-hand side of Eq. (3.51) can be used for $F_{p\sigma,p'\sigma'}$ if one substitutes:

$$k : = \Phi_{p\sigma} = \varphi_{a\sigma}\varphi_{s\sigma}, \tag{3.61}$$

$$\boldsymbol{\nabla} k : = \boldsymbol{\nabla}\Phi_{p\sigma} = \boldsymbol{\nabla}\left(\varphi_{a\sigma}\varphi_{s\sigma}\right) = \left(\boldsymbol{\nabla}\varphi_{a\sigma}\right)\varphi_{s\sigma} + \varphi_{a\sigma}\left(\boldsymbol{\nabla}\varphi_{s\sigma}\right). \tag{3.62}$$

However, it is not necessary to evaluate directly the exchange-correlation integrals $F_{p\sigma,p'\sigma'}$. The requirements to do so in terms of time and memory would be very high in a realistic calculation. Rather, one needs the value of the (matrix) product of the exact exchange-correlation integral $F_{p\sigma,p'\sigma'}$ and a trial eigenvector $\{x_{p\sigma}\}$ provided by the eigensolver in each iteration:

$$Y_{p\sigma} = \sum_{p'\sigma'} F_{p\sigma,p'\sigma'} x_{p'\sigma'}. \tag{3.63}$$

After substituting the equation for the exchange-correlation integrals $F_{p\sigma,p'\sigma'}$, Eqs. (3.59) and (3.60), we obtain

$$Y_{as\sigma} = \varphi_{a\sigma}(\boldsymbol{r})\varphi_{s\sigma}(\boldsymbol{r}) \times \sum_{\sigma'} f_{\mathrm{XC}}^{\sigma\sigma'} \times \sum_{a's'} \varphi_{a'\sigma'}(\boldsymbol{r})\varphi_{s'\sigma'}(\boldsymbol{r})\, x_{a's'\sigma'}(\boldsymbol{r}). \tag{3.64}$$

Schematically, the evaluation of Eq. (3.64), will be done in three steps. In the first step one calculates the response of the density:

$$\delta\rho_{\sigma'}(\boldsymbol{r}) = \sum_{a's'} \varphi_{a'\sigma'}(\boldsymbol{r})\varphi_{s'\sigma'}(\boldsymbol{r}) x_{a's'\sigma'}(\boldsymbol{r}). \tag{3.65}$$

In the second step one obtains the potential response:

$$\delta v_{\sigma}(\boldsymbol{r}) = \sum_{\sigma'} f_{\mathrm{XC}}^{\sigma\sigma'}(\boldsymbol{r})\, \delta\rho_{\sigma'}(\boldsymbol{r}). \tag{3.66}$$

The third step is the calculation of $Y_{p\sigma}$:

$$Y_{p\sigma} = \langle \varphi_{a\sigma} | \delta v_{\sigma} | \varphi_{s'\sigma'} \rangle, \tag{3.67}$$

again, the meta-index $p = (as)$ was introduced in the last equation.

3.3.5 Numerical quadrature for the LDA exchange-correlation integrals

In the actual implementation the calculation of the LDA integrals is done in five steps.

One calculates the values of the molecular KS-orbitals $\varphi_{i\sigma}^{\Gamma\gamma}(\boldsymbol{r})$ on the grid of points $\boldsymbol{r}$ using eigenvectors $E_{in\sigma}^{\Gamma}$ and values of the orbital basis functions $\chi_n^{\Gamma\gamma}(\boldsymbol{r})$ on the grid:

$$\varphi_{i\sigma}^{\Gamma\gamma}(\boldsymbol{r}) = \sum_{n} E_{in\sigma}^{\Gamma} \chi_n^{\Gamma\gamma}(\boldsymbol{r}) \tag{3.68}$$

Further down we will distinguish occupied molecular orbitals $\varphi_{a\sigma}^{\Gamma_\gamma}(\boldsymbol{r})$ and unoccupied molecular orbitals $\varphi_{s\sigma}^{\Gamma_\gamma}(\boldsymbol{r})$. This operation has been implemented using BLAS matrix multiplication subroutines [56]. The cost of the operation per irrep and per partner is of the order $N_r N_\chi$, where N_r is the number of grid points and N_χ is the dimension of orbital basis set.

In the next step one computes the two-center functions $\Phi_{p\sigma}^{\tau\Gamma\gamma}(\boldsymbol{r})$ from the products of occupied and virtual orbitals by symmetry adaption with the help of Clebsch–Gordon coefficients $C^{\tau\Gamma\gamma}_{\Gamma_a\gamma_a,\Gamma_s\gamma_s}$, Eq. (3.60). The cost of the operation per irrep and per partner is of the order $N_r N_p$, where N_r is the number of grid points and N_p is the dimension of product space of occupied and virtual molecular orbital basis sets.

The symmetry-adapted basis functions together with the set of approximate eigenvectors $\{x_{p\sigma}^n\}$ are used to calculate the response of the density.

$$\delta\rho_\sigma^{n\tau\Gamma\gamma}(\boldsymbol{r}) = \sum_p \Phi_{p\sigma}^{\tau\Gamma\gamma}(\boldsymbol{r}) x_{p\sigma}^n \tag{3.69}$$

The set of approximate eigenvectors $\{x_{p\sigma}^n\}$ are provided every iteration by the Davidson eigensolver while solving Eq. (3.20). The BLAS matrix multiplication subroutine has been used for this operation. The cost of the operation per irrep and per partner is $N_r N_p N_n$, where N_r is the number of grid points, N_p is the dimension of products of occupied and virtual molecular orbital basis sets, and N_n is the size of the set of approximate eigenvectors $\{x_{p\sigma}^n\}$.

The next step is the calculation of the response of the XC-functional $\delta v_{\sigma\sigma'}^{n\tau\Gamma\gamma}(\boldsymbol{r})$ (we omit the symbol XC for brevity here). For that, one multiplies the response of the density $\delta\rho_\sigma^{n\tau\Gamma\gamma}(\boldsymbol{r})$ with the exchange-correlation kernel $f_{\mathrm{XC}}^{\sigma\sigma'}(\boldsymbol{r})$.

$$\delta v_\sigma^{n\tau\Gamma\gamma}(\boldsymbol{r}) = \sum_{\sigma'} f_{\mathrm{XC}}^{\sigma\sigma'}(\boldsymbol{r}) \delta\rho_{\sigma'}^{n\tau\Gamma\gamma}(\boldsymbol{r}) \tag{3.70}$$

The cost of the operation per irrep and per partner is $N_r N_n$, where N_r is the number of grid points, N_n is the size of the set of approximate eigenvectors $\{x_{p\sigma}^n\}$.

The next two operations are implemented in the integration procedure. The method (a) is integration of the symmetrized functions $\Phi_{p\sigma}^{\tau\Gamma\gamma}(\boldsymbol{r})$, of the size $N_p N_r$ with the response of the XC-functional, $\delta v_{\sigma\sigma'}^{n\tau\Gamma\gamma}(\boldsymbol{r})$, of the size $N_r N_n$:

$$\begin{aligned} \Upsilon_{p\sigma}^{n\tau\Gamma} &= \frac{1}{\dim\Gamma} \sum_\gamma \int d^3\boldsymbol{r}\, \Phi_{p\sigma}^{\tau\Gamma\gamma}(\boldsymbol{r}) \delta v_\sigma^{n\tau\Gamma\gamma}(\boldsymbol{r}) \\ &\simeq \frac{1}{\dim\Gamma} \sum_\gamma \sum_{\boldsymbol{r}} w(\boldsymbol{r}) \Phi_{p\sigma}^{\tau\Gamma\gamma}(\boldsymbol{r}) \delta v_\sigma^{n\tau\Gamma\gamma}(\boldsymbol{r}), \end{aligned} \tag{3.71}$$

where $w(\boldsymbol{r})$ are the weights of the grid points [57]. In the method (b) one evaluates the matrix elements of the XC-potential response for each pair of the partners γ_a and γ_s of

the orbital sets $\{\varphi_{a\sigma}^{\Gamma_a\gamma_a},\ \gamma_a = 1..\dim\Gamma_a\}$ and $\{\varphi_{s\sigma}^{\Gamma_s\gamma_s},\ \gamma_s = 1..\dim\Gamma_s\}$:

$$\langle a\sigma\Gamma_a\gamma_a|\delta v_\sigma^{n\tau\Gamma\gamma}|s\sigma\Gamma_s\gamma_s\rangle \simeq \sum_{\boldsymbol{r}} w(\boldsymbol{r})\varphi_{a\sigma}^{\Gamma_a\gamma_a}(\boldsymbol{r})\delta v_\sigma^{n\tau\Gamma\gamma}(\boldsymbol{r})\varphi_{s\sigma}^{\Gamma_s\gamma_s}(\boldsymbol{r}). \tag{3.72}$$

That is followed by the symmetry adaption of the resulting integrals, Eq. (3.72), by reducing them with the help of Clebsch–Gordon $C^{\tau\Gamma\gamma}_{\Gamma_a\gamma_a,\Gamma_s\gamma_s}$:

$$Y_{p\sigma}^{n\tau\Gamma} = \frac{1}{\dim\Gamma}\sum_{\gamma}\sum_{\gamma_a\gamma_s} C^{\tau\Gamma\gamma}_{\Gamma_a\gamma_a,\Gamma_s\gamma_s}\langle a\sigma\Gamma_a\gamma_a|\delta v_\sigma^{n\tau\Gamma\gamma}|s\sigma\Gamma_s\gamma_s\rangle \tag{3.73}$$

The cost of operations (a) and (b) per irrep and per partner is N_rN_p, where N_r is the number of grid points, N_p is the dimension of products of occupied and virtual molecular orbital basis sets. Here the BLAS subroutine is used for optimal matrix multiplications. Methods (a) and (b) show different performance. Method (b) was from 2 to 12 times faster than method (a) according to the tests on different systems. Another technical advantage of method (b) is that one is able to re-use already implemented and well tested code. The result $Y_{p\sigma}^{n\tau\Gamma}$ of the last step will be returned to the eigensolver.

The calculation of the exchange-correlation potential response is effectively parallelized over the grid points. The two-center functions $\Phi_{p\sigma}$ are split along the dimension N_p between processors as N_p/n, where n is the number of processors, see Section 3.1.3.

3.3.6 Numerical quadrature for the GGA exchange-correlation integrals

In the previous section we described the evaluation of the numerical quadrature for four-index LDA exchange-correlation integral. In this section we will extend the description of the integration scheme for GGA exchange-correlation functionals. The terms and expressions common both to GGA and LDA from Section 3.3.3 will be omitted. We will again use the analogy between the expression for the XC response kernel representation $F_{p\sigma,p'\sigma'}$, Eq. (3.59), and for two-index XC response kernel representation $R_{k\sigma,k'\sigma'}$, Eq. (3.45), and we will use the alternative expressions for k , Eq. (3.61), and $\boldsymbol{\nabla}k$, Eq. (3.62). For GGA as well as for LDA we do not explicitly calculate the four-index integrals $F_{p\sigma,p'\sigma'}$, Eq. (3.59), but instead we calculate the product of the trial eigenvector $x_{p\sigma}^n$ with four-index GGA exchange-correlation integral $F_{p\sigma,p'\sigma'}$, Eq. (3.59). In the actual implementation the numerical quadrature for the GGA functionals is done in five steps.

For the numerical quadrature of GGA exchange-correlation functionals we calculate not only the values of the molecular KS-orbitals $\varphi_{i\sigma}^{\Gamma\gamma}(\boldsymbol{r})$ on the grid of points $\boldsymbol{r}$ from eigenvectors $E_{in\sigma}^{\Gamma}$ and values of the orbital basis functions $\chi_n^{\Gamma\gamma}(\boldsymbol{r})$, Eq. (3.68), but also the gradients of molecular KS-orbitals $\boldsymbol{\nabla}\varphi_{i\sigma}^{\Gamma\gamma}(\boldsymbol{r})$, from the values of the gradient of the

orbital basis functions $\boldsymbol{\nabla}\chi_n^{\Gamma\gamma}(\boldsymbol{r})$.

$$\boldsymbol{\nabla}\varphi_{i\sigma}^{\Gamma\gamma}(\boldsymbol{r}) = \sum_n E_{in\sigma}^{\Gamma}\boldsymbol{\nabla}\chi_n^{\Gamma\gamma}(\boldsymbol{r}) \tag{3.74}$$

Below we will distinguish the gradient of the occupied molecular orbitals $\boldsymbol{\nabla}\varphi_{a\sigma}^{\Gamma\gamma}(\boldsymbol{r})$ and the gradient of unoccupied molecular orbitals $\boldsymbol{\nabla}\varphi_{s\sigma}^{\Gamma\gamma}(\boldsymbol{r})$. This operation has been implemented using the BLAS matrix multiplication subroutine as well. The additional cost of the operation per irreducible representation and per partner when compared to the LDA code is of the order $3N_rN_\chi$, where N_r is the number of grid points and N_χ is the dimension of the orbital basis set.

In the next step in addition to the two-center functions $\Phi_{p\sigma}^{\tau\Gamma\gamma}(\boldsymbol{r})$, Eq. (3.60), one computes also the gradient of the two-center function $\boldsymbol{\nabla}\Phi_{p\sigma}^{\tau\Gamma\gamma}(\boldsymbol{r})$ from the products and gradients of occupied and virtual orbitals. Symmetry adaption is done with the help of Clebsch–Gordon coefficients $C^{\tau\Gamma\gamma}_{\Gamma_a\gamma_a,\Gamma_s\gamma_s}$:

$$\boldsymbol{\nabla}\Phi_{p\sigma}^{\tau\Gamma\gamma}(\boldsymbol{r}) = C^{\tau\Gamma\gamma}_{\Gamma_a\gamma_a,\Gamma_s\gamma_s}\left(\boldsymbol{\nabla}\varphi_{a\sigma}^{\Gamma_a\gamma_a}(\boldsymbol{r})\varphi_{s\sigma}^{\Gamma_s\gamma_s}(\boldsymbol{r}) + \varphi_{a\sigma}^{\Gamma_a\gamma_a}(\boldsymbol{r})\boldsymbol{\nabla}\varphi_{s\sigma}^{\Gamma_s\gamma_s}(\boldsymbol{r})\right) \tag{3.75}$$

The additional cost of the operation per irreducible representation and per partner when compared to LDA is of the order $6N_rN_p$, where N_r is the number of grid points and N_p is the dimension of the product space of occupied and virtual molecular orbitals.

The symmetry-adapted basis functions together with the set of approximate eigenvectors $\{x_{p\sigma}^n\}$ are used to calculate in addition to the response of the density, the gradient of the response of the density. Again we will use the set of approximate eigenvectors $\{x_{p\sigma}^n\}$ provided every iteration by the Davidson eigensolver while solving the Casida eigenvalue problem, Eq. (3.20):

$$\delta\boldsymbol{\nabla}\rho_\sigma^{n\tau\Gamma\gamma}(\boldsymbol{r}) = \sum_p \boldsymbol{\nabla}\Phi_{p\sigma}^{\tau\Gamma\gamma}(\boldsymbol{r})x_{p\sigma}^n \tag{3.76}$$

The BLAS matrix multiplications subroutine is used for this operation. The additional cost of the operation per irreducible representation and per partner is $3N_rN_pN_n$, where N_r is the number of grid points and N_p is the dimension of product space of occupied and virtual molecular orbitals, N_n is the size of the set of approximate eigenvectors $\{x_{p\sigma}^n\}$.

The fourth step is the calculation of the response of the XC-potential. For those calculations we introduce three auxiliary vector functions $\boldsymbol{a}_\sigma^{n\tau\Gamma\gamma}(\boldsymbol{r})$, $\boldsymbol{b}_\sigma^{n\tau\Gamma\gamma}(\boldsymbol{r})$, $\boldsymbol{c}_\sigma^{n\tau\Gamma\gamma}(\boldsymbol{r})$,

the origin of which is Eq. (3.51):

$$\begin{aligned}
\boldsymbol{a}_\sigma^{n\tau\Gamma\gamma} &= \sum_{\sigma'} \delta\boldsymbol{\nabla}\rho_{\sigma'}^{n\tau\Gamma\gamma}\left(\frac{\partial}{\partial\gamma_{\sigma'\sigma}}+\frac{\partial}{\partial\gamma_{\sigma\sigma'}}\right)\epsilon_{\mathrm{XC}} \\
\boldsymbol{b}_\sigma^{n\tau\Gamma\gamma} &= \sum_{\sigma'} \delta\rho_{\sigma'}^{n\tau\Gamma\gamma}\sum_{\zeta}\boldsymbol{\nabla}\rho_{\zeta}^{n\tau\Gamma\gamma}\left(\frac{\partial^2}{\partial\rho_\sigma\partial\gamma_{\sigma'\zeta}}+\frac{\partial^2}{\partial\rho_\sigma\partial\gamma_{\zeta\sigma'}}\right)\epsilon_{\mathrm{XC}} \\
\boldsymbol{c}_\sigma^{n\tau\Gamma\gamma} &= \sum_{\sigma'}\sum_{\zeta,\zeta'}\boldsymbol{\nabla}\rho_{\zeta}^{n\tau\Gamma\gamma}\left(\boldsymbol{\nabla}\rho_{\zeta'}\delta\boldsymbol{\nabla}\rho_{\sigma'}\right) \\
&\times \left(\frac{\partial^2}{\partial\gamma_{\sigma\zeta}\partial\gamma_{\sigma'\zeta'}}+\frac{\partial^2}{\partial\gamma_{\zeta\sigma}\partial\gamma_{\sigma'\zeta'}}+\frac{\partial^2}{\partial\gamma_{\sigma\zeta}\partial\gamma_{\zeta'\sigma'}}+\frac{\partial^2}{\partial\gamma_{\zeta\sigma}\partial\gamma_{\zeta'\sigma'}}\right)\epsilon_{\mathrm{XC}}
\end{aligned} \tag{3.77}$$

and the auxiliary scalar function $d_\sigma^{n\tau\Gamma\gamma}(\boldsymbol{r})$, as in Eq. (3.51):

$$d_\sigma^{n\tau\Gamma\gamma} = \sum_{\sigma'}\sum_{\zeta}\left(\boldsymbol{\nabla}\rho_{\zeta}^{n\tau\Gamma\gamma}\delta\boldsymbol{\nabla}\rho_{\sigma'}^{n\tau\Gamma\gamma}\right)\left(\frac{\partial^2}{\partial\rho_\sigma\partial\gamma_{\sigma'\zeta}}+\frac{\partial^2}{\partial\rho_\sigma\partial\gamma_{\zeta\sigma'}}\right)\epsilon_{\mathrm{XC}}. \tag{3.78}$$

Indices σ, σ' and ζ, $\zeta'$are spin indices. Here and below we omit the explicit dependence of quantities on $\boldsymbol{r}$.

The next two operations of the XC quadrature are implemented in the integration procedure in two ways. Method (a) is the integration of the symmetrized functions product, $\Phi_{p\sigma}^{\tau\Gamma\gamma}(\boldsymbol{r})$, with the response of the XC-functional for LDA $\delta v_\sigma^{n\tau\Gamma\gamma}(\boldsymbol{r})$ and scalar function $d_\sigma^{n\tau\Gamma\gamma}(\boldsymbol{r})$, and integration of the gradients of the symmetrized function product, $\boldsymbol{\nabla}\Phi_{p\sigma}^{\tau\Gamma\gamma}(\boldsymbol{r})$, with the auxiliary vector functions $\boldsymbol{a}_\sigma^{n\tau\Gamma\gamma}(\boldsymbol{r})$, $\boldsymbol{b}_\sigma^{n\tau\Gamma\gamma}(\boldsymbol{r})$, $\boldsymbol{c}_\sigma^{n\tau\Gamma\gamma}(\boldsymbol{r})$.

$$\begin{aligned}
Y_{p\sigma}^{n\tau\Gamma} &\simeq \frac{1}{\dim\Gamma}\sum_{\gamma}\sum_{\boldsymbol{r}} w\,\left(\Phi_{p\sigma}^{\tau\Gamma\gamma}(\delta v_\sigma^{n\tau\Gamma\gamma}+d_\sigma^{n\tau\Gamma\gamma})\right), \\
&+ \frac{1}{\dim\Gamma}\sum_{\gamma}\sum_{\boldsymbol{r}} w\,\left(\boldsymbol{\nabla}\Phi_{p\sigma}^{\tau\Gamma\gamma}(\boldsymbol{a}_\sigma^{n\tau\Gamma\gamma}+\boldsymbol{b}_\sigma^{n\tau\Gamma\gamma}+\boldsymbol{c}_\sigma^{n\tau\Gamma\gamma})\right)
\end{aligned} \tag{3.79}$$

Here $w = w(\boldsymbol{r})$ are the weights of the grid points [57]. In method (b) one evaluates the matrix elements of the XC-potential response for each pair of the partners γ_a and γ_s of the orbital sets $\{\varphi_{a\sigma}^{\Gamma_a\gamma_a}(\boldsymbol{r}),\ \gamma_a = 1..\dim\Gamma_a\}$ and $\{\varphi_{s\sigma}^{\Gamma_s\gamma_s}(\boldsymbol{r}),\ \gamma_s = 1..\dim\Gamma_s\}$

$$\begin{aligned}
\langle a\sigma\Gamma_a\gamma_a|\delta v_\sigma^{n\tau\Gamma\gamma}|s\sigma\Gamma_s\gamma_s\rangle &\simeq \sum_{\boldsymbol{r}} w\,\left(\varphi_{a\sigma}^{\Gamma_a\gamma_a}(\delta v_\sigma^{n\tau\Gamma\gamma}+d_\sigma^{n\tau\Gamma\gamma})\varphi_{s\sigma}^{\Gamma_s\gamma_s}\right) \\
&+ \sum_{\boldsymbol{r}} w\,\left(\boldsymbol{\nabla}\varphi_{a\sigma}^{\Gamma_a\gamma_a}(\boldsymbol{a}_\sigma^{n\tau\Gamma\gamma}+\boldsymbol{b}_\sigma^{n\tau\Gamma\gamma}+\boldsymbol{c}_{\sigma'}^{n\tau\Gamma\gamma})\varphi_{s\sigma}^{\Gamma_s\gamma_s}\right) \\
&+ \sum_{\boldsymbol{r}} w\,\left(\varphi_{a\sigma}^{\Gamma_a\gamma_a}(\boldsymbol{a}_\sigma^{n\tau\Gamma\gamma}+\boldsymbol{b}_\sigma^{n\tau\Gamma\gamma}+\boldsymbol{c}_\sigma^{n\tau\Gamma\gamma})\boldsymbol{\nabla}\varphi_{s\sigma}^{\Gamma_s\gamma_s}\right)
\end{aligned} \tag{3.80}$$

Here we again omit the explicit dependence of the quantities on the grid points $\boldsymbol{r}$. The integration is followed by the symmetry adaption of the resulting integrals, Eq. (3.80),

by reducing them with the help of Clebsch–Gordon coefficients $C^{\tau\Gamma\gamma}_{\Gamma_a\gamma_a,\Gamma_s\gamma_s}$:

$$Y^{n\tau\Gamma}_{p\sigma} = \frac{1}{\dim\Gamma}\sum_{\gamma}\sum_{\gamma_a\gamma_s} C^{\tau\Gamma\gamma}_{\Gamma_a\gamma_a,\Gamma_s\gamma_s}\langle a\sigma\Gamma_a\gamma_a|\delta v^{n\tau\Gamma\gamma}_{\sigma}|s\sigma\Gamma_s\gamma_s\rangle \tag{3.81}$$

Here, too, a BLAS subroutine is used for optimal matrix multiplications. The difference between the two methods (a) and (b) is in performance, see Sec. 3.3.5. The result of the last step will be returned to the Davidson eigensolver.

The numerical quadrature of the exchange-correlation potential response is efficiently parallelized over the grid points. The two-center functions $\Phi_{p\sigma}$ and $\nabla\Phi_{p\sigma}$ are split over the dimension N_p between processors in blocks of the size N_p/n, where n is number of processors, see Section 3.1.3.

3.4 Evaluation of the exchange-correlation kernel: LDA and GGA

In this section we will explain the evaluation of the exchange-correlation kernel. At the moment, the following exchange-correlation functionals with second-order derivatives are available in PARAGAUSS:

- Local density exchange functional (X_α with $\alpha = 2/3$) [20]
- Vosko, Wilk, Nusair (VWN) local density correlation functional (VWN) [21]
- Perdew and Wang local density correlation functional (PW LDA) [16]
- Becke generalized gradients approximation exchange functional (B88) [13]
- Perdew generalized gradients approximation correlation functional (P86) [14]
- Perdew and Wang generalized gradients approximation exchange-correlation functional (PW91) [15]
- Perdew, Burke and Ernzernhof generalized gradients approximation exchange-correlation functional and its revised versions (PBE, PBEN, revPBE) [17–19].

The exchange-correlation kernel for TDDFT calculation involves the second-order derivative of the exchange-correlation energy density ϵ_{XC}, Eqs. (3.50) and (3.51). To evaluate the LDA exchange-correlation kernel, we have to determine the second-order derivatives $\partial^2\epsilon_{\mathrm{XC}}/\partial\rho_\sigma\partial\rho_{\sigma'}$ of exchange-correlation function with respect to the density. In the case of GGA, we additionally need to evaluate the mixed second-order derivatives with respect to the density and the gradient of density $\partial^2\epsilon_{\mathrm{XC}}/\partial\rho_\sigma\partial\boldsymbol{\nabla}\rho_{\sigma'}$, and the second-order derivative with respect to the gradient of the densities $\partial^2\epsilon_{\mathrm{XC}}/\partial\boldsymbol{\nabla}\rho_\sigma\partial\boldsymbol{\nabla}\rho_{\sigma'}$ as well. In PARAGAUSS the XC functional for open-shell

systems depends on the two densities $\rho_\uparrow$ and $\rho_\downarrow$. The GGA XC functional in addition depends on the gradients of the density via the scalar variables $\gamma_{\uparrow\uparrow} = |\boldsymbol{\nabla}\rho_\uparrow|^2$, $\gamma_{\downarrow\downarrow} = |\boldsymbol{\nabla}\rho_\downarrow|^2$, and $\gamma_{\uparrow\downarrow} = (\boldsymbol{\nabla}\rho_\uparrow \boldsymbol{\nabla}\rho_\downarrow)$, see Appendix D.

The exchange-correlation function ϵ_{XC} is conventionally separated into two terms: the exchange term with the exchange density $\epsilon_{\mathrm{X}}(\rho_\uparrow, \rho_\downarrow, \gamma_{\uparrow\uparrow}, \gamma_{\uparrow\downarrow}, \gamma_{\downarrow\downarrow})$ and the correlation term with the corresponding correlation density $\epsilon_{\mathrm{C}}(\rho_\uparrow, \rho_\downarrow, \gamma_{\uparrow\uparrow}, \gamma_{\uparrow\downarrow}, \gamma_{\downarrow\downarrow})$:

$$\epsilon_{\mathrm{XC}} = \epsilon_{\mathrm{X}} + \epsilon_{\mathrm{C}}. \tag{3.82}$$

The most general exchange density in a spin-polarized system is a sum of two contributions [58]:

$$\epsilon_{\mathrm{X}}[\rho_\uparrow, \rho_\downarrow] = \frac{1}{2}\epsilon_{\mathrm{X}}[2\rho_\uparrow] + \frac{1}{2}\epsilon_{\mathrm{X}}[2\rho_\downarrow]. \tag{3.83}$$

We will start our explanation from the simplest case, the X_α LDA exchange functional [20].

LDA exchange functional: X_α

The local density exchange approximation of the X_α functional is a significant contribution to the XC-functional which serves as a basis for GGA exchange functionals. In general it can be written as [58]

$$E_{X_\alpha}(\rho_\uparrow, \rho_\downarrow) = \frac{1}{2}\int d^3\boldsymbol{r}\, \left(\epsilon_{X_\alpha}(2\rho_\uparrow) + \epsilon_{X_\alpha}(2\rho_\downarrow)\right). \tag{3.84}$$

Here ϵ_{X_α} is the exchange density for the X_α functional [20]:

$$\epsilon_{X_\alpha}(\rho_\sigma) = -\left(\frac{3}{2}\alpha\right)\frac{3}{4}\left(\frac{3}{\pi}\right)^{1/3}\rho_\sigma^{4/3}. \tag{3.85}$$

The first- and second-order derivatives of the exchange energy density with respect to the density ρ_σ are given by the following expressions:

$$\epsilon'_{X_\alpha}(\rho_\sigma) = -\left(\frac{3}{2}\alpha\right)\left(\frac{3}{\pi}\right)^{1/3}\rho_\sigma^{1/3}, \tag{3.86}$$

$$\epsilon''_{X_\alpha}(\rho_\sigma) = -\left(\frac{3}{2}\alpha\right)\frac{1}{3}\left(\frac{3}{\pi}\right)^{1/3}\rho_\sigma^{-2/3}. \tag{3.87}$$

Note, that the mixed second-order derivatives $\partial^2\epsilon_{X_\alpha}/\partial\rho_\uparrow\partial\rho_\downarrow$ is equal to zero, according to the equation for general exchange density, Eq. (3.83).

GGA exchange energy functionals

Generalized gradients approximations (GGA) of the energy functional are constructed as a correction of the LDA functional in such a way that they fulfill as many exact scaling and asymptotic properties of the hypothetical exact energy functional as possible [13, 15, 17]. The GGA XC functional depends on the electron density and the gradient of the electron density.

The exchange energy function of the open shell system consists of the LDA exchange energy function ϵ_{X_α}, Eq. (3.85), and the GGA correction to the LDA expression introduced as a scaling factor $F(s^2)$ [13, 15, 17]:

$$\epsilon_X[\rho_\sigma] = \epsilon_{X_\alpha}(\rho_\sigma)F(s^2). \tag{3.88}$$

which depends on the square of the generalized density gradient s^2:

$$s^2 = \frac{1}{(3\pi^2)^{2/3}}\frac{\gamma_{\sigma\sigma}}{\rho_\sigma^{8/3}}, \tag{3.89}$$

This exchange energy functional is applied to both density contributions $\rho_\uparrow$ and $\rho_\downarrow$, as suggested by the general form of the exchange density, Eq. (3.83). The first-order derivatives of the exchange energy density with respect to the density ρ_σ and the density gradient measure $\gamma_{\sigma\sigma}$ are:

$$\frac{\partial\epsilon_X}{\partial\rho_\sigma} = \epsilon'_{X_\alpha}F + \epsilon_{X_\alpha}F'(s^2)'_{\rho_\sigma}, \tag{3.90}$$

$$\frac{\partial\epsilon_X}{\partial\gamma_{\sigma\sigma}} = \epsilon_{X_\alpha}F'(s^2)'_{\gamma_{\sigma\sigma}}. \tag{3.91}$$

The second-order derivatives of the exchange energy density with respect to the density ρ_σ and the density gradient measure $\gamma_{\sigma\sigma}$ are:

$$\frac{\partial^2\epsilon_X}{\partial\rho_\sigma^2} = \epsilon''_{X_\alpha}F + 2\epsilon'_{X_\alpha}F'(s^2)'_{\rho_\sigma} + \epsilon_{X_\alpha}F''((s^2)'_{\rho_\sigma})^2 + \epsilon_{X_\alpha}F'(s^2)''_{\rho_\sigma}, \tag{3.92}$$

$$\frac{\partial^2\epsilon_X}{\partial\rho_\sigma\partial\gamma_{\sigma\sigma}} = \epsilon'_{X_\alpha}F'(s^2)'_{\gamma_{\sigma\sigma}} + \epsilon_{X_\alpha}F''(s^2)'_{\rho_\sigma}(s^2)'_{\gamma_{\sigma\sigma}} + \epsilon_{X_\alpha}F'(s^2)''_{\rho_\sigma\gamma_{\sigma\sigma}}, \tag{3.93}$$

$$\frac{\partial^2\epsilon_X}{\partial\gamma_{\sigma\sigma}^2} = \epsilon_{X_\alpha}F''((s^2)'_{\gamma_{\sigma\sigma}})^2 + \epsilon_{X_\alpha}F'(s^2)''_{\gamma_{\sigma\sigma}}. \tag{3.94}$$

The first-order derivatives of the square of the generalized density gradients with respect to the density ρ_σ and with respect to the density gradient measure $\gamma_{\sigma\sigma}$ are:

$$(s^2)'_{\rho_\sigma} = -\frac{8}{3}\frac{1}{(3\pi^2)^{2/3}}\frac{\gamma_{\sigma\sigma}}{\rho_\sigma^{11/3}}, \tag{3.95}$$

$$(s^2)'_{\gamma_{\sigma\sigma}} = \frac{1}{(3\pi^2)^{2/3}}\frac{1}{\rho_\sigma^{8/3}}. \tag{3.96}$$

The second-order derivatives of the square of the generalized density gradients with respect to the density ρ_σ and with respect to the density gradient measure $\gamma_{\sigma\sigma}$ are:

$$(s^2)''_{\rho_\sigma\rho_\sigma} = -\frac{88}{9}\frac{1}{(3\pi^2)^{2/3}}\frac{\gamma_{\sigma\sigma}}{\rho_\sigma^{14/3}}, \tag{3.97}$$

$$(s^2)''_{\rho_\sigma\gamma_{\sigma\sigma}} = -\frac{8}{3}\frac{1}{(3\pi^2)^{2/3}}\frac{1}{\rho_\sigma^{8/3}}, \tag{3.98}$$

$$(s^2)''_{\gamma_{\sigma\sigma}\gamma_{\sigma\sigma}} = 0. \tag{3.99}$$

The mixed second-order derivatives $\partial^2\epsilon_X/\partial\rho_\sigma\partial\rho_{\sigma'}$, $\partial^2\epsilon_X/\partial\rho_\sigma\partial\gamma_{\sigma'\sigma'}$, $\partial^2\epsilon_X/\partial\rho_\sigma\partial\gamma_{\sigma\sigma'}$, $\partial^2\epsilon_X/\partial\gamma_{\sigma\sigma}\partial\gamma_{\sigma'\sigma'}$, $\partial^2\epsilon_X/\partial\gamma_{\sigma\sigma'}\partial\gamma_{\sigma\sigma'}$, that involve two different spin $\sigma \neq \sigma'$ orientations, are identically equal to zero.

For the B88 Becke exchange functional [13], the GGA scaling factor is

$$F_{\mathrm{B88}} = \frac{Ds^2}{1 + As\,\sinh^{-1}(Bs)}. \tag{3.100}$$

For the PW91 Perdew–Wang exchange functional [15], the GGA scaling factor is

$$F_{\mathrm{PW91}} = \frac{s^2(D - Cs^2 - E\exp(-100s^2))}{1 + As\sinh^{-1}(Bs) + Cs^4}, \tag{3.101}$$

where $A = 0.19645$, $B = 7.7956$, and $D = 0.2743$ are the same parameters for B88 [13] and PW91 [15] exchange functionals; $C = 0.004$, and $E = 0.1508$ are additional parameters in the case of the PW91 [15] exchange functional.

In the case of the PBE exchange functional [17], the GGA scaling factor is

$$F_{\mathrm{PBE}} = \frac{\kappa\mu s^2}{(\kappa + \mu s^2)}. \tag{3.102}$$

In the case of the PBEN exchange functional [18], the GGA scaling factor is

$$F_{\mathrm{PBEN}} = \kappa\left(1 - \exp\left(\frac{-\mu s^2}{\kappa}\right)\right), \tag{3.103}$$

where $\kappa = 0.804$ and $\mu = 0.2195$ are the same parameters for PBE [17] and PBEN [18] exchange functionals.

GGA correlation energy functional

The correlation energy can be separated into two parts, the LDA correlation energy and the correction due to GGA:

$$E[\rho_\uparrow, \rho_\downarrow] = E_{\mathrm{LDA}}[\rho_\uparrow, \rho_\downarrow] + E_{\mathrm{GGA}}[\rho_\uparrow, \rho_\downarrow] \tag{3.104}$$

where the LDA part of the correlation functional is usually taken either in the parametrization of Vosko, Wilk and Nusair [21] (for the Becke86 GGA correlation see Ref. [13]) or Perdew and Wang [16] (for the PBE GGA functionals see Ref. [17] and PW91 GGA functional see Ref. [15]). The equation for the GGA correlation functional $E_{\mathrm{GGA}}[\rho_\uparrow, \rho_\downarrow]$ is a GGA correction to the LDA part. The GGA correlation functional depends on the GGA energy density per particle $H(A, B, C, D)$

$$E_{\mathrm{GGA}}[\rho_\uparrow, \rho_\downarrow] = \int d^3\boldsymbol{r}\, \rho H(A, B, C, D), \tag{3.105}$$

where $\rho = \rho_\uparrow + \rho_\downarrow$, and the energy density is $\epsilon_{\mathrm{GGA}} = \rho H(A, B, C, D)$.

Next, we will discuss the implementation of the GGA correction, $E_{\mathrm{GGA}}[\rho_\uparrow, \rho_\downarrow]$. The GGA correlation energy density per particle H depends on four auxiliary intermediate quantities $A(\rho_\uparrow, \rho_\downarrow, \gamma)$, $B(\rho_\uparrow, \rho_\downarrow, \gamma)$, $C(\rho_\uparrow, \rho_\downarrow, \gamma)$, $D(\rho_\uparrow, \rho_\downarrow, \gamma)$, where $\gamma = \gamma_{\uparrow\uparrow} + \gamma_{\downarrow\downarrow} + 2\gamma_{\uparrow\downarrow}$. The first-order derivatives of the GGA correlation energy density H per particle are given by the chain rule:

$$\frac{\partial \epsilon_{\mathrm{GGA}}}{\partial \rho_\sigma} = H + \rho \left(\sum_{k=A,B,C,D} \frac{\partial H}{\partial k} \frac{\partial k}{\partial \rho_\sigma} \right), \tag{3.106}$$

$$\frac{\partial \epsilon_{\mathrm{GGA}}}{\partial \gamma} = \rho \left(\sum_{k=A,B,C,D} \frac{\partial H}{\partial k} \frac{\partial k}{\partial \gamma} \right). \tag{3.107}$$

The second-order derivatives of the GGA correlation energy density H per particle are obtained by applying the chain rule twice:

$$\begin{aligned} \frac{\partial^2 \epsilon_{\mathrm{GGA}}}{\partial \rho_\sigma \partial \rho_{\sigma'}} &= \sum_{k=A,B,C,D} \frac{\partial H}{\partial k} \frac{\partial k}{\partial \rho_\sigma} + \sum_{k=A,B,C,D} \frac{\partial H}{\partial k} \frac{\partial k}{\partial \rho_{\sigma'}} \\ &+ \rho \sum_{k=A,B,C,D} \left(\frac{\partial H}{\partial k} \frac{\partial^2 k}{\partial \rho_\sigma \partial \rho_{\sigma'}} + \sum_{l=A,B,C,D} \frac{\partial^2 H}{\partial k \partial l} \frac{\partial k}{\partial \rho_\sigma} \frac{\partial l}{\partial \rho_{\sigma'}} \right), \end{aligned} \tag{3.108}$$

$$\begin{aligned} \frac{\partial^2 \epsilon_{\mathrm{GGA}}}{\partial \rho_\sigma \partial \gamma} &= \sum_{k=A,B,C,D} \frac{\partial H}{\partial k} \frac{\partial k}{\partial \rho_\sigma} \\ &+ \rho \sum_{k=A,B,C,D} \left(\frac{\partial H}{\partial k} \frac{\partial^2 k}{\partial \rho_\sigma \partial \gamma} + \sum_{l=A,B,C,D} \frac{\partial^2 H}{\partial k \partial l} \frac{\partial k}{\partial \rho_\sigma} \frac{\partial l}{\partial \gamma} \right), \end{aligned} \tag{3.109}$$

$$\frac{\partial^2 \epsilon_{\mathrm{GGA}}}{\partial \gamma^2} = \rho \sum_{k=A,B,C,D} \left(\frac{\partial H}{\partial k} \frac{\partial^2 k}{\partial \gamma^2} + \sum_{l=A,B,C,D} \frac{\partial^2 H}{\partial k \partial l} \frac{\partial k}{\partial \gamma} \frac{\partial l}{\partial \gamma} \right). \tag{3.110}$$

As an example, we provide the correlation energy density H per particle for the PBE GGA correlation functional [17]:

$$H_{\mathrm{PBE}}(\phi, t, \epsilon_c) = \frac{e^2}{a_0}\gamma\phi^3 \ln\{1 + \frac{\beta}{\gamma}t^2\left(\frac{1+Zt^2}{1+Zt^2+Z^2t^4}\right)\} \tag{3.111}$$

Here, the auxiliary quantity Z depends on the LDA correlation energy density ϵ_{LDA}

$$Z = \frac{\beta}{\gamma}[\exp\{-\epsilon_{\mathrm{LDA}}/(\gamma\phi^3 e^2/a_0)\} - 1]^{-1} \tag{3.112}$$

We choose to define the auxiliary function A for the PBE correlation functional as a spin-scaling factor ϕ:

$$A := \phi \;=\; \left((1+\zeta)^{2/3} + (1-\zeta)^{2/3}\right)/2,\; \zeta = \frac{\rho_\uparrow - \rho_\downarrow}{\rho_\uparrow + \rho_\downarrow} \tag{3.113}$$

The auxiliary function B for the PBE correlation functional is a dimensionless density gradient t:

$$B := t = \frac{|\boldsymbol{\nabla}\rho|}{2\phi k_s \rho} \tag{3.114}$$

Here the quantity k_s is the Thomas-Fermi screening constant [17]. The auxiliary function C of the PBE correlation functional is the LDA correlation functional ϵ_{LDA}:

$$C := \epsilon_{\mathrm{LDA}}. \tag{3.115}$$

Note that there is no D auxiliary function for the PBE correlation functional. The quantity e^2/a_0 is equal to one in the Hartree atomic units system. $\beta = 0.066725$ and $\gamma = 0.031091$ are parameters [17].

For the PW91 correlation functional [15] we write the GGA correlation energy density (per particle) $H = H_{\mathrm{PBE}} + H_{\mathrm{PW91}}$. Here the GGA correlation energy density H_{PBE} per particle is taken from the PBE functional, Eq. (3.111), with values for the parameters $\gamma = 0.02474$ and $\beta = 0.06726$, and the function H_{PW91} is

$$\begin{aligned} H_{\mathrm{PW91}}(r_s, \phi, t) &= \nu(C_c(r_s) - C_c(0) - 3C_x/7)\phi^3 t^2 \\ &\times \exp[-100\delta\phi^4 t r_s] \end{aligned} \tag{3.116}$$

where the spin-scaling factor ϕ is taken in the form of Eq. (3.113), the dimensionless density gradient t is taken in the form of Eq. (3.114) and the auxiliary function D is taken as the local Seitz radius r_s [15]:

$$D := r_s = \left(\frac{3}{4\pi\rho}\right)^{1/3} \tag{3.117}$$

The function $C_c(r_s)$ can be found in Ref. [59]. The quantities $\nu = 15.7559$, $C_c(0) = 0.004235$, $C_x = -0.001667$, and $\delta = 0.66344$ are parameters [15].

3.5 Evaluation and performance of the TDDFT module of PARAGAUSS

The performance of the TDDFT module of PARAGAUSS

Finally, we discuss the performance of the new TDDFT module of the program package PARAGAUSS with respect to its computational demands. Benchmark calculations were carried out with the LDA exchange-correlation potential (SVWN, i.e. X_α exchange, with $\alpha = 2/3$ [20] and VWN correlation [21] functionals) and the GGA exchange-correlation potential (BP86 [13, 14]). For the evaluation of the parallel performance the calculations were carried out with 2, 4, and 8 processors. The 30 lowest excitation energies of each irreducible representation were examined. To investigate the scaling of the new TDDFT code we compared the wall-clock time required for each run.

We have chosen the Cu_2 dimer deposited on the (001) surface of MgO represented by the cluster model $Mg_{10}O_{10}$ as a test system. This system belongs to the C_s point group symmetry. The orbital basis set for Cu was ($16s13p7d \rightarrow 7s5p4d$) and the auxiliary basis set was ($16s13r^2 5p5d$) [32, 33].

The results of the time measurements for Cu_2 on $Mg_{10}O_{10}$ are collected in Tables 3.2 and 3.3. On two processors, the calculation of this system takes two hours for the LDA XC potential and seven hours for the GGA XC potential. The most time consuming parts are the calculation of the density response on the grid, Eqs. (3.69) and (3.76), and the numerical quadrature of the XC potential response, Eq. (3.63). The TDDFT calculation with the LDA XC potential (see Table 3.2) is 2.3 times slower than the SCF calculation. The TDDFT calculation with the GGA XC potential (see Table 3.3) is 7 times slower than the SCF calculation. The factor 3 reflects the fact that the GGA XC potential, formally, is an extension of the LDA XC potential, see Section 3.3.6, Eqs. (3.72) and (3.80). Comparison of the ratio of timings, R, for 4 and 8 processors shows essentially ideal scaling of the TDDFT module of PARAGAUSS, at least for these typical numbers of processors.

Restricting the active space for core and valence excitations by an energy cutoff

The availability of a general and accurate method of treating core excitations, as well as the valence electron transitions separated from the core electron excitations, is highly important. To a large extent, excitations of core electrons do not interfere with the valence electron transitions. This fact can be used to reduce computational costs by

Table 3.2: Timing of the relevant program parts of PARAGAUSS (in s) for the Cu_2 cluster supported on $Mg_{10}O_{10}$, calculated with SVWN LDA exchange correlation functional [20, 21, 60–62].

	(2 proc)	(4 proc)	R[a]	(8 proc)	R[a]
SCF[b]	1952.4	1065.5	1.8	688.5	2.8
TDDFT[c]	4471.1	2251.2	2.0	1141.2	3.9
|-calc. of R, Eq. (3.16)	247.3	123.8	2.0	60.7	4.1
|-calc. of L, Eq. (3.19)	364.9	155.4	2.3	89.0	4.1
\-TDDFT calc.	3858.3	1971.3	2.0	990.8	3.9
|-calc. of diagonal, see Sec. 3.1.3	643.3	343.7	1.9	173.5	3.7
|-calc. of eigensolver and Y, Eq. (3.63)	3151.2	1626.2	1.9	816.0	3.9
|-summary of calc. of $\delta\rho$	1272.2	629.5	2.0	301.4	4.2
|- calc. of χ, Eq. (3.26)	158.4	78.0	2.0	36.9	4.3
|-calc. of φ, Eq. (3.68)	195.7	96.4	2.0	45.0	4.3
|- calc. of $\delta\rho$, Eq. (3.69)	856.2	424.7	2.0	205.0	4.2
\- rest	62.0	30.4	2.0	14.4	4.3
|-calc. of $\frac{\partial^2\epsilon}{\partial\rho^2}$, see Sec. 3.4	135.0	67.1	2.0	31.7	4.3
\-summary of calc. of Y	1738.6	857.7	2.0	412.3	4.2
|- calc. of δv, Eq. (3.70)	131.0	57.6	2.3	28.1	4.7
|-calc. of Y, Eq. (3.63)	1344.5	669.9	2.0	320.9	4.2
\- rest	309.2	130.2	2.4	63.4	4.9
TOTAL (usr)	6423.5	3316.6	1.9	1829.7	3.5
TOTAL (real)	7355.0	3775.0	1.9	2315.0	3.2

[a]) The ratio of timings is denoted by R = Time (2 proc)/Time (n proc)
[b]) Time spent on SCF calculations
[c]) Time spent on TDDFT calculations

neglecting Kohn–Sham eigenstates based on their energy. In the TDDFT calculation one can choose the working space of occupied levels and the working space of virtual orbitals to exclude *a priory* "irrelevant" states. In practice the occupied orbitals can be limited to the core shell under study or, similarly, to the valence shell. The examples below shall demonstrate how sensitive the low excitation energies are to contributions of the core-to-valence excitations.

The supported metal particles Au on Mg_9O_9 and Au_2 on $Mg_{10}O_{10}$ were chosen as test systems. These systems have been calculated with the BP86 GGA XC potential. The orbital basis set for Au was $(22s20p11d7f \rightarrow 9s7p6d4f)$ and the auxiliary basis set was $(22s20r^2 5p5d)$ [32, 33].

With the help of the cutoff of the core levels we include only the 11 electrons of the $5d6s$ valence electronic shells per Au atom, as well as the 2 electrons of the $3s$ valence electronic shell per Mg atom and the 6 electrons of the $2p$ valence electronic shell per O atom in the working space.

As seen from Tables 3.4 and 3.5, the cutoffs of core excitation energies do not influence the results for excitations of valence electrons. The maximal deviation of ex-

Table 3.3: Timing of the relevant program parts of PARAGAUSS (in s) for the Cu_2 cluster supported on $Mg_{10}O_{10}$, calculated with the BP86 GGA exchange correlation functional [13, 14].

	(2 proc)	(4 proc)	R[a]	(8 proc)	R[a]
SCF[b]	2769.6	1428.9	1.9	893.0	3.1
TDDFT[c]	19429.6	9614.3	2.0	4870.4	4.0
|-calc. of R, Eq. (3.16)	1545.3	776.3	2.0	395.8	3.9
|-calc. of L, Eq. (3.19)	421.9	145.6	2.9	74.8	5.6
\-TDDFT calc.	17461.8	8691.7	2.0	4399.1	4.0
|-calc. of diagonal, see Sec. 3.1.3	641.9	327.3	2.0	168.0	3.8
|-calc. of eigensolver and Y, Eq. (3.63)	16818.5	8363.0	2.0	4399.0	3.8
|-summary of calc. of $\delta\rho$	6184.4	3073.5	2.0	1538.9	4.0
|- calc. of χ, Eq. (3.26)	156.7	78.5	2.0	39.1	4.0
|-calc. of φ, Eq. (3.68)	795.2	399.7	2.0	198.7	4.0
|- calc. of $\delta\rho$, Eq. (3.69)	5171.3	2564.8	2.0	1285.7	4.0
\- rest	61.3	30.6	2.0	15.4	4.0
|-calc. of $\frac{\partial^2\epsilon}{\partial\rho^2}$, see Sec. 3.4	136.2	68.3	2.0	34.5	3.9
\-summary of calc. of Y	10415.4	5153.1	2.0	2576.4	4.0
|- calc. of δv, Eq. (3.70)	733.9	366.4	2.0	183.5	4.0
|-calc. of Y, Eq. (3.63)	9196.8	4556.3	2.0	2276.9	4.0
\- rest	484.7	230.4	2.1	116.0	4.2
TOTAL (usr)	22186.5	11043.2	2.0	5763.5	3.8
TOTAL (real)	24214.0	12263.0	2.0	6553.0	3.7

[a]) The ratio of timings is denoted by R = Time (2 proc)/Time (n proc)
[b]) Time spent on SCF calculations
[c]) Time spent on TDDFT calculations

citation energies is 0.01 eV and that of oscillator strengths is 0.005 a.u. Calculation of excitation energies without inclusion of core electrons in the working space of a TDDFT part is more than twice faster than a calculation with core electrons. Hence, in further calculations one can cut the core electron levels without any significant effect on the results. The excitation energies obtained with cutoffs for virtual orbitals are more sensitive to the inclusion of a complete set of MO's. The maximal deviation of excitation energies is 0.05 eV and oscillator strength -0.012 a. u. Hence, one can use the cutoff for virtual levels, but with careful check of the accuracy.

Investigation of core excitations

Next, we investigated the performance of the TDDFT module for the core excitations of the molecules SO_2 and $TiCl_4$. We will calculate transitions from selected core electron levels to valence levels. We will remove from consideration all valence and virtual electron levels which are not involved in the transitions investigated. Also we will compare our results with the results in the literature [28, 29].

The molecule SO_2 was calculated with the SVWN LDA exchange-correlation potential (X_α exchange, with $\alpha = 2/3$ [20] and VWN correlation [21] functionals). For comparison with the results of Fronzoni et al. [28], we used the LB94 correction for the ground state [63]. The Gaussian-type basis set for the S atom was ($12s9p2d \rightarrow 6s5p2d$), and for the O atoms ($10s4p \rightarrow 3s,2p$). Only the $1s$ and $2p$ orbitals of the S atom and the $1s$ orbital of the O atoms were kept among the occupied levels. For the virtual levels no cutoff was employed.

The results of Ref. [28] were obtained with the ADF program package [26]. The basis set employed for the S and O atoms is an all-electron ZORA basis set, consisting of Slater-type orbitals of the size ($13s9p5d6f$) for the S atom and ($10s6p4d4f$) set for the O atoms (ET-QZ4P-2diff) [28, 64]. The adiabatic local density approximation to the exchange-correlation kernel was employed. For the XC potential in the SCF calculation the LB94 XC potential was employed [63]. The LB94 XC potential was chosen for its correct asymptotic behavior at large electron-nucleus separations [63]. The point group symmetry is C_{2v}. The experimental geometry [65] was used: the S-O distance is 1.432Å and the S-O-S angle is 119.5°.

The present and literature results are compared in Table 3.6. Deviations are in the range 0.1-0.6 eV for excitation energies and 0.03-0.4 a.u. for oscillator strengths. The results of our calculations are in good agreement with those obtained in Ref. [28].

Another test was performed with the molecule $TiCl_4$. The basis set for the Ti atom was chosen to be ($15s11p6d6f$) and for the Cl atoms ($12s9p2d \rightarrow 9s6p2d$). All the occupied levels except $2p$ orbital of the Ti atom were cut from the working space of TDDFT; for the virtual levels no cutoff was employed.

Fronzoni et al. [29] calculated TDDFT excitation spectra of $TiCl_4$ with the ADF program [26]. They used the Slater-type diffuse basis set ET-QZ3P-2diff [28, 64] for the Ti and Cl atoms. The point group symmetry was T_d. The experimental geometry [66] was used: the Ti-Cl bond length is 2.17Å.

The present and literature results are compared in Table 3.7. The discrepancy between the two calculations is about 2.0 eV for excitation energies and about 0.022 a.u. for oscillator strengths. The different methods and algorithms used in PARAGAUSS and ADF could be the reason for such a large disagreement.

Table 3.4: Excitation energies (eV) and oscillator strengths (a.u.) of Au atom supported on MgO and differences due to exclusion of either the occupied core levels or valence levels above the imposed cutoff.

	Reference[a]	5*d* and 6*s*[b]	100 eV[c]	50 eV[c]	20 eV[c]	10 eV[c]
31*e*-36a_1	2.01	0.00	0.00	0.00	0.00	0.00
35a_1-36a_1	2.07	0.01	0.01	0.01	0.02	0.04
14b_2-36a_1	2.14	0.00	0.00	0.00	0.00	0.00
30*e*-36a_1	2.15 [0.008]	0.01 [0.000]	0.01 [0.000]	0.01 [0.000]	0.01 [0.000]	0.01 [0.000]
4a_2-36a_1	2.26	0.00	0.00	0.00	0.00	0.00
34a_1-36a_1	2.37 [0.011]	0.00 [0.000]	0.00 [0.000]	0.00 [0.000]	0.01 [0.000]	0.01 [0.000]
14b_1-36a_1	2.39	0.00	0.00	0.00	0.00	0.00
13b_2-36a_1	2.57	0.00	0.00	0.00	0.00	0.00
29*e*-36a_1	2.61	0.00	0.00	0.00	0.00	0.01
13b_1-36a_1	2.63	0.00	0.00	0.00	0.00	0.00
28*e*-36a_1	2.70 [0.005]	0.00 [0.001]	0.00 [0.001]	0.00 [0.001]	0.00 [0.001]	0.01 [0.001]
12b_1-36a_1	2.72	0.00	0.00	0.00	0.00	0.01
27*e*-36a_1	2.90 [0.004]	0.00 [0.001]	0.00 [0.001]	0.00 [0.001]	0.00 [0.001]	0.00 [0.001]
12b_2-36a_1	2.96	0.00	0.00	0.00	0.00	0.00
3a_2-36a_1	3.13	0.00	0.00	0.00	0.00	0.00
33a_1-36a_1	3.13	0.01	0.01	0.01	0.02	0.04
36a_1-32*e*	3.28 [0.077]	0.00 [0.000]	0.00 [0.000]	0.00 [0.000]	0.01 [-0.002]	0.03 [0.001]
36a_1-37a_1	3.44 [0.001]	0.00 [0.000]	0.00 [0.000]	0.00 [0.000]	0.00 [0.000]	0.00 [0.000]
36a_1-33*e*	3.49	0.00	0.00	0.00	0.00	0.00
26*e*-36a_1	3.53	0.00	0.00	0.00	0.00	0.01
11b_1-36a_1	3.64	0.00	0.00	0.00	0.00	0.00
36a_1-38a_1	3.72 [0.001]	0.00 [0.000]	0.00 [0.000]	0.00 [0.000]	0.00 [0.000]	0.00 [0.000]
36a_1-39a_1	3.88 [0.034]	0.00 [0.000]	0.00 [0.000]	0.00 [0.000]	0.00 [0.000]	0.00 [-0.001]
25*e*-36a_1	3.93	0.00	0.00	0.00	0.00	0.00
32a_1-36a_1	3.93 [0.004]	0.00 [0.000]	0.00 [0.000]	0.00 [0.000]	0.01 [0.000]	0.01 [-0.001]
31a_1-36a_1	3.98 [0.001]	0.00 [0.000]	0.00 [0.000]	0.00 [0.000]	0.01 [0.001]	0.02 [0.002]
36a_1-34*e*	4.01	0.00	0.00	0.00	0.00	0.00
36a_1-40a_1	4.18 [0.058]	0.00 [-0.002]	0.00 [-0.002]	0.00 [-0.002]	0.01 [-0.006]	0.01 [-0.012]
36a_1-35*e*	4.21	0.00	0.00	0.00	0.00	0.00
MAX[d]		0.01 [-0.002]	0.01 [-0.002]	0.01 [-0.002]	0.02 [-0.006]	0.04 [-0.012]
AVG		0.00 [0.000]	0.00 [0.000]	0.00 [0.000]	0.00 [0.001]	0.01 [0.001]
Space[e] A_1	16570	3907	3594	3089	1831	1188
Space A_2	12255	3291	3050	2644	1512	968
Space B_1	14309	3601	3316	2857	1659	1066
Space B_2	14183	3583	3316	2866	1677	1084
Space E	28645	7190	6638	5728	3339	2153
Time, s	1734.92	793.62	755.33	710.95	533.16	434.86

[a]) Reference excitation energies (eV) and oscillator strengths in square brackets (a.u.).
[b]) "5*d* and 6*s*" denotes the system where "core transitions" (from all occupied levels of Au except 5*d* and 6*s*) were excluded.
[c]) "100 eV", "50 eV", "20eV", and "10 eV" denote results corresponding to a cutoff of virtual one-electron levels at 100 eV, 50 eV, 20 eV, and 10 eV, respectively.
[d]) The row labeled "MAX" shows the maximal deviation from the reference; "AVG" denotes the average deviation.
[e]) The size of the active space, $N_{occ}N_{vir}$, for each symmetry term.

Table 3.5: Excitation energies (eV) and oscillator strengths (a.u.) of Au_2 dimer supported on MgO and differences due to exclusion of either the occupied core levels or valence levels above the imposed cutoff.

	Reference[a]	5*d* and 6*s*[b]	20 eV[c]
70a'' - 110a'	2.88 [0.005]	0.00 [0.000]	0.00 [0.000]
69a'' - 110a'	2.92 [0.001]	0.00 [0.000]	0.00 [0.000]
108a'- 110a'	2.92 [0.011]	0.00 [-0.001]	0.00 [-0.002]
109a' - 110a'	2.99 [0.043]	0.01 [0.000]	0.03 [-0.008]
106a' - 110a'	3.07 [0.059]	0.00 [0.002]	0.00 [0.008]
68a'' - 110a'	3.10	0.01	0.01
107a' - 110a'	3.13 [0.001]	0.00 [0.005]	0.00 [0.005]
67a'' - 110a'	3.13 [0.006]	0.00 [-0.004]	0.01 [-0.003]
105a' - 110a'	3.15 [0.002]	0.01 [0.000]	0.01 [0.000]
66a'' - 110a'	3.16	0.00	0.00
104a' - 110a'	3.19 [0.001]	0.00 [0.000]	0.00 [0.000]
65a'' - 110a'	3.20	0.00	0.00
64a'' - 110a'	3.25 [0.004]	0.00 [-0.001]	0.00 [-0.001]
103a' - 110a'	3.33 [0.001]	0.00 [0.000]	0.00 [0.000]
63a'' - 110a'	3.35	0.00	0.00
102a' - 110a'	3.38 [0.001]	0.00 [0.000]	0.00 [0.000]
101a'- 110a'	3.59 [0.012]	0.00 [0.000]	0.00 [0.000]
62a'' - 110a'	3.62 [0.001]	0.00 [0.000]	0.00 [0.000]
100a' - 110a'	3.63 [0.001]	0.00 [0.000]	0.00 [0.000]
99a' - 110a'	3.72 [0.005]	0.00 [0.000]	0.00 [-0.001]
61a'' - 110a'	3.93 [0.003]	0.00 [0.000]	0.00 [0.000]
98a' - 110a'	3.97 [0.006]	0.00 [0.000]	0.01 [-0.001]
60a'' - 110a'	3.99 [0.001]	0.00 [0.000]	0.00 [0.000]
109a' - 71a''	4.18 [0.009]	0.00 [0.000]	0.01 [-0.001]
97a'- 110a'	4.19 [0.024]	0.00 [-0.001]	0.01 [-0.002]
109a' - 111a'	4.21 [0.011]	0.00 [0.000]	0.01 [-0.001]
96a'- 110a'	4.26 [0.011]	0.00 [0.000]	0.01 [0.000]
59a''- 110a'	4.29	0.01	0.00
70a'' - 71a''	4.32	0.00	0.00
MAX[d]		0.01 [0.005]	0.03 [0.008]
AVG		0.00 [0.000]	0.00 [0.000]
Space[e] A$'$	48535	10997	5425
Space A$''$	46156	10692	5235
Time, s	7582.0	3633.0	2949.0

[a]) Reference excitation energies (eV) and oscillator strengths in square brackets (a.u.).
[b]) "5*d* and 6*s*" denotes the system where "core transitions" (from all occupied levels of Au except 5*d* and 6*s*) were excluded.
[c]) "20 eV" denotes results corresponding to a cutoff of virtual one-electron levels of 20 eV.
[d]) The row labeled "MAX" shows the maximal deviation from the reference; "AVG" denotes the average deviation.
[e]) The size of the active space, $N_{occ}N_{vir}$, for each symmetry term.

Table 3.6: Excitation energies (eV) and oscillator strengths f (a.u.) for the first three core-to-valence transitions from the S 1s, O 1s, and S 2p levels of SO_2 in the TDDFT approach.

		PARAGAUSS		ADF[a]	
Initial state	Final state (Term)	E[b], eV	$f \times 10^2$	E[b], eV	$f \times 10^2$
S 1s	$3b_1(B_1)$	(2449.66)	0.630	(2438.07)	0.581
	$9a_1(A_1)$	4.84	0.270	4.27	0.220
	$6b_2(B_2)$	5.81	0.280	5.22	0.211
O 1s	$3b_1(B_1)$	(534.15)	4.560	(526.75)	4.331
	$9a_1(B_2)$	4.75	2.820	4.36	1.821
	$6b_2(A_1)$	5.75	2.010	5.31	1.731
S 2p	$9a_1(B_1)$	(170.23)	2.220	(168.95)	2.421
	$3b_1(B_1)$	-4.95	0.090	-4.67	0.162
	$3b_1(A_1)$	-4.29	0.070	-3.82	0.109
	$6b_2(B_2)$	0.88	0.750	0.71	1.066
	$6b_2(A_1)$	1.36	0.760	1.09	0.999

[a]) Ref. [28], nonrelativistic results.
[b]) Absolute excitation energy given in parentheses. Positions of other lines are reported relative to the first line.

Table 3.7: Excitation energies (eV) and oscillator strengths f (a.u.) for the first core-to-valence transition from the Ti $2p$ level of $TiCl_4$ in the TDDFT approach.

		PARAGAUSS		ADF[a]	
Initial state	Final state (Term)	E^b, eV	$f \times 10^2$	E^b, eV	$f \times 10^2$
Ti $2p$ (t_2)	$10t_2 + 3e$	(456.90)	50.61	(455.99)	45.69
	$3e + 10t_2$	-2.50	1.610	-2.11	2.343
	$11t_2$	5.19	2.860	4.04	0.558
	$12t_2$	6.26	2.170	4.98	0.847
	$13t_2$	8.60	0.590	5.50	1.354
	$11a_1$	8.61	0.010	6.13	0.900
	$14t_2$	8.74	2.390	6.35	3.183
	$5e$	11.49	0.350	7.07	3.402
	$15t_2$	11.77	6.840	7.27	0.559

[a]) Ref. [29], nonrelativistic results.
[a]) Absolute excitation energy given in parentheses. Positions of other lines are reported relative to the first line.

Chapter 4

Optical spectra of Cu, Ag and Au monomers and dimers supported on MgO

Unique optical, thermodynamic, electronic, and spectral properties make metal nanoparticles useful for a variety of applications, such as optical and electronic devices, optical data storage, biosensors, magnetism, as well as catalysis [1–4]. In this context, metal nanoclusters supported on oxide surfaces and thin films as well as on inner surfaces of zeolite frameworks attract growing interest [67–70], as there is an obvious advantage of incorporating very small amounts of clusters with special chemical and physical functions into conventional materials, which in addition provide structural support for the clusters. However, the support itself may affect the electronic structure and the chemical properties of supported species [67–69, 71]. In particular, surface defects have been shown to influence in a direct and characteristic fashion the properties of adsorbed species due to typically stronger interaction with these sites than with more chemically inert regular positions [67–69, 71]. Cluster-support interaction is thus a crucial issue when rationalizing observations on such systems and using this knowledge in the design of new materials with predefined properties.

Although chemical and catalytic properties of supported metal nanoparticles comprise an area of intensive and fruitful research [67–70, 72, 73], experimental or theoretical studies on magnetic [74, 75] and optical properties [76–80] of deposited nanoparticles are far less numerous. However, this situation is changing fast due to the growing recognition of the potential for using the attractive optical properties of metal nanoclusters (in particular Au, Ag and nanoalloys thereof) in the design of materials with desired optical response for applications like tagging and anticounterfeiting (or "labeling") technology, plasmonics [5], optical communications, and optical information processing [6].

In addition to applications just mentioned, optical transitions of clusters provide signatures that can be exploited in experimental characterization techniques. Optical

spectroscopy has long been used to study metal clusters in the gas phase [3,81]. However, studies on supported clusters require the development of new characterization tools to complement those of traditional surface science, such as ultra-violet electron spectroscopy (UPS), X-ray electron spectroscopy (XPS) or electron energy loss spectroscopy (EELS), for which major challenges arise due to the low concentrations of adsorbed species (at the border of detection limit) and the dominant background signal of the support material. Only recently the very sensitive cavity ringdown spectroscopy (CRDS) was applied to surface systems and seems to emerge as a method of choice for overcoming these problems [79,80]. Theoretical investigations of absorption spectra of supported metals represent a complex task, which can be performed with sufficient accuracy with the help of the linear response TDDFT method [8,9,82]. The potential of this theoretical approach for surface systems has not yet been fully exploited; among the few published works we mention very recent contributions devoted to Cu or Au atoms and small aggregates on MgO [77,78] and atomic and dimer Au species on amorphous SiO_2 [79,80].

Recently, our group carried out a series of systematic adsorption studies [30,32–34] on coinage metal atoms and small aggregates, M_n (M = Cu, Ag, Au, n = 1 – 4), deposited at regular O^{2-} and oxygen vacancy sites F_s or F_s^+ of MgO(001). In continuation of these studies, we present here a systematic evaluation and discussion of the optical absorption spectra of supported coinage metal atoms and dimers, where we explored three key parameters: elemental composition, particle size, and interaction with the support on regular as well as defect sites. In the size range where metal particles consist of only a few atoms, the optical properties of free and supported clusters are directly linked to their intrinsic electronic and geometric properties. We will show that for such small supported species, interaction with a defect can significantly affect their electronic energy levels and optical signatures.

4.1 Computational methods and models

The optical properties of atoms M_1 (M = Cu, Au, Ag) and dimers M_2 adsorbed at O^{2-} sites of the regular MgO(001) surface as well as at F_s and F_s^+ oxygen vacancies of that surface were theoretically studied in the framework of DFT with the help of the parallel computer code PARAGAUSS [22,83]. All-electron calculations were carried out with the linear combination of Gaussian-type orbitals fitting-functions density functional (LCGTO-FF-DF) method [84]. The generalized gradient approximation (GGA) of the exchange-correlation (XC) potential suggested by Becke and Perdew (BP86) [13,14] was used for calculation of the properties of the supported metal species.

The calculations were performed at the non-relativistic level for Cu and with the scalar relativistic variant of the Douglas-Kroll-Hess approach to the Dirac-Kohn-Sham problem for Ag and Au [85,86]. Thus, the current study does not account for spin-orbit

(SO) interaction. Optical properties of free and adsorbed atoms and dimers were computed using a linear response formalism based on the time-dependent density functional theory (TDDFT) as implemented in the program PARAGAUSS [46, 47, 83]; see Chapters 2 and 3. For numerical stability, the resolution of the identity in the coupled Kohn-Sham equations [46, 47] was applied only to the Coulomb part of the response kernel while the XC contribution to the response kernel was treated by an accurate numerical integration; see Section 3.3.4.

The Gaussian-type orbital basis sets of Cu, Ag [87, 88], and Au [89], used in the structure optimization [30–32], had to be augmented by diffuse functions for an accurate evaluation of absorption properties by the linear response TDDFT method. The orbital basis set of Cu was augmented by one s exponent (0.012237 au), two p exponents (0.046199, 0.021537 au), and one d exponent (0.042600 au). The orbital basis set of Ag was augmented by two s exponents (0.041877, 0.014877 au), and two p exponents (0.032648, 0.012615 au). Similarly the orbital basis set for Au atom was augmented by one s exponent (0.004545 au) and three p exponents (0.008695, 0.003780, 0.001644 au). The exponents of the orbital basis sets for metal atoms have been augmented according to geometric progressions. Thus, in the TDDFT calculations, the orbital basis sets of the coinage metal atoms were Cu(16s13p7d → 7s5p4d), Ag(19s15p9d →8s6p5d), and Au(22s20p11d7f →9s7p6d4f). For the support, we used the same orbital basis set, Mg(15s10p1d →6s5p1d) and O(13s8p1d →6s5p1d) [84], as in earlier studies [30–34]. The generalized atomic contractions were obtained from BP86 calculations on atoms. For additional flexibility of the wave functions in the cavity of the surface defects, F_s or F_s^+ centers were represented by a "ghost" basis set of oxygen [32].

The auxiliary basis set used in the LCGTO-FF-DF method to represent the electron charge density and for treating the Hartree part of the electron-electron interactions was constructed in a standard fashion [84]. The s and p exponents of the orbital basis sets were doubled for s- and r^2-type functions of the auxiliary basis set. In addition, five "polarization" exponents of p- and d-type were added on each atom, constructed as geometric series with a factor 2.5. The exponents of the p set started at 0.1 au for Mg and O, 0.133442 au for Cu, and 0.103053 au for Ag as well as Au; the corresponding d-type series started in each case at twice these values. The resulting auxiliary basis sets were Cu(16s,13r^2,5p,5d), Ag(19s,15r^2,5p,5d), Au(22s,20r^2,5p,5d), Mg(13s,4r^2,5p,5d), O(13s,4r^2,5p,5d) [30–34]. The influence of additional auxiliary functions on the excitation spectra under scrutiny, in particular of diffuse p- and d- or higher angular momenta f- and g-functions, proved to be rather minor. A study of metal atoms and dimers in the gas phase and on selected support sites demonstrated that the use of saturated auxiliary basis sets (at least 13 exponents each of p-, d- and f-type) resulted in differences of 0.01–0.06 eV for excitation energies and 0.005–0.010 for oscillator strengths.

The spatial grids for numerical integration of XC contributions in SCF and response calculations were set up as a superposition of radial and angular grids [90]. The radial

grids comprised 102 shells for Cu, 119 shells for Ag, and 102 shells for Au, 67 shells for Mg, and 29 shells for O anion. In each shell a Lebedev angular grid accurate up to angular momentum L = 23 for the coinage metal atoms, and L = 17 for the substrate atoms was used [57].

Cluster models of the MgO substrate, described quantum mechanically (QM), were embedded in an elastic polarizable environment (EPE), represented by a force field [91, 92]. The EPE approach to cluster model embedding affords an accurate description of the relaxation of the support also for a charged defect, F_s^+. We employed the QM cluster $Mg_9O_9(Mg^{PP})_{16}$ to model adsorption of atoms of at O^{2-} sites of the regular MgO(001) surface and the QM cluster $Mg_9O_8(Mg^{PP})_{16}$ for atomic adsorption at neutral, F_s, and charged, F_s^+, oxygen vacancies [30, 31]. Here, Mg^{PP} designates pseudopotential centers Mg^{2+} without electrons [91, 92]. For dimers, we used slightly different cluster models, $Mg_{10}O_{10}(Mg^{PP})_{12}$, and $Mg_9O_8(Mg^{PP})_{12}$, respectively [32]. In all cases studied, the coinage metal atom or dimer adsorbed directly above an O atom or a corresponding oxygen vacancy. The optimized geometries were taken as determined in previous studies [30–32]. All cluster models with adsorbed atoms were calculated in C_{4v} symmetry, while cluster models for adsorbed dimers were calculated in C_s symmetry.

In the molecular orbital (MO) analysis given below, we will use a simplified terminology where we refer to a MO according to its leading (zero-order) character. In important cases, we will explicitly comment on admixtures of other orbitals. Also, we will assign electronic transitions by their dominant contribution; of course, TDDFT calculations commonly yield many, often notably smaller contributions from other symmetry-allowed combinations of states. The investigation of the electron transitions with the help of the natural transition orbitals (NTO) [93] is a matter of the future work. With the help of the NTO technique based on the corresponding orbital transformation of Amos and Hall [94] one can dramatically simplify the quantitative description of an electronic transition.

Calculated polarization-resolved optical spectra will be presented with a Gaussian broadening (σ = 0.05 eV equivalent to a full width of 0.12 eV at half height) applied to individual transitions, weighted by the corresponding calculated oscillator strengths.

4.2 Optical transitions of M_1 adsorbed at regular and defect sites of MgO

Atoms in the gas phase and at regular O^{2-} sites

Computational studies of our group [30–32, 95–97] and of others [77, 98–101] have unambiguously shown that on the regular MgO(001) surface metal atoms preferentially adsorb on top of surface oxygen anions. The nature of interaction with regular surface

sites is mainly polarization and electrostatic attraction, counteracted by Pauli repulsion; therefore, adsorption energies are moderate, 93, 46, and 96 kJ $^{-1}$, for Cu, Ag, and Au, respectively [30,31]. Distances to the oxygen center forming the adsorption site are 2.11, 2.29, and 2.30 Å, for Cu, Ag, and Au, respectively. Two TDDFT studies recently addressed optical properties of Cu [77] and Au [78] atoms and larger aggregates supported at regular O^{2-} and F_s sites of MgO(001) terraces. However, neither a theoretical nor an experimental work to date compared systematically the optical spectra of the coinage metals adsorbed at MgO. The current work attempts such a systematic evaluation. We also wanted to compare with the results of earlier TDDFT studies for Cu and Au [77,78], where different types of pseudopotential approaches were used in contrast to the present all-electron method; in Ref. [78], a plane-wave based technology [102] was employed as opposed to the present approach which relies on localized MO basis sets.

Table 4.1: Vertical transition energies (eV) and oscillator strengths (in square brackets) for coinage metal atoms in the gas phase (gp) and supported at O^{2-} sites of MgO(001).[a]

		(n-1)d→ns			ns→np			ns→(n+1)s		
		calc.		exp.[b]	calc.		exp.[b]	calc.		exp.[b]
Cu	gp	1.10 (H_g)	[0.000]	1.49	4.12 (T_{1u})	[0.154]	3.81	5.18 (A_g)	[0.000]	5.35
	O^{2-}site	2.13 (E)	[0.001]		2.45 (E)	[0.072]		3.41 (A_1)	[0.076]	
		2.20 (A_1)	[0.000]		2.86 (A_1)	[0.004]				
		2.36 (B_2)	[0.000]							
		2.39 (B_1)	[0.000]							
Au	gp	3.27 (H_g)	[0.000]	3.97	4.07 (T_{1u})	[0.234]	3.74	5.14 (A_g)	[0.000]	5.28
	O^{2-}site	2.66 - 5.44	[0.053][c]		2.62 (E)	[0.110]		3.54 (A_1)	[0.053]	
					3.22 (A_1)	[0.133]				
Ag	gp	1.36 (H_g)	[0.000]	1.74	5.23 (T_{1u})	[0.129]	4.95	6.16 (A_g)	[0.000]	6.76
	O^{2-}site	2.14 - 5.15	[0.012][c]		3.33 (E)	[0.041]		4.20 (A_1)	[0.046]	
					3.87 (A_1)	[0.038]		4.26 (A_1)	[0.049]	
								4.28 (A_1)	[0.042]	

[a]) Atoms in the gas phase were calculated in I_h symmetry, adsorbed atoms in C_{4v} symmetry. The irreducible representations given in parentheses characterize the transition dipole moment.
[b]) Ref. [103,104]. Experimental values for d→s and s→p transitions are averaged over the fine structure. For transitions between degenerate states, oscillator strengths per partner are given.
[c]) Maximum value.

To understand the nature and trends in optical transitions of adsorbed coinage metal atoms, it is informative first to look at the excitation spectra of the corresponding free species. All three congeners, Cu, Ag, Au, feature the same electronic ground state ^{2}S and electronic configuration of the valence shell, $(n-1)\mathrm{d}^{10}n\mathrm{s}^1$ (with $n = 4, 5, 6$, respectively). The low-lying excited states include ^{2}D, ^{2}P, and $(n+1)$s ^{2}S obtained by promoting a single electron: $(n-1)$d→ns, ns→np, and ns→ $(n+1)$s, respectively (Ta-

ble 4.1); of these excitations, only ns→np transitions are symmetry allowed in optical spectra. Promoting one d electron into the valence p shell results in dipole and spin forbidden transitions to high-spin states ^{4}P, ^{4}F, and ^{4}D, which for Cu and Au, extend in part below the $(n+1)$s ^{2}S level. The 5d→6p excitations of Au are strongly affected by spin-orbit interaction; for instance, the three components of ^{4}P, with a weighted average of 5.66 eV, are separated by 1.4 eV due to spin-orbit interaction [103, 104]. Table 4.1 compares calculated excitation energies for free atoms with experimental data obtained by averaging term energies over the spin-orbit structure and also with the excitation energies for supported atoms to be discussed below. The $(n-1)$d→np group of transitions is not included because for atoms supported at O^{2-} sites of MgO this series lies above the presently considered energy range up to 4.5 eV.

That energy range is already at the border of the theoretical band gap of MgO(001), 4.6 eV, as determined with the presently used GGA method, whereas the experimental gap is much larger, 7.8 eV [105]. Common local density functional and GGA methods are known to underestimate the band gap of wide-gap insulators [10]. Unfortunately, this causes some artifacts (and we will touch on that again in the further discussion), e.g., unrealistic mixing of unoccupied levels of the metal with the conduction band of the support. Hence, only the lowest transitions can be reliably and unambiguously described with the methodology used here. Our GGA estimate for the band gap of the support is close to the value, 4 eV, previously estimated with a cluster approach at the LDA level [78]. Therefore, it would not be appropriate if one tried to match blindly current TDDFT results to experimental data. Instead of expecting quantitative accuracy, we regard the current computational method as a semi-quantitative tool, which affords a coherent systematic comparison and information about the MOs involved in the various transitions. In this way, it may become useful for interpreting experimental results. Also, the method provides valuable means for assessing trends, e.g. it allows us to compare systematically the three coinage metals and to explore the extent to which the cluster geometry as well as the nature of the adsorption site affects general aspects of spectral features.

As seen from Table 4.1, for free atoms the current TDDFT approach reproduces experimental trends very well: the order and the relative energies of the transitions are adequately predicted. The maximum error in the theoretical transition energies, ~25%, is obtained for the 3d→4s transition of Cu, but the average deviation from experiment, 12%, is quite a bit smaller. We note a significantly larger separation of 4d and 5s levels in the Ag atom, ~4 eV, compared to the corresponding valence levels in Cu and Au, 1.5 and 1.7 eV, respectively. The similarity between Cu and Au comes as the consequence of a relativistic stabilization of the 6s level and simultaneous destabilization of the 5d levels of Au [106]. The same trend also occurs for bulk metals, where the 4d levels of bulk Ag were found to lie ~2 eV lower than the 3d levels of bulk Cu [107]; the 5d levels of bulk Au lie ~1 eV below the 3d levels of bulk Cu [108].

As a result of the interaction with the O^{2-} anions of the MgO surface, the *n*s level of the coinage metal atom M shifts to higher energies; this effect is a manifestation of the so-called Pauli repulsion between the filled shells. Consequently, *n*s→*n*p and *n*s→(*n* + 1)s transition energies are reduced by 1.5 – 2 eV (Table 4.1). In addition, the M *n*p levels split into p_z and $p_{x,y}$ components; the former level also shifts to a somewhat higher energy due to electrostatic destabilization by a negatively charged oxygen center.

Fig. 4.1 shows the calculated polarization-resolved absorption spectra for Cu, Ag, and Au monomers adsorbed on top of an O center of the ideal MgO(001) surface. The three main spectral features, labeled by I, II, and III, are the same for all three metals M and have mainly intra-atomic character, *n*s→*n*$p_{x,y}$, *n*s→*n*p_z, and *n*s→(*n* + 1)s, respectively. However, the unoccupied *n*p and (*n* + 1)s levels of the coinage metal M lie rather close to the upper end of the MgO band gap and mix considerably with unoccupied states of the support. For instance, the 4p_z level of Cu delocalizes particularly strongly via mixing with several unoccupied states. Consequently, it contributes to several transitions, of which the lowest most intensive ones are marked as II and III. The M *n*p_z level also mixes strongly with higher lying states of M s character. Yet for simplicity, in Table 4.1, transitions II and III are formally assigned as *n*s→*n*p_z or *n*s→(*n* + 1)s according to our convention (see Section 4.2). In contrast, the *n*s→*n*$p_{x,y}$ transitions are quite unambiguously identified, as can be seen from polarization-resolved spectra (Fig. 4.1). These transitions are of E symmetry within the C_{4v} point group and thus are "visible" in x or y polarized light.

The d→s transitions, which were symmetry forbidden for atoms, now appear with low intensity due to mixing with the states of the support, e.g., a feature at ~2.8 eV for Ag (Fig. 4.1B) and at ~2.5 eV for Au (Fig. 4.1C). The mixing of the metal d states with the top of the O 2p valence band is especially pronounced for silver. This is also consistent with observations for the free Ag atom and the bulk metal (see above), where we noted lower lying 4d levels of Ag compared to the corresponding (*n* - 1)d levels of Cu and Au. Fig. 4.2A displays the calculated density of states (DOS) of Ag adsorbed at an O^{2-} site of a defect-free MgO(001) surface, represented by the $Mg_9O_9(Mg^{PP})_{16}$ embedded cluster model; the contributions to the total DOS from d, s, and p states of the Ag atom are explicitly given. The other two coinage metals show qualitatively similar patterns. The singly occupied *n*s orbital of each of the three adsorbed monomers lies well inside the band gap of MgO, whereas the (*n* - 1)d and *n*p levels appear at the lower and upper ends of the band gap, respectively. The 6s orbital of an adsorbed Au atom is shifted by ~1 eV to lower energies compared to Ag and Cu. Hence, the three major signals of Fig. 4.1 (all originating from the *n*s level of M) are shifted to higher energies for Au_1/MgO (panel C). The unlabeled features to the far right of panels A and B can be roughly assigned to transitions of type *n*s→(*n* + 1)p and (*n* - 1)d→*n*p. However, these high-lying transitions can no longer be unambiguously described in terms of excitations within a metal atom as the corresponding final states involve no-

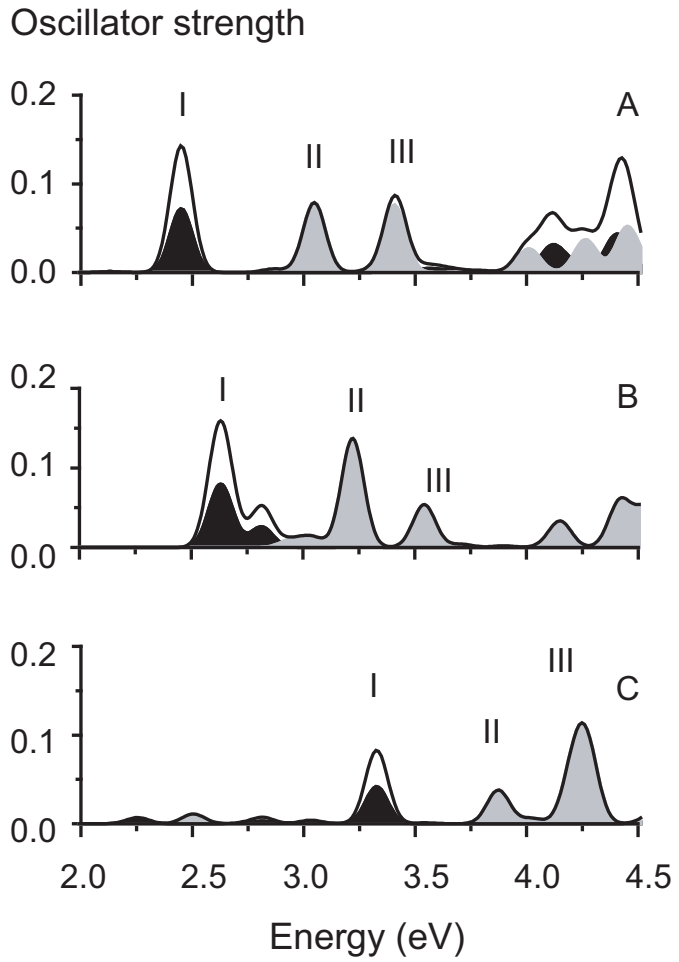

Figure 4.1: Absorption spectra of coinage metal atoms Cu (A), Ag (B), and Au (C) adsorbed at an O^{2-} site of a defect-free MgO(001) surface. Spectra are weighted by calculated oscillator strengths and broadened by a Gaussian with σ=0.05 eV. Polarization-resolved spectra are indicated by shading: gray – z-polarized transitions; black – one of two equal polarization components of xy-polarized transitions. See the text for a discussion of the major peaks marked with I, II, and III.

table admixtures of the support which likely have to be considered as artifacts of the presently used XC approximation.

Some of the present findings can be compared to the results of other recent TDDFT studies [77, 78]. In the previous study on Cu_1/MgO, only the 3d→4s and one of the 4s→4p transition energies are given [77]. That predictions with the B3LYP hybrid exchange-correlation functional [13, 109], are very close to our results: 2.29 – 2.57 eV vs. 2.13 – 2.39 eV of this work for the 3d → 4s transitions and 2.63 eV vs. 2.45 eV of this work for the lowest 4s → 4p transition (we assigned this transition to 4s →$4p_{x,y}$). An optical spectrum of Au_1/MgO was recently reported from a TDLDA calculation [78]; there, the first two strong transitions were also assigned to 6s→6p excitations, split into $p_{x,y}$ and p_z components. Given the rather different computational methodologies, the TDLDA excitation energies at 3.38 and 3.61 eV agree very well with the present results, 3.33 and 3.87 eV.

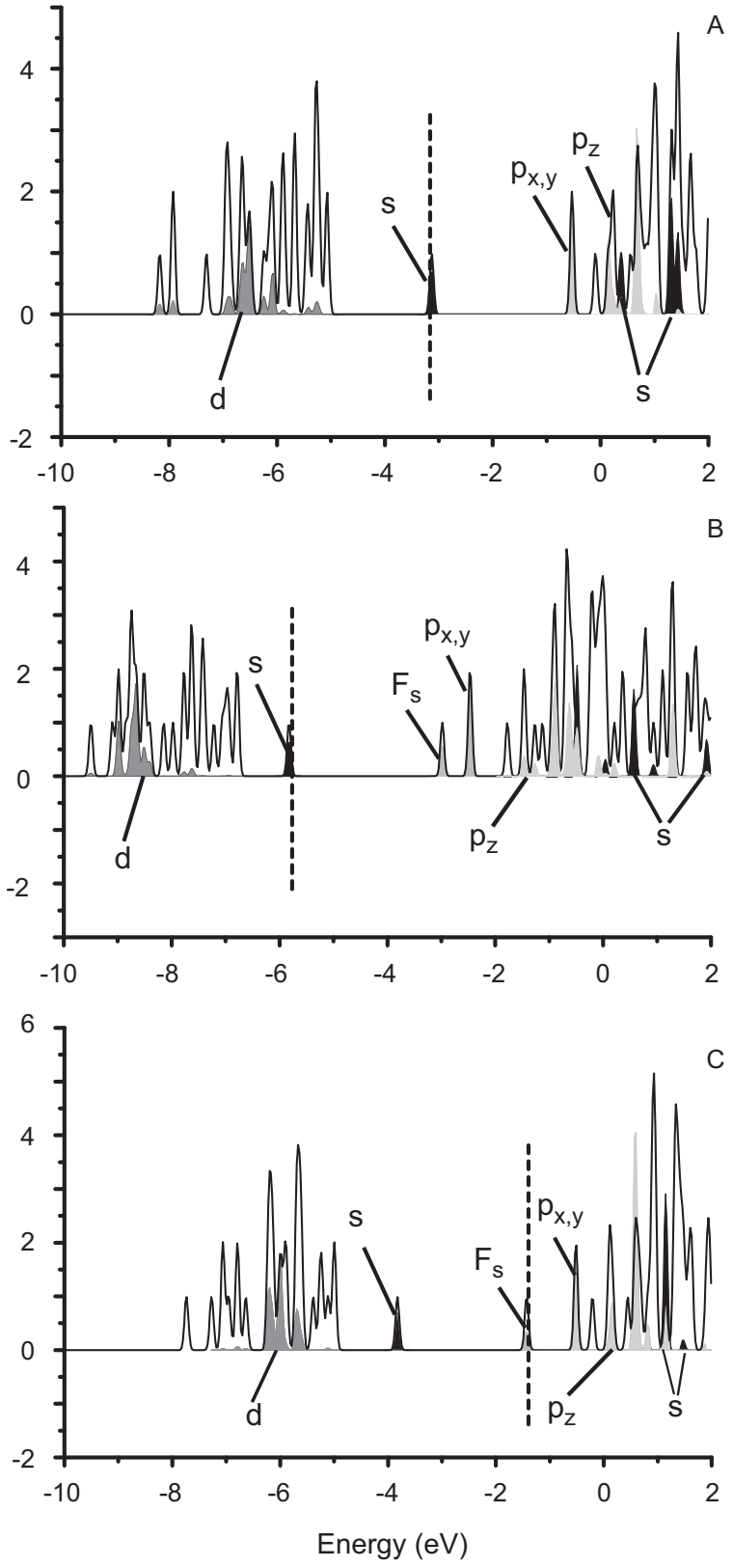

Figure 4.2: Density of states for Ag_1 adsorbed at various sites of MgO(001). (A) regular O^{2-} site; (B) F_s^+ site; (C) F_s site. A Gaussian broadening with σ=0.05 eV was applied. Contributions from Ag s, p, and d orbitals are given by black, light gray, and dark gray shading, respectively. The position of the highest occupied Kohn-Sham level is marked by a vertical dashed line.

Atoms at F_s^+ vacancy sites

"Color centers" F_s^+ or F_s are point defects on a surface that correspond to oxygen vacancies with one or two free electrons, respectively, trapped in a cavity previously occupied by a missing O atom. The bonding of M_1 to an F_s^+ center [110] can be envisaged as interaction of the singly occupied vacancy level and the ns and np$_z$ orbitals of M, particularly strongly with np$_z$; as schematically illustrated in Fig. 4.3, this is a typical example of a three-orbital interaction [111]. The ns orbital of M shifts down, whereas the F_s and np$_z$ levels shift up. Note the non-bonding character of the intermediate level, which we refer to as F_s (level); actually it carries a strong M p$_z$ contribution. The orbital labeled p$_z$ has a contribution of the original F_s cavity level. Therefore, our notations reflect the nature of these MOs only approximately. As a result of such interaction, the ns orbital of an adsorbed metal atom becomes doubly occupied and the F_s cavity level is formally empty if adsorption occurs at a charged defect, F_s^+. Favorable bonding of M_1 at an F_s^+ center is manifested by metal adsorption energies which are two to five times larger than the binding energies at regular O^{2-} sites of MgO(001) [30, 31]. Compared with binding energies of 242 and 229 kJ mol^{-1} for Cu and Ag, respectively, the Au monomer features the strongest interaction, 358 kJ $^{-1}$, which correlates with the fact that the Au 6s orbital is ~1 eV lower in energy than Cu 4s or Ag 5s in either free atoms or atoms adsorbed on regular O^{2-} sites of MgO(001), as shown by our calculations. Consequently, the stabilization due to electron transfer from the vacancy site is stronger for Au.

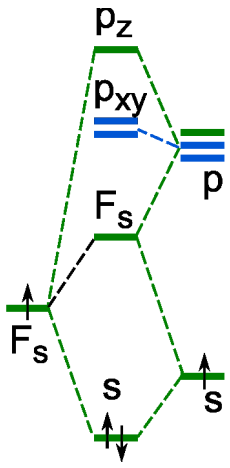

Figure 4.3: Schematic orbital energy diagram illustrating the interaction of a metal M_1 with an F_s^+ site at the MgO(001) surface.

As seen from Fig. 4.2B, the ordering of frontier orbitals slightly changes upon going from M_1/O^{2-} to M_1/F_s^+. The ns→np separation grows somewhat larger, while the F_s orbital, with a notable M np$_z$ contribution, appears below the M np$_{x,y}$ levels. Thus, at variance with the optical spectra of M_1 adsorbed at O^{2-} sites, the ns→F_s(np$_z$) transition (I in Fig. 4.4) occurs at lower energies than the ns→np$_{x,y}$ transition (II in Fig. 4.4). The next group of transitions, III, can be classified as predominantly (n - 1)d→np$_{x,y}$. Recall

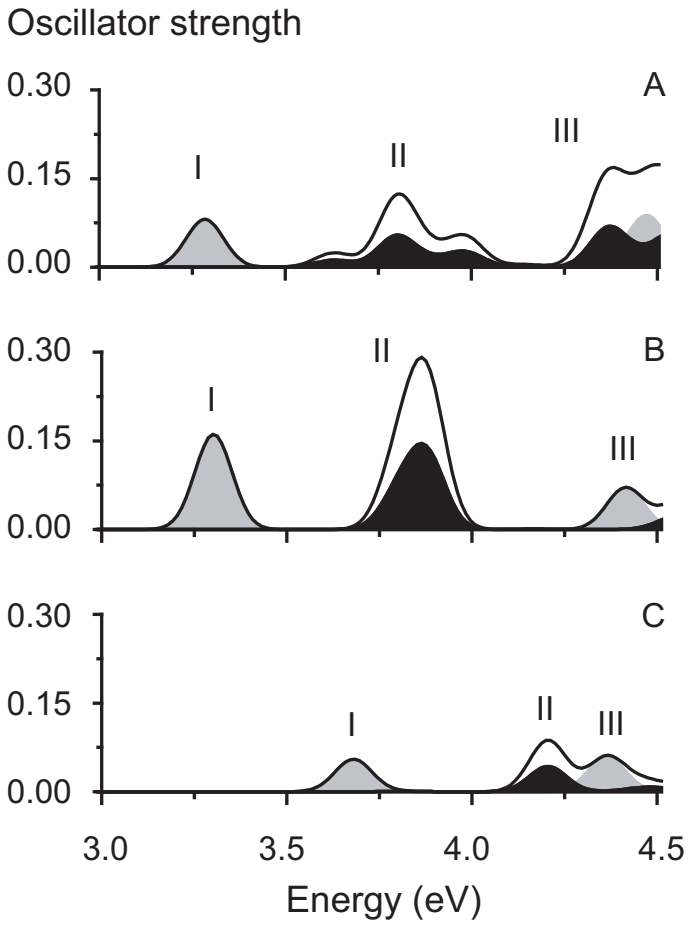

Figure 4.4: Absorption spectra of coinage metal atoms Cu (A), Ag (B), and Au (C) adsorbed at an F_s^+ site of the MgO(001) surface. Polarization-resolved spectra are indicated by shading; lay-out as in Fig. 4.1. See the text for a discussion of the major peaks marked with I, II, III.

that our model neglects spin-orbit interaction, which should shift the initial state to somewhat higher energies. Less intensive (n - 1)d$\rightarrow n$p$_z$ transitions have lower energy and overlap with ns$\rightarrow n$p$_{x,y}$ bands. For Au_1 on F_s^+, the energy separation of excitations with initial states of 5d and 6s character is really small (below 1 eV); thus, one observes in Fig. 4.4 that bands II and III, quite well separated for Cu and Ag, almost overlap for Au. Transitions of type ns$\rightarrow n$p$_z$(F$_s$) and ns$\rightarrow$(n + 1)s lie higher than 5 eV and are not discussed here.

The difference to optical spectra of M_1 adsorbed at O^{2-} sites is quite pronounced. The first strong transitions in the case of M_1/F_s^+ appear at higher energies than in the case of M_1/O^{2-}. Furthermore, a fundamental difference in the spectral pattern is most easily recognized if one compares polarization-resolved contributions to the spectra (Figs. 4.1, 4.4).

Atoms at F_s vacancy sites

The interaction of a neutral vacancy site with an adsorbed coinage metal atom follows the same scheme as described above for the case of F_s^+ and illustrated in Fig. 4.3, with the only essential difference that due to an additional electron contributed by the vacancy. Therefore, the HOMO of the ground state is the singly occupied $F_s(n\mathrm{p}_z)$ level.

Table 4.2: Calculated vertical transition energies (eV) and oscillator strengths (in square brackets) of the main low-lying excitations for coinage metal atoms supported at F_s^+ sites of MgO(001).[a]

	ns→F_s	ns→$n\mathrm{p}_{x,y}$[b]	(n - 1)d→$n\mathrm{p}_{x,y}$
Cu	3.28 (A_1) [0.081]	3.80 (E) [0.052]	3.86 - 5.59, 4.37(E) [0.066][c]
Au	3.30 (A_1) [0.161]	3.88 (E) [0.122]	4.22 - 6.64, 4.41(A_1) [0.070][c]
Ag	3.68 (A_1) [0.055]	4.21 (E) [0.043]	4.24 - 6.56, 4.36(A_1) [0.058][c]

[a]) Adsorbed atoms were calculated in C_{4v} symmetry. The irreducible representations given in parentheses characterize the transition dipole moment.
[b]) For transitions of E symmetry, oscillator strengths are given per partner.
[c]) Transition with maximum intensity.

Table 4.3: Calculated vertical transition energies (eV) and oscillator strengths (in square brackets) of the main low-lying excitations for coinage metal atoms supported at F_s sites of MgO(001).[a]

	F_s →$n\mathrm{p}_{x,y}$[b]	F_s →$n\mathrm{p}_z$	F_s →(n+1)$\mathrm{p}_{x,y}$[b]
Cu	0.72 (E) [0.007]	1.35 (A_1) [0.081]	1.78 (E) [0.033]
Au	0.86 (E) [0.009]	1.48 (A_1) [0.096]	1.81 (E) [0.016]
Ag	0.93 (E) [0.002]	1.52 (A_1) [0.056]	1.83 (E) [0.009]

[a]) Adsorbed atoms were calculated in C_{4v} symmetry. The irreducible representations given in parentheses characterize the transition dipole moment.
[b]) For transitions of E symmetry, oscillator strengths are given per partner.

Accordingly, the lowest transitions originate from the F_s level (Tables 4.2 and 4.3). Spectral features for Cu, Ag, and Au in the low-energy region are quite similar (Fig. 4.5). The low-intensity peak I corresponds to F_s→$n\mathrm{p}_{x,y}$ transitions, whereas peak II is assigned to a transition from F_s to a level exhibiting mainly MgO character. This probably is an artifact of the model as in reality the bottom of the MgO conduction band should lie much higher than predicted by our GGA-based TDDFT approach. The most intensive band III is a transition from F_s to $n\mathrm{p}_z$, followed by F_s →(n+1)$\mathrm{p}_{x,y}$ (IV) and higher lying transitions involving higher order p and s levels of M, which contain a sizable contribution from unoccupied levels of MgO. Thus, beyond that point application of our GGA-based TDDFT method is not meaningful. Overall, a notable difference to optical spectra of coinage metal atoms adsorbed at regular O^{2-} sites and F_s^+ sites is that intense peaks appear in our model at much lower energies, at 1.5 eV

or below. Polarization-resolved spectra below 2.5 eV are dominated by transitions polarized in z-direction, i.e., perpendicular to the surface plane.

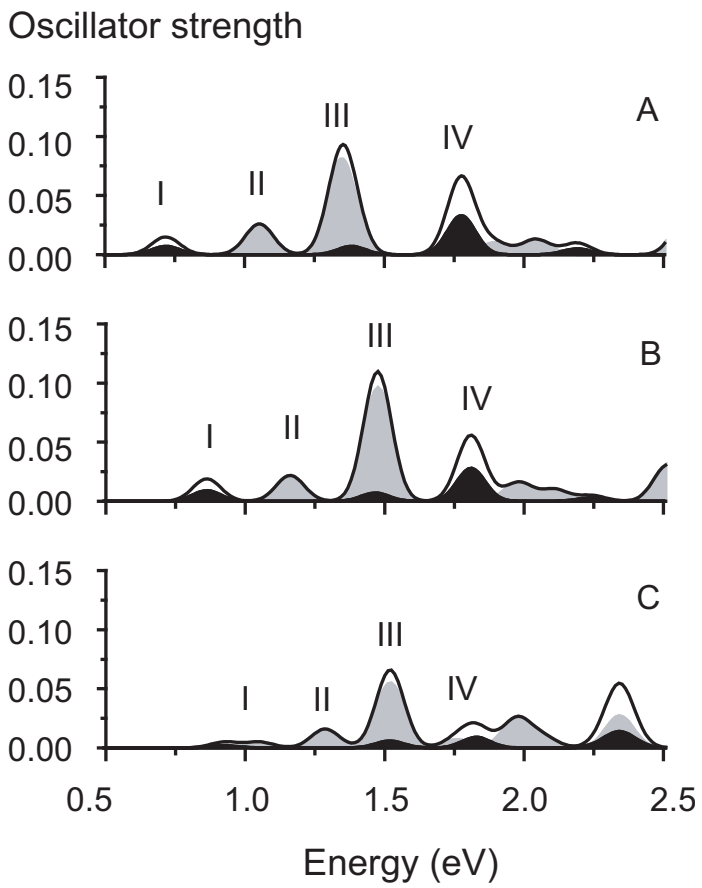

Figure 4.5: Absorption spectra of coinage metal atoms Cu (A), Ag (B), and Au (C) adsorbed at an F_s site of the MgO(001) surface. Polarization-resolved spectra are indicated by shading; lay-out as in Fig. 4.1. See the text for a discussion of the major peaks marked with I, II, III, IV.

4.3 Optical transitions of coinage metal dimers adsorbed at regular and defect sites of MgO

Dimers in the gas phase and at regular O^{2-} sites

The dimers Cu_2, Ag_2, and Au_2 in the gas phase are characterized by a singlet ground state, $^1\Sigma_g^+$ [112]. The order of the valence orbitals as obtained at our BP86 level is similar for Cu_2 and Au_2 and involves an antibonding combination of d orbitals, $d\sigma_u^*$ orbital, as HOMO (Fig. 4.6) and the antibonding combination, $s\sigma_u^*$, as LUMO. This is different from the MO ordering rendered by HF-based methods [113, 114] and the hybrid B3LYP functional [77], the HOMO is predicted to derive from a bonding combination of two s orbitals, $s\sigma_g$. Experimental spectroscopic studies on Cu_2 and Au_2 [115–119] also assumed the $(s\sigma_g^2)(s\sigma_u^{*0})$ electronic configuration because this is consistent with

$^1\Sigma_u^+(s\sigma_g \rightarrow s\sigma_u^*)$ as the first singlet excited state. Nevertheless, most recent spectroscopic studies [116–119] actually reveal that for both Cu_2 and Au_2 the two lowest excited states, A and B, of 0_u^+ symmetry are strongly spin-orbit coupled and derive from $^1\Sigma_u^+(s\sigma_g \rightarrow s\sigma_u^*)$ and $^3\Pi_u(d\pi_g \rightarrow s\sigma_u^*)$ states corroborating our expectation that valence s and d levels lie rather close and are able to mix either via spin-orbit interaction or s-d hybridization. In our calculations the energy difference between the $s\sigma_g$ and $d\sigma_u^*$ (HOMO) orbitals of Cu_2 was determined to be just 0.3 eV, i.e., much smaller than the whole span of Cu 3d orbitals, 1.63 eV. Whether or not the $d\sigma_u^*$ orbital is the correct HOMO actually does not affect the qualitative pattern of optical transitions of dimers in the gas phase as all low-lying d→s transitions have zero or vanishing intensity in our TDDFT approach, where spin-orbit coupling is not included (Table 4.4). For the same reason all singlet-triplet transitions in our calculations are spin-forbidden and have zero intensity. Our calculated values for $s\sigma_g \rightarrow s\sigma_u^*$ transitions for Cu_2 and Au_2 (2.53 and 2.76 eV) are slightly lower than the experimental X→B excitation energies, 2.69 eV for Cu_2 [117] and 3.18 eV for Au_2 [119]. (The B state has more $^1\Sigma_u^+$ character than the A state.) The X→A excitation energies, 2.53 eV for Cu_2 [115] and 1.76 eV for Au_2 [118], are lower than our theoretical values. A TDDFT calculation [77] using the hybrid B3LYP approach yielded a value 2.89 eV for the $s\sigma_g \rightarrow s\sigma_u^*$ transition in Cu_2. That study reported only the lowest d→s excitation energies, beginning at 2.53 eV, which is notably higher than our result, 1.90 eV. We attribute this difference to the use of a different XC functional, B3LYP [77], which affects the MO ordering (see above) and, in general, increases the HOMO-LUMO gap. That previous study [77] did not report transitions of d→p type.

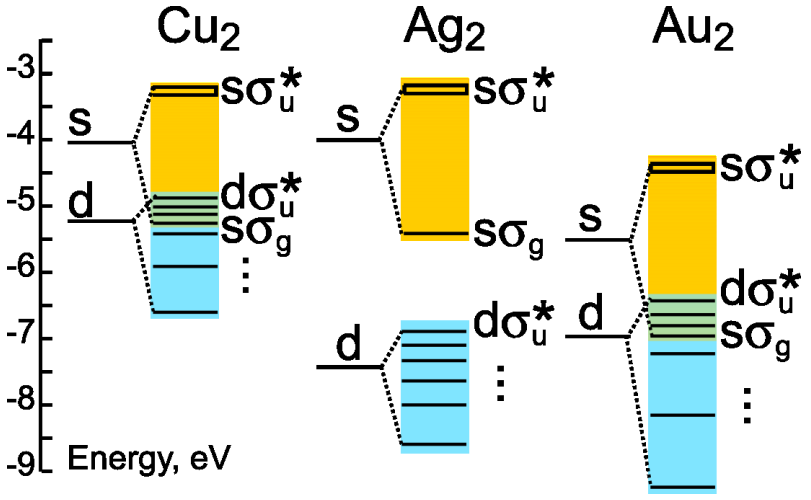

Figure 4.6: Frontier molecular orbital levels of dimers Cu_2, Ag_2, and Au_2 in the gas-phase, obtained with an all-electron BP86 calculation. The LUMO s σ_u^* is indicated by an open horizontal bar.

For Ag_2, we find the same HOMO and LUMO, $s\sigma_g$ and $s\sigma_u$, as inferred from MRD-CI ground and excited states and underlying HF MOs [120] and also supported by spectroscopic measurements [121]. This difference to Cu_2 and Au_2 is clearly a conse-

quence of the larger separation between the valence s and d levels in Ag (Fig. 4.6).

The first transition of Ag_2 with non-zero intensity is the HOMO-LUMO transition of s→s nature corresponding to $X^1\Sigma_g^+ \rightarrow^1 \Sigma_u^+(s\sigma_g \rightarrow s\sigma_u^*)$, just as calculated in the case of Cu_2 and Au_2. The experimental value for this excitation energy of Ag_2 is 2.85 eV [121], 0.2 eV lower than our result, 3.05 eV. According to the present calculations, the first d→s transition with intensity appears at 5.41 eV ($d\sigma_g \rightarrow s\sigma_u^*$). This value is very close to the adiabatic transition energy 5.55 eV determined for the corresponding $X^1\Sigma_g^+ \rightarrow 2^1\Sigma_u^+$ transition calculated with a MRD-CI method [120].

For dimers adsorbed at regular sites of MgO, the MO order does not change significantly as the interaction with the MgO surface is mainly of polarization type. From the preceding study [32], the adsorption energies of Cu_2, Ag_2, and Au_2 in the most favorable upright orientation are 132, 80, and 164 kJ mol^{-1}, respectively. The nature of HOMO and LUMO remains the same as for M_2 species in the gas phase. Thus, in dimers adsorbed at O^{2-} sites of ideal MgO(001) the lowest transitions are of the type HOMO→LUMO, i.e. $d\sigma_u^* \rightarrow s\sigma_u^*$ for Cu_2 and Au_2 (labeled I in Fig. 4.7), and $s\sigma_g \rightarrow s\sigma_u^*$ for Ag_2 (labeled II). Here, we preserved the notations used for MOs of diatomics in the gas phase, although the symmetry in the adsorbed systems has been lowered to C_s and thus previously forbidden transitions $\sigma_u^* \rightarrow \sigma_u^*$ have become allowed via interaction with the support. Furthermore, note that for Cu_2 and especially for Au_2 s-d hybridization becomes even more pronounced than in the corresponding molecules in the gas phase, which permits a certain degree of mixing between $d\sigma_u^*$ and $s\sigma_g$ MOs. For the three coinage metal diatomics under study, the calculated absorption spectra exhibit quite different spectral shape and types of transitions (Fig. 4.7).

For Cu_2, the first two peaks at 2.6 eV and 3.6 eV correspond to the transitions $d\sigma_u^* \rightarrow s\sigma_u^*$ (I) and $s\sigma_g \rightarrow s\sigma_u^*$ (II). Both transitions blue shift by ~1 eV relative to those calculated for free Cu_2 (Table 4.4). This result is at variance with findings of Del Vitto et al. [77] who reported an almost unchanged transition energy for the $s\sigma_g \rightarrow s\sigma_u^*$ excitation upon adsorption, 2.95 eV, vs 2.89 eV in the gas phase. The low-intensity feature at 4.0 eV in Fig. 4.7 is assigned as $s\sigma_g \rightarrow p\pi_u$ (III) followed by $d\sigma_u^* \rightarrow p\pi_u$ at 4.1 eV. Beyond that point the continuum of the support sets in and thus makes further identification of transitions within the metal particle difficult. As already pointed out, this much too early emergence of the continuum is a shortcoming of the XC approximation used in the present TD-DFT study.

Transitions of adsorbed Ag_2 begin at 3.1 eV with an intense $s\sigma_g \rightarrow s\sigma_u^*$ peak followed by another intense transition at 3.8 eV of $s\sigma_g \rightarrow p\pi_u$ type (III). The $s\sigma_g \rightarrow s\pi_u^*$ transition remains at about the same energy as in the gas-phase dimer (3.05 eV), consistent with the essentially unchanged HOMO-LUMO gap, ~2 eV in adsorbed Ag_2. We note the difference to Cu_2 and Au_2; in the latter species, the HOMO-LUMO gap increased by up to 1 eV upon adsorption, indicative of a favorable interaction with the MgO support. This is also reflected in 1.6 and 2 times higher adsorption energies of Cu_2 and Au_2

Table 4.4: Calculated vertical transition energies (eV) and oscillator strengths (in square brackets) for coinage metal dimers, in the gas phase (gp) and supported at O^{2-} sites of MgO(001).[a]

System		d→s[b]		s→s		d→p and s→p[c]	
		Transition	Character	Transition	Character	Transition	Character
Cu_2	gp	1.90 [0.000]	$\sigma_u^* \rightarrow \sigma_u^*$	2.53 [0.080]	$\sigma_g \rightarrow \sigma_u^*$	3.45 - 5.43	
		1.91 [0.006]	$\pi_g^* \rightarrow \sigma_u^*$			3.67 [0.016]	$d\pi_g^* \rightarrow \pi_u$
		2.07 [0.000]	$\delta_u^* \rightarrow \sigma_u^*$			4.19 [0.036]	$d\delta_g \rightarrow \pi_u$
		2.30 [0.000]	$\delta_g \rightarrow \sigma_u^*$			4.26 [0.063]	$d\sigma_u^* \rightarrow \sigma_g$
		2.81 [0.000]	$\pi_u \rightarrow \sigma_u^*$			5.32 [0.007]	$d\pi_u \rightarrow \sigma_g$
		4.79 [0.531]	$\sigma_g \rightarrow \sigma_u^*$			5.43 [0.038]	$d\sigma_g \rightarrow \pi_u$
						4.54 [0.389]	$s\sigma_g \rightarrow \pi_u$
	O^{2-}site	2.12 - 6.44		3.55 [0.094]	$\sigma_g \rightarrow \sigma_u^*$	3.99 [0.003]	$d\sigma_u^* \rightarrow \sigma_g$
		2.60 [0.045][d]	$\sigma_u^* \rightarrow \sigma_u^*$			4.09 [0.032]	$d\sigma_u^* \rightarrow \pi_u$
		4.26 [0.046][d]	$\sigma_g \rightarrow \sigma_u^*$			4.09 [0.003]	$d\sigma_u^* \rightarrow \pi_u$
						3.96 [0.033]	$s\sigma_g \rightarrow \pi_u$
						3.96 [0.012]	$s\sigma_g \rightarrow \pi_u$
Ag_2	gp	3.71 [0.000]	$\sigma_u^* \rightarrow \sigma_u^*$	3.05 [0.367]	$\sigma_g \rightarrow \sigma_u^*$	3.70 - 7.96	
		3.83 [0.004]	$\pi_g^* \rightarrow \sigma_u^*$			6.01 [0.054]	$d\pi_g^* \rightarrow \pi_u$
		4.03 [0.000]	$\delta_u^* \rightarrow \sigma_u^*$			6.43 [0.419]	$d\sigma_u^* \rightarrow \sigma_g$
		4.23 [0.000]	$\delta_g \rightarrow \sigma_u^*$			6.47 [0.218]	$d\delta_g \rightarrow \pi_u$
		4.79 [0.000]	$\pi_u \rightarrow \sigma_u^*$			7.30 [0.046]	$d\sigma_g \rightarrow \pi_u$
		5.41 [0.060]	$\sigma_g \rightarrow \sigma_u^*$			7.37 [0.050]	$d\pi_u \rightarrow \sigma_g$
						4.70 [0.754]	$s\sigma_g \rightarrow \pi_u$
	O^{2-}site	3.30 - 5.86		3.12 [0.502]	$\sigma_g \rightarrow \sigma_u^*$	4.28 [0.004]	$d\sigma_u^* \rightarrow \sigma_g$
		4.54 [0.041][d]	$\sigma_u^* \rightarrow \sigma_u^*$			3.81 [0.117]	$s\sigma_g \rightarrow \pi_u$
						3.87 [0.131]	$s\sigma_g \rightarrow \pi_u$
Au_2	gp	2.27 [0.000]	$\sigma_u^* \rightarrow \sigma_u^*$	2.76 [0.122]	$\sigma_g \rightarrow \sigma_u^*$	5.05 - 8.13	
		2.33 [0.011]	$\pi_g^* \rightarrow \sigma_u^*$			5.23 [0.003]	$d\pi_g^* \rightarrow \pi_u$
		2.40 [0.000]	$\delta_u^* \rightarrow \sigma_u^*$			5.50 [0.014]	$d\sigma_u^* \rightarrow \sigma_g$
		2.73 [0.000]	$\delta_g \rightarrow \sigma_u^*$			6.07 [0.288]	$d\delta_g \rightarrow \pi_u$
		3.84 [0.000]	$\pi_u \rightarrow \sigma_u^*$			7.71 [0.363]	$d\pi_u \rightarrow \sigma_g$
		6.35 [0.804]	$\sigma_g \rightarrow \sigma_u^*$			8.13 [0.170]	$d\sigma_g \rightarrow \pi_u$
						5.62 [0.288]	$s\sigma_g \rightarrow \pi_u$
	O^{2-}site	2.93 - 5.53		4.01 [0.006]	$\sigma_g \rightarrow \sigma_u^*$	4.91 [0.003]	$d\sigma_u^* \rightarrow \sigma_g$
		3.02 [0.052][d]	$\sigma_u^* \rightarrow \sigma_u^*$			4.17 [0.004]	$d\sigma_u^* \rightarrow \pi_u$
						4.18 [0.005]	$d\sigma_u^* \rightarrow \pi_u$

[a]) MO symmetries are given for the point group $D_{\infty h}$. For M_2 adsorbed on MgO, the same notations are used to show correspondence between the MOs of gas-phase and adsorbed molecules.
[b]) For degenerate transitions, oscillator strengths are given per partner.
[c]) Only transitions with non-zero intensity are listed; for adsorbed species, the range up to 4.5 eV is considered.
[d]) Transition with maximum intensity.

compared to Ag_2.

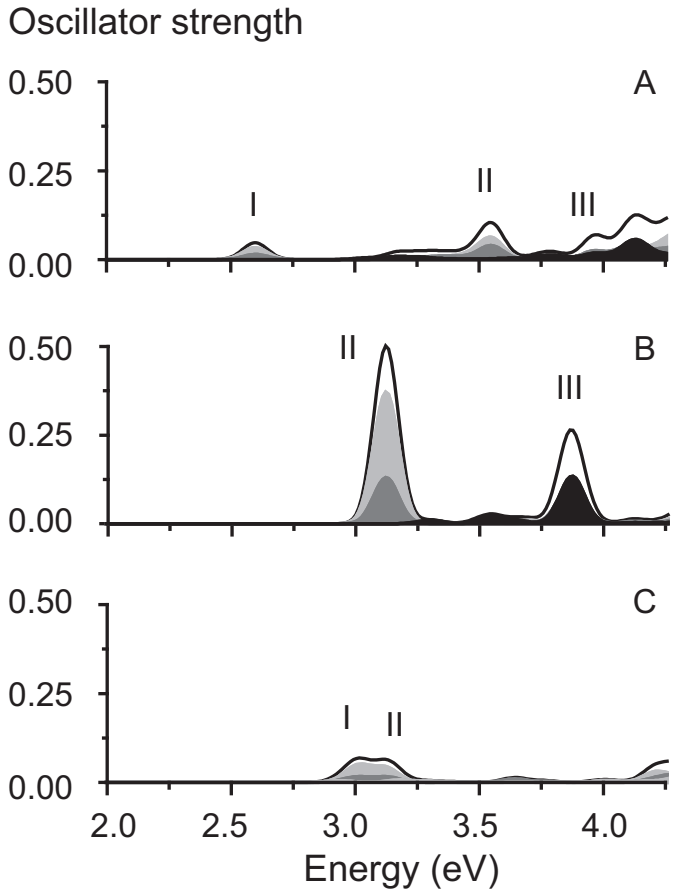

Figure 4.7: Absorption spectra of coinage metal dimers Cu_2 (A), Ag_2 (B), and Au_2 (C) adsorbed at an O^{2-} site of a defect-free MgO(001) surface. Polarization-resolved spectra are indicated by shading: dark gray – x-polarized transitions black – y-polarized transitions, light gray – z-polarized transitions. See the text for a discussion of the major peaks marked with I, II, III.

For Au_2, the first transitions with intensity appear at 3.0 eV with the weak $d\sigma_u^* \rightarrow s\sigma_u^*$ band and remain at rather low intensity in the considered energy range up to 4.25 eV (Fig. 4.7). The $d\sigma_u^* \rightarrow s\sigma_u^*$ transition lies 0.7 eV above the gas-phase value, 2.26 eV; this upward shift is of similar magnitude as determined for Cu_2 (Table 4.4).

Although quite differently looking, the three spectra can be characterized by some common features. In the energy range considered, the two main transitions are of type $d\sigma_u^* \rightarrow s\sigma_u^*$ (I) and $s\sigma_g \rightarrow s\sigma_u^*$ (II) (Fig. 4.7). The remarkably high intensity of the latter transition in the case of Ag_2 can probably be rationalized by the relatively pure $s\sigma_g$ character of the HOMO, separated by 0.8 eV from the underling d-manifold, and the weak interaction with the support, whereas for Cu_2 and Au_2, $s\sigma_g$ and $d\sigma_u^*$ mixing is quite pronounced. The former transition, of $d\sigma_u^* \rightarrow s\sigma_u^*$ type, is less intense because it is parity forbidden for dimers in the gas phase. Furthermore, the d→s transitions are dipole forbidden in the free atoms.

Inclusion of SO interaction is expected to affect the calculated spectra at least of Au_2, because of an upward spread in energy of the d-manifold and thus a decreased

HOMO-LUMO gap (by ~0.5 eV as revealed by our test calculations for the gas-phase dimer).

Dimers at F_s^+ and F_s vacancy sites

Coinage metal dimers adsorb at vacancy sites in an almost upright orientation with some degree of tilting with respect to the surface normal [32]. The bonding involves, as shown above for atoms, considerable shifts of the valence (frontier) orbitals and a change of the electronic configuration of the adsorbed metal species. To first approximation, the MO picture of bonding can be described as interaction of the singly (or doubly) occupied vacancy level F_s and the $s\sigma_u^*$ LUMO of the dimer. As a result, the bonding combination $s\sigma_u^*$+F_s is lowered in energy and the antibonding combination $s\sigma_u^*-F_s$ shifts upward, close to the (bonding) virtual MOs $p\sigma_g$ and $p\pi_u$ of M_2 while mixing considerably with $p\sigma_g$. For simplicity, in the following we will refer to the two MOs with a contribution from the cavity as $s\sigma_u^*$ and F_s instead of $s\sigma_u^*+F_s$ and $s\sigma_u^*-F_s$. Note, however, that due to interaction with the support, there are several unoccupied levels with mixed F_s and $p\sigma_g$ character; thus, our simplified labeling of virtual orbitals is just a convenience. The adsorption interaction just described stabilizes the electron from the vacancy level F_s^+ at the lowered $s\sigma_u^*$ orbital. However, there is also a destabilizing effect due to the weakening of the M-M bond, yet the former contribution seems to dominate as adsorption energies of M_2 at F_s^+ (66, 64 and 116 kJ mol^{-1}/atom for Cu_2, Ag_2, and Au_2, respectively) are equal or greater than for diatomics adsorbed at regular O^{2-} sites (66, 40 and 82 kJ mol^{-1}/atom) [32]. The strongest increase in the binding energy, for Au_2, correlates with the largest downward shift of $s\sigma_u^*$ (almost 1 eV below the corresponding MOs of Cu_2 and Ag_2).

The bonding picture at neutral vacancy sites is quite similar, only that the HOMO $s\sigma_u^*+F_s$ acquires a second electron from the vacancy site. The net stabilizing effect is even stronger on F_s than on F_s^+ as the vacancy orbital is doubly occupied. The adsorption interaction on a neutral F_s site is 60 – 70% stronger for all three dimers than on a charged defect site F_s^+ and 1.6 – 2.7 times larger than at regular O^{2-} sites [32].

The spectral features of diatomics adsorbed at vacancy sites are consistent with the orbital pattern just described. For dimers adsorbed at F_s^+ (Fig. 4.8), the first relatively strong transition is $s\sigma_u^* \rightarrow p\sigma_g$ (I), which appears at 2.61, 2.27, 3.18 eV for Cu_2, Ag_2, and Au_2, respectively (Table 4.5). The highest energy of this transition is calculated for Au_2, again consistent with the largest downward shift of $s\sigma_u^*$ and the strongest binding to the surface as mentioned above. The low-intensity peaks to the left of I (Fig. 4.8) are mainly from the higher occupied d orbitals to $s\sigma_u^*$ (and $s\sigma_g \rightarrow s\sigma_u^*$ in the case of Ag_2). For Ag_2, the next well-pronounced high-intensity peak (II) corresponds to the transition $s\sigma_u^* \rightarrow p\pi_g$. In fact, the MO to that we refer as $p\pi_g$ is its A′ component, which bears a sizable contribution from F_s and also mixes strongly with $p\sigma_g$ due to a considerable tilting of Ag_2 with respect to the surface normal, 29° [32]. Transitions

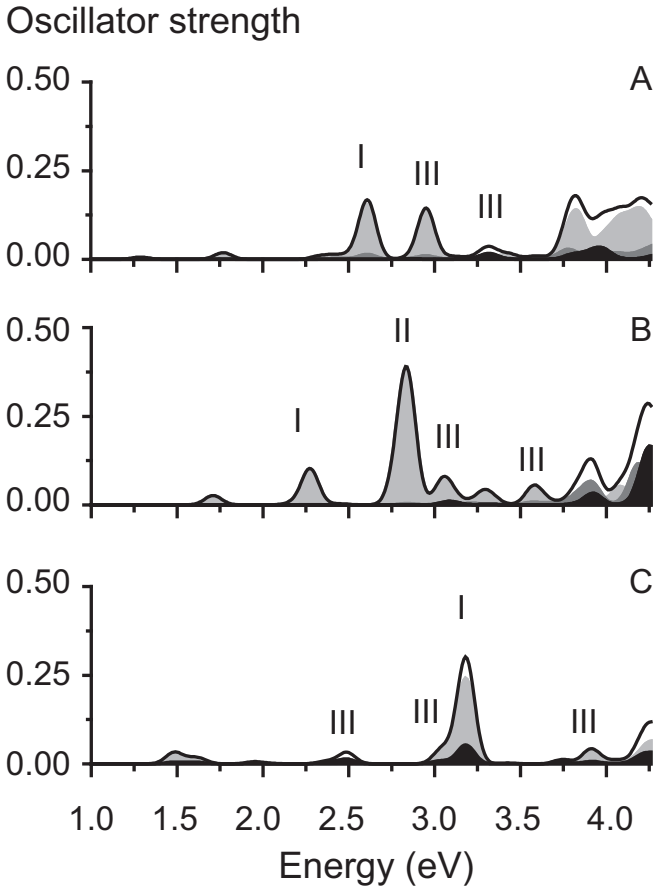

Figure 4.8: Absorption spectra of coinage metal dimers Cu_2 (A), Ag_2 (B), and Au_2 (C) adsorbed at an F_s^+ site of the MgO(001) surface. Lay-out as in Fig. 4.7. See the text for a discussion of the major peaks marked with I, II, III.

of this type are found to appear with much lower intensity for Cu_2 and Au_2 (Table 4.5). One reason for that difference could be a less significant tilting of Cu_2 and Au_2 moieties, at most 10°. However, we will see in the following that the same strong peak appears for Ag_2 (but not for Cu_2 and Au_2) at a neutral F_s defect where only a minor tilting was calculated for all three dimers. This anomalous behavior of Ag_2 may be due to its weaker interaction with the MgO surface. Thus, low-lying transitions have more pronounced intramolecular character, whereas Cu_2 and Au_2 interact stronger with the support, which results in many mixed states and a distribution of oscillator strength over a range of transitions. Transitions from $s\sigma_u^*$ to F_s carry very low intensity (Table 4.5). Only for Ag_2 is this transition at 3.3 eV calculated to be visible in the spectrum. Other well-separated peaks to the right of I (and also to the left of I in case of Au_2), marked as III in Fig. 4.8, are assigned as $d \rightarrow s\sigma_u^*$.

Absorption spectra of dimers supported at neutral vacancy sites Fs of the MgO(001) surface (Fig. 4.9, Table 4.5) can be interrelated with those for M_2 at the corresponding F_s^+ sites. As stated above, the qualitative frontier orbital picture differs only by the doubly occupied $s\sigma_u^*$ HOMO level instead of the singly occupied level of dimers adsorbed at F_s^+. In the spectra of all three coinage metal dimers, the first peaks of high

Table 4.5: Calculated vertical transition energies (eV) and oscillator strengths (in square brackets) for coinage metal dimers supported at F_s^+ and F_s sites of MgO(001).[a]

	System	$s\sigma_u^* \rightarrow p\sigma_g$	$s\sigma_u^* \rightarrow p\pi_u^b$	$s\sigma_u^* \rightarrow F_s$
Cu_2	F_s^+ site	2.61 [0.133]	3.91 [0.012]	3.36 [0.003]
			3.92 [0.011]	
	F_s site	2.17 [0.123]	2.46 [0.006]	2.54 [0.082]
			2.46 [0.009]	
Ag_2	F_s^+ site	2.27 [0.082]	2.84 [0.281]	3.29 [0.028]
			2.84 [0.000]	
	F_s site	2.08 [0.142]	2.12 [0.001]	2.48 [0.096]
			2.13 [0.001]	
Au_2	F_s^+ site	3.17 [0.220]	3.15 [0.011]	3.97 [0.002]
			3.17 [0.006]	
	F_s site	2.72 [0.122]	2.78 [0.000]	3.09 [0.099]
			2.78 [0.000]	

[a]) MO symmetries are given for the point group $D_{\infty h}$ to show the correspondence between MOs of gas-phase and adsorbed molecules.
[b]) For degenerate transitions, oscillator strengths are given per partner.

intensity (I) again correspond to the $s\sigma_u^* \rightarrow p\sigma_g$ transition. At neutral vacancy sites, these transitions are calculated 0.2 – 0.5 eV lower in energy compared to the spectra of dimers at charged defect sites F_s^+. The $s\sigma_u^* \rightarrow F_s$ transitions (II) follow with comparable intensities at 2.5, 2.4 and 3.1 eV for Cu_2, Ag_2, and Au_2, respectively. The next higher band (III) that appears in all three spectra is also of $s\sigma_u^* \rightarrow p\sigma_g$ type, but it involves a higher lying orbital of partial $p\sigma_g$ character. In the case of Ag_2, transitions II and III cannot be unambiguously separated because both are actually mixtures involving large contributions of $s\sigma_u^* \rightarrow F_s$ and $s\sigma_u^* \rightarrow p\sigma_g$. Other identifiable higher transitions (IV) are from the top of the d manifold, $d\sigma_u^* \rightarrow F_s$, found in the spectra of Cu_2 and Au_2 around 2.9 and 4.0 eV, respectively; for Ag_2 they are not observed in the considered energy range as occupied d orbitals lie quite low in energy. Instead, a $s\sigma_g \rightarrow p\sigma_g$ transition (V) with sizable intensity is found around 3.7 eV. Unmarked bands involve transitions to higher lying orbitals with considerable admixtures of MgO levels. Overall, the spectral shapes of the three congeners differ notably (Fig. 4.9). Still the transition $s\sigma_u^* \rightarrow p\sigma_g$ can be considered characteristic, ordered in energy according to $Ag_2 < Cu_2 < Au_2$; that pattern is similar to what was calculated for the coinage metal dimers adsorbed at F_s^+ (Fig. 4.8).

Optical transitions of Au_2 at F_s centers of MgO(001) have previously been studied computationally [78] using TDDFT in the LDA approximation. In that work, two almost isoenergetic minima were reported, one with the gold dimer standing "upright" and another one with the dimer tilted by 33° from the surface normal. Surprisingly, calculations yielded completely different spectral shapes for the two isomers, despite only slight difference in geometry. Although an earlier study by our group determined

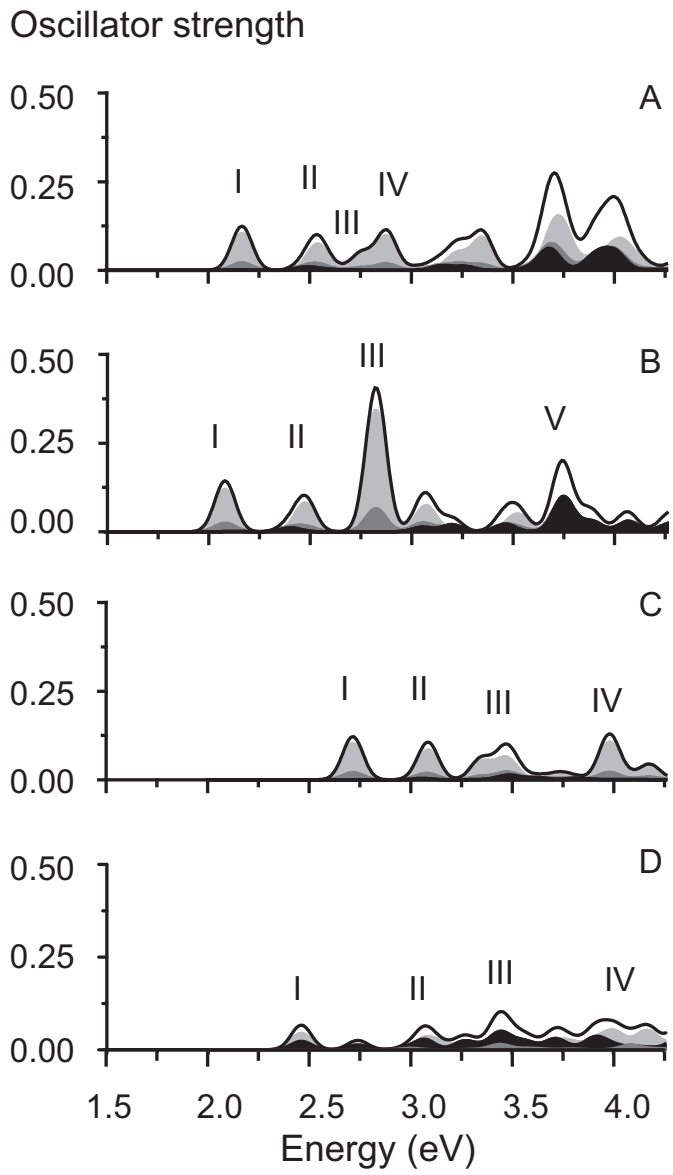

Figure 4.9: Absorption spectra of coinage metal dimers Cu_2 (A), Ag_2 (B), Au_2 in "upright" orientation (C), and Au_2 in "tilted" orientation (D), adsorbed at an F_s site of the MgO(001) surface. Lay-out as in Figure 4.7. See the text for a discussion of the major peaks marked with I to V.

only one minimum for this system (the upright geometry) [32], the remarkable similarity of our predicted spectrum (Fig. 4.9C) to that for a tilted geometry in Ref. [78] motivated us to calculate also the optical transitions for a tilted gold dimer. We used the same tilt angle as reported in Ref. [78], 33°, but kept the Au-Au distance as previously optimized with our embedded cluster model approach, at 2.63 Å. This calculation revealed only a slight shift (at most 0.3 eV) of the main bands I to IV with respect to those of the "upright" structure, although oscillator strengths decreased on the whole and migrated partially from the z to the y spectral component (following the dimer axis tilted in *y*-direction), while several previously forbidden transitions appeared with low intensity (Fig. 4.9D). The general agreement with the spectrum of the tilted isomer in Ref. [78] may seem worsened due to the appearance of several low intensity transitions; however, the positions of the main bands still agree within 0.1 – 0.2 eV. Our test showed a relatively small variation in the spectral shape upon changing the orientation of Au_2 with respect to MgO surface from an essentially upright to the titled geometry, at variance with predictions of Ref. [78]. Thus, the apparently good agreement of our spectrum for the "upright" structure (Fig. 4.9C) with the TDLDA spectrum of a tilted dimer [78] seems to be coincidental.

4.4 Effect of cluster embedding on calculated optical properties

Finally, we would like to address the importance of proper cluster embedding for accurate calculations of vertical excitation energies and oscillator strengths. To this end, we compared three cluster models, using a Cu atom supported at a regular O^{2-} site of the ideal MgO(001) surface as benchmark system. Model I is our standard EPE model, briefly described in the Section Computational Methods and in more detail elsewhere [91, 92]. In Model II, the QM cluster environment was kept untouched, but the representation of the long-range electrostatic potential was removed. In other words, the surface charge representation of the electrostatic embedding potential (SCREEP), which accounts for the electrostatic field due to the distant part of the infinite crystal, was eliminated, but a point-charge array of 644 point charges representing the electrostatic field of the nearby region of the support (region II of EPE [91, 92]) was kept. Model III comprised only the QM cluster model $CuMg_9O_9(Mg^{PP})_{16}$ without any embedding. The TDDFT results of these three models are compared in Table 4.6.

The d→s transition energies and the corresponding oscillator strengths, calculated in Model II, agree quantitatively with the benchmark values of Model I, whereas the s→p and s→s transitions are shifted by 0.3 – 0.4 eV. However, the average deviation in transition energies can be considered small (<0.3 eV) and maximum deviation obtained was 0.7 eV. The oscillator strengths deviated at most 0.06 and on average by 0.01 from those obtained with Model I. Model III underestimates the d→s transition ener-

Table 4.6: Vertical transition energies (eV) and oscillator strengths (in square brackets) for supported Cu atom at O^{2-} sites of MgO(001) with three cluster models of the support.[a]

Model[a]	(n-1)d→ns[b] calc.		ns→np[b] calc.		ns→(n+1)s calc.	
I	2.13 (E)	[0.001]	2.45 (E)	[0.072]	3.41 (A_1)	[0.076]
	2.20 (A_1)	[0.000]	2.86 (A_1)	[0.004]		
	2.36 (B_2)	[0.000]				
	2.39 (B_1)	[0.000]				
II	2.14 (E)	[0.001]	2.46 (E)	[0.063]	3.08 (A_1)	[0.043]
	2.20 (A_1)	[0.000]	2.11 (A_1)	[0.002]		
	2.36 (B_2)	[0.000]				
	2.39 (B_1)	[0.000]				
III	1.45 (E)	[0.010]	0.85 (E)	[0.049]	3.10 (A_1)	[0.036]
	1.68 (A_1)	[0.000]	0.92 (A_1)	[0.080]		
	1.69 (B_2)	[0.000]				
	1.85 (B_1)	[0.000]				

[a]) I - $Mg_9O_9(Mg^{PP})_{16}$ cluster embedded in an elastic polarizable environment (EPE);
II - same as I, i.e. with an array of 644 point charges representing the electrostatic field of the nearby region of the support, but without the surface charge representation of the long-range electrostatic embedding potential (SCREEP);
III - $Mg_9O_9(Mg^{PP})_{16}$ model without embedding.
[b]) For degenerate transitions, oscillator strengths are given per partner.

gies by 0.5 – 0.7 eV and particularly strongly the s→p transition energies, by 1.6 – 2.0 eV. Although the s→s transition energies predicted by Model III closely match those calculated with Model II, this is probably fortuitous because the average deviation of transition energies from Model I, calculated for the 30 lowest transitions, was 0.8 eV and the maximum deviation was 2.6 eV. These results illustrate the fact that Model III is too crude to be useful.

This simple test substantiates the importance of cluster embedding, which affects the ordering of the MOs and hence the excitation energies calculated with a TDDFT method. Inclusion of the SCREEP, however, overall contributes only little, in particular when one considers the overall predictive accuracy of the approach used here, but omission may affect individual transitions too much to prevent correct assignment for some systems.

Chapter 5

Summary

The objective of the present thesis was to improve and extend the functionality of the parallel density functional program package PARAGAUSS for calculating electronic excitations with methods on the basis of time-dependent density functional theory (TDDFT). The new TDDFT implementation is based on a previous separate code, which was restricted to closed-shell systems. The module, now merged with PARAGAUSS was extended to open-shell reference systems, to exploiting spatial symmetry of a molecular framework, and to feature more variants of exchange-correlation kernels. This newly developed TDDFT module of PARAGAUSS, was validated by calculating optical spectra of a variety of molecular and surface systems.

Chapter 2 presented a review of the formalism of TDDFT. Starting point was the Schrödinger equation in its time-dependent form. Next, using a superposition of monochromatic electric fields as model of an external perturbation, first-order response of the density was invoked to solve of the time-dependent Schrödinger equation, leading to the coupled perturbed Kohn–Sham (CPKS) equation. Finally, symmetry adaptation of the CPKS equation was explained.

In Chapter 3, various aspects of the implementation of TDDFT in the program PARAGAUSS were discussed. First, the resolution of the identity (RI) method for the CPKS eigenvalue problem was described for open-shell and closed-shell systems. It was shown, that applying the resolution of the identity, one can separate time- and memory-demanding four-index integrals into two-index integrals and three-index integrals with the help of auxiliary basis functions. The solution of the Casida eigenvalue problem with the help of a Davidson eigensolver as well as the parallelization of the iterative Davidson eigensolver over several processors was discussed. The symmetrization of the integrals, which are necessary for the Casida eigenvalue problem, was explained starting from the symmetrization of the orbital and auxiliary basis sets. Then the symmetrization of the four-, three- and two-index integrals was treated. The implementation of the second-order derivatives of the energy density in the local density approximation and the generalized gradients approximation to the exchange-correlation kernel was discussed in detail. The origin of numerical instabilities was analyzed. A

numerical quadrature scheme for the exchange-correlation four-index integrals and the evaluation of matrix elements of the exchange-correlation kernel as second-order derivative of the exchange-correlation functional was constructed, thus improving on the RI approach. The new numerical quadrature scheme does not require an auxiliary basis set; in turn, the results became numerically stable. However, the RI technique is still used in the TDDFT module of PARAGAUSS for evaluating the matrix elements of the Coulomb contribution to the response kernel; this part of the algorithm has never suffered from numerical instabilities.

Test calculations demonstrated the performance of the new TDDFT module of PARAGAUSS for different exchange-correlation functionals and systems of various spatial symmetry. This suite of test systems comprised the metal species Au, Au_2, and Cu_2 adsorbed at an oxygen site of the ideal MgO(001) support. The performance of the TDDFT module of PARAGAUSS was carefully analyzed by restricting the active space for core- and valence excitations with the help of energy cutoffs. The comparison of timings for 2, 4, and 8 processors for Cu_2 on MgO showed an essentially ideal scaling and a reasonable time consumption of the TDDFT module. It was shown, that the *a priory* "irrelevant" states, e.g., the core electrons for optical excitations of low energies, do not influence the results. The maximal deviation of the excitation energies between 2.0 and 5.0 eV for the test systems Au and Au_2 on MgO(001) was 0.01 eV and that of oscillator strengths was 0.005 a.u. With such a judicious restriction of the working space, calculations can be carried out in half the time.

Not only valence excitations, but also electronic transitions from core orbitals to the LUMO and other low-lying unoccupied levels were analyzed. The results obtained with PARAGAUSS were compared with those of other authors [28, 29] and fair agreement was noted. Deviations for the molecule SO_2 with excitation energies of 170–2450 eV were 0.1–0.6 eV in excitation energies and 0.03–0.04 a.u. in oscillator strengths. Deviations for the molecule $TiCl_4$ with excitations from Ti $2p$ orbitals in the range 450–470 eV were 0.4–3.0 eV for excitation energies and 0.002–0.022 a.u. for oscillator strengths. Different algorithms used in this work and other implementations [28,29] likely are the main reason for these discrepancies.

Chapter 4 reported a systematic study on the absorption spectra of coinage metal atoms Cu, Ag, and Au and the diatomics Cu_2, Ag_2, and Au_2, all systems being supported on MgO(001) terraces, at regular O^{2-} sites as well as neutral and charged oxygen vacancies (F_s and F_s^+). The adsorption complexes were described with an accurate all-electron DF method in combination with cluster embedding in an elastic polarizable environment. The energies and oscillator strengths of vertical electronic transitions were calculated within the framework of linear response TDDFT using the BP86 exchange-correlation potential and all-electron basis sets. The calculated adsorption spectra for excitation energies up to 4.5 eV for the three coinage metals show in general similar characters of the transitions, although they differ energetically and by rela-

tive intensities. Particularly for adsorbed Au atoms and dimers, the lowest transitions with intensity are typically blue-shifted with respect to the spectra of the corresponding species of the other two metals. Comparison with electronic spectra of the metal species in the gas phase revealed how the interaction of the metal species with the support affect optical properties. It was found that the interaction with MgO support significantly perturbs the atomic or molecular orbitals; therefore, transition energies for the adsorbed species are shifted by up to 2.5 eV compared to the gas-phase reference. Trends among various metal species and the importance of embedding for an accurate prediction of excitation energies of adsorbed systems were carefully analyzed. The average deviation between the results with and without embedding was 0.8 eV and the maximum deviation was 2.6 eV for excitations with energies of up to 4.5 eV. This comparison between the results with embedding and without embedding demonstrated the importance of cluster embedding in an elastic polarizable environment for ionic substrate cluster models.

Spin-orbit interaction was not included in the treatment of the systems involving Ag and Au atoms. A TDDFT method that accounts for spin-orbit interaction seems advantageous and promising for exploring excitation properties of these systems with heavy elements.

Appendix A

Response density and response function

The first-order density response $\rho^{(1)}(\boldsymbol{r},\omega)$ of the system of non-interacting electrons is obtained by inserting the Slater determinants into the perturbation expression, see Section 2.4. A simpler approach is to apply time-dependent perturbation theory directly at the level of the one-electron orbitals $\varphi_{n\sigma}(\boldsymbol{r})$. All many-electron operators in Section 2.2 need to be exchanged with the corresponding one-electron operators, and a sum over occupied one-electron wave functions $\varphi_{a\sigma}$ is used instead of the summation over many electron states Ψ_q

$$\begin{aligned}
\rho^{(1)}(\boldsymbol{r},\omega) &= \sum_{\sigma}^{\text{spin}} \sum_{a}^{\text{occ}} \sum_{s}^{\text{unocc}} \left(\frac{\rho_{as\sigma}(\boldsymbol{r}) v_{sa\sigma}(\omega)}{\Delta_{sa\sigma} + \omega} + \frac{\rho_{sa\sigma}(\boldsymbol{r}) v_{as\sigma}(\omega)}{\Delta_{sa\sigma} - \omega} \right) \\
&= \sum_{\sigma}^{\text{spin}} \sum_{a}^{\text{occ}} \sum_{s}^{\text{unocc}} \left(\frac{\rho_{as\sigma}(\boldsymbol{r}) v_{sa\sigma}(\omega)(\Delta_{sa\sigma} - \omega + \Delta_{sa\sigma} + \omega)}{\Delta_{sa\sigma}^2 - \omega^2} \right) \\
&= 2 \sum_{\sigma}^{\text{spin}} \sum_{a}^{\text{occ}} \sum_{s}^{\text{unocc}} \left(\frac{\Delta_{sa\sigma} \rho_{as\sigma}(\boldsymbol{r}) v_{sa\sigma}(\omega)}{\Delta_{sa\sigma}^2 - \omega^2} \right)
\end{aligned} \tag{A.1}$$

Here we use the following equations $\rho_{as\sigma} = \rho_{sa\sigma}$ and $v_{as\sigma} = v_{sa\sigma}$. The matrix of the electric perturbation $v_{as\sigma}$ is given in form

$$v_{as\sigma}(\omega) = \langle \varphi_{a\sigma} | v(\boldsymbol{r},\omega) | \varphi_{s\sigma} \rangle = -\int dr\, \varphi^*_{a\sigma}(\boldsymbol{r})\, v(\boldsymbol{r},\omega)\, \varphi_{s\sigma}(\boldsymbol{r}). \tag{A.2}$$

and $\Delta_{sa\sigma} = \epsilon_{s\sigma} - \epsilon_{a\sigma}$ is the difference of one-electron Kohn–Sham energies of occupied levels $\epsilon_{a\sigma}$ and unoccupied levels $\epsilon_{s\sigma}$. Thus the first-order density response, Eq. (A.1), can be written as

$$\rho^{(1)}(\boldsymbol{r},\omega) = \int d^3\boldsymbol{r}' \chi_s^{(1)}(\boldsymbol{r},\boldsymbol{r}',\omega) v(\boldsymbol{r},\omega) \tag{A.3}$$

where the integral kernel is the first-order density response function of a system of N_e non-interacting particles:

$$\chi^{(1)}_{s\sigma}(\boldsymbol{r},\boldsymbol{r}',\omega) = \sum_{\sigma}^{\text{spin}} \sum_{a}^{\text{occ}} \sum_{s}^{\text{unocc}} \frac{2\Delta_{sa\sigma}}{\Delta^2_{sa\sigma} - \omega^2} \varphi_{a\sigma}(\boldsymbol{r})\varphi_{s\sigma}(\boldsymbol{r})\varphi_{a\sigma}(\boldsymbol{r}')\varphi_{s\sigma}(\boldsymbol{r}'). \tag{A.4}$$

Appendix B

Example: point group C_{3v}

Table B.1: Characters of point group C_{3v}

C_{3v}	E	$2C_3$	$3\sigma_v$
a_1	1	1	1
a_2	1	1	-1
e	2	-1	0

Table B.2: Direct product of irreducible representations (irrep) for point group C_{3v}

$\oplus$	a_1	a_2	e
a_1	a_1	a_2	e
a_2	a_2	a_1	e
e	e	e	$a_1 + a_2 + e$

Table B.3: Selection rules for the two-index Coulomb overlap integrals in symmetry C_{3v}. Irreps of rows and columns denote the irrep of fitting functions k and k', respectively. The combinations allowed by symmetry are labelled by crosses

$(k\|\|k')$	a_1	a_2	e
a_1	$\times$		
a_2		$\times$	
e			$\times$

Table B.4: Selection rules for three-index Coulomb integrals $(ij||k)$ in symmetry C_{3v}. Labels of the columns denote the irrep of fitting function k. The direct product of the irreps of orbital basis functions i and j must be reducible to the irrep of the fitting function in order for the integral to be non-zero. The combinations allowed by symmetry are labelled by crosses.

$(ij\|\|k)$	a_1	a_2	e
$a_1 \oplus a_1 \rightarrow a_1$	$\times$		
$a_2 \oplus a_2 \rightarrow a_1$	$\times$		
$e \oplus e \rightarrow a_1$	$\times$		
$a_1 \oplus a_2 \rightarrow a_2$		$\times$	
$e \oplus e \rightarrow a_2$		$\times$	
$a_1 \oplus e \rightarrow e$			$\times$
$a_2 \oplus e \rightarrow e$			$\times$
$e \oplus e \rightarrow e$			$\times$

Table B.5: Selection rules for the four-index integrals $(ij||kl)$ in symmetry C_{3v}. The direct products of irreps of each pair orbital functions (ij) and (kl) must be reducible to the same irrep in order for the integral to be non-zero. The combinations allowed by symmetry are labelled by crosses.

$(ij\|\|kl)$	$a_1 \oplus a_1 \rightarrow a_1$ $a_2 \oplus a_2 \rightarrow a_1$ $e \oplus e \rightarrow a_1$	$a_1 \oplus a_2 \rightarrow a_2$ $e \oplus e \rightarrow a_2$	$a_1 \oplus e \rightarrow e$ $a_2 \oplus e \rightarrow e$ $e \oplus e \rightarrow e$
$a_1 \oplus a_1 \rightarrow a_1$ $a_2 \oplus a_2 \rightarrow a_1$ $e \oplus e \rightarrow a_1$	$\times$ $\times$ $\times$		
$a_1 \oplus a_2 \rightarrow a_2$ $e \oplus e \rightarrow a_2$		$\times$ $\times$	
$a_1 \oplus e \rightarrow e$ $a_2 \oplus e \rightarrow e$ $e \oplus e \rightarrow e$			$\times$ $\times$ $\times$

Appendix C

From open shell to closed shell

In this appendix we will derive the Casida equation for closed-shell systems, from the more general equation for open-shell systems, Eq. (3.1). In the following algebra, we will use the diagonal matrices with the elements defined by energy differences

$$\begin{aligned}(\Delta_\uparrow)_{pp'} &= (\epsilon_{s\uparrow} - \epsilon_{a\uparrow})\delta_{pp'} \\ (\Delta_\downarrow)_{pp'} &= (\epsilon_{s\downarrow} - \epsilon_{a\downarrow})\delta_{pp'}\end{aligned} \tag{C.1}$$

and the full matrices with matrix elements defined by

$$\begin{aligned}(A_{\uparrow\uparrow})_{pp'} &= 2\sqrt{\Delta_{p\uparrow}}K_{p\uparrow,p'\uparrow}\sqrt{\Delta_{p'\uparrow}} \\ (A_{\downarrow\downarrow})_{pp'} &= 2\sqrt{\Delta_{p\downarrow}}K_{p\downarrow,p'\downarrow}\sqrt{\Delta_{p'\downarrow}} \\ (A_{\uparrow\downarrow})_{pp'} &= 2\sqrt{\Delta_{p\uparrow}}K_{p\uparrow,p'\downarrow}\sqrt{\Delta_{p'\downarrow}} \\ (A_{\downarrow\uparrow})_{pp'} &= 2\sqrt{\Delta_{p\downarrow}}K_{p\downarrow,p'\uparrow}\sqrt{\Delta_{p'\uparrow}}\end{aligned} \tag{C.2}$$

We use a meta index p for the pairs of occupied and virtual orbitals a and s. Using the new notations, Eqs. (C.1) and (C.2), the Casida eigenvalue problem, Eq. (3.1), may be rewritten in a form that emphasizes the block structure of the equation:

$$\left[\begin{pmatrix} \Delta_\uparrow^2 & 0 \\ 0 & \Delta_\downarrow^2 \end{pmatrix} + \begin{pmatrix} A_{\uparrow\uparrow} & A_{\uparrow\downarrow} \\ A_{\downarrow\uparrow} & A_{\downarrow\downarrow} \end{pmatrix}\right] \begin{pmatrix} y_\uparrow \\ y_\downarrow \end{pmatrix} = \omega^2 \begin{pmatrix} y_\uparrow \\ y_\downarrow \end{pmatrix} \tag{C.3}$$

Here we also introduced the vectors $y_\uparrow$ and $y_\downarrow$ for corresponding ranges of the solution vector. Let us make a variable substitution:

$$\begin{pmatrix} y_\uparrow \\ y_\downarrow \end{pmatrix} = V \begin{pmatrix} u \\ v \end{pmatrix}, \tag{C.4}$$

where the matrix

$$V = \frac{1}{\sqrt{2}} \begin{pmatrix} 1 & 1 \\ 1 & -1 \end{pmatrix} \tag{C.5}$$

is unitary. By applying the basis transformation to Eq. (C.3) we obtain the eigenvalue equation for u and v:

$$V^{\dagger} \left[\begin{pmatrix} \Delta_{\uparrow}^2 & 0 \\ 0 & \Delta_{\downarrow}^2 \end{pmatrix} + \begin{pmatrix} A_{\uparrow\uparrow} & A_{\uparrow\downarrow} \\ A_{\downarrow\uparrow} & A_{\downarrow\downarrow} \end{pmatrix} \right] V \begin{pmatrix} u \\ v \end{pmatrix} = \omega^2 \begin{pmatrix} u \\ v \end{pmatrix} \tag{C.6}$$

Upon transformation the diagonal term of the original matrix acquires off-diagonal elements:

$$V^{\dagger} \begin{bmatrix} \Delta_{\uparrow}^2 & 0 \\ 0 & \Delta_{\downarrow}^2 \end{bmatrix} V = \frac{1}{2} \begin{bmatrix} \Delta_{\uparrow}^2 + \Delta_{\downarrow}^2 & \Delta_{\uparrow}^2 - \Delta_{\downarrow}^2 \\ \Delta_{\downarrow}^2 - \Delta_{\uparrow}^2 & \Delta_{\downarrow}^2 + \Delta_{\uparrow}^2 \end{bmatrix} \tag{C.7}$$

The blocks of the second term of the original matrix will be rearranged after transformation:

$$V^{\dagger} \begin{pmatrix} A_{\uparrow\uparrow} & A_{\uparrow\downarrow} \\ A_{\downarrow\uparrow} & A_{\downarrow\downarrow} \end{pmatrix} V = \frac{1}{2} \begin{pmatrix} (A_{\uparrow\uparrow} + A_{\downarrow\downarrow}) + (A_{\uparrow\downarrow} + A_{\downarrow\uparrow}) & (A_{\uparrow\uparrow} + A_{\downarrow\downarrow}) - (A_{\downarrow\uparrow} - A_{\uparrow\downarrow}) \\ (A_{\uparrow\uparrow} - A_{\downarrow\downarrow}) + (A_{\downarrow\uparrow} - A_{\uparrow\downarrow}) & (A_{\uparrow\uparrow} - A_{\downarrow\downarrow}) - (A_{\downarrow\uparrow} + A_{\uparrow\downarrow}) \end{pmatrix} \tag{C.8}$$

In a closed-shell system, the occupied and unoccupied spin-up and spin-down molecular KS orbitals have the same shape: $\varphi_{a\uparrow} = \varphi_{a\downarrow}$, as well as $\varphi_{s\uparrow} = \varphi_{s\downarrow}$ and $\Delta_{\uparrow}^2 = \Delta_{\downarrow}^2 = \Delta^2$. Spin-up and spin-down densities, therefore, are also equal: $\rho_{\uparrow} = \rho_{\downarrow} = \rho/2$. Thus, the Coulomb-exchange-correlation kernel must satisfy the equalities $K_{p\uparrow,p'\uparrow} = K_{p\downarrow,p'\downarrow}$, and $K_{p\uparrow,p'\downarrow} = K_{p\downarrow,p'\uparrow}$. By introducing $A = A_{\uparrow\uparrow} = A_{\downarrow\downarrow}$, and $B = A_{\uparrow\downarrow} = A_{\downarrow\uparrow}$, we can bring the Casida equation, Eq. (C.3), into completely decoupled form:

$$\left\{ \begin{pmatrix} \Delta^2 & 0 \\ 0 & \Delta^2 \end{pmatrix} + \begin{pmatrix} (A+B) & 0 \\ 0 & (A-B) \end{pmatrix} \right\} \begin{pmatrix} u \\ v \end{pmatrix} = \omega^2 \begin{pmatrix} u \\ v \end{pmatrix} \tag{C.9}$$

The equation for the so-called singlet-singlet transitions u is derived from the first row of Eq. (C.9):

$$\Big(\Delta^2 + (A+B)u \Big) = \omega^2 u, \tag{C.10}$$

and the equation for the so-called singlet-triplet transitions v is derived from the second row of Eq. (C.9):

$$\Big(\Delta^2 + (A-B)v \Big) = \omega^2 v. \tag{C.11}$$

Appendix D

Exchange-correlation kernel

In this section we will express the second-order derivatives of the exchange-correlation potential response kernel, Eq. (3.48), in terms of derivatives with respect to $\gamma_{\sigma\sigma'} = (\boldsymbol{\nabla}\rho_\sigma \boldsymbol{\nabla}\rho_{\sigma'})$, see Sec. 3.4. In the open-shell case we have the following expressions for the exchange-correlation potential response kernel $f_{\mathrm{XC}}^{\sigma\sigma'}$ in terms of $\boldsymbol{\nabla}\rho_\sigma$,:

$$f_{\mathrm{XC}}^{\sigma\sigma'} = \left(\frac{\partial^2}{\partial\rho_\sigma \partial\rho_{\sigma'}} - \boldsymbol{\nabla}\frac{\partial^2}{\partial\rho_\sigma \partial\boldsymbol{\nabla}\rho_{\sigma'}} + \nabla_i\nabla_j \frac{\partial^2}{\partial\nabla_i\rho_\sigma \partial\nabla_j\rho_{\sigma'}} \right) \epsilon_{\mathrm{XC}} \tag{D.1}$$

where summation over repeated Cartesian indices i and j is assumed. To replace the derivatives with respect to $\boldsymbol{\nabla}\rho_\sigma$ by derivatives with respect to $\gamma_{\sigma\sigma'}$, we will use the following formulae for the first-order derivatives:

$$\frac{\partial}{\partial\boldsymbol{\nabla}\rho_\sigma} = \sum_\tau \boldsymbol{\nabla}\rho_\tau \left(\frac{\partial}{\partial\gamma_{\sigma\tau}} + \frac{\partial}{\partial\gamma_{\tau\sigma}} \right) \tag{D.2}$$

Similarly, the second-order derivatives with respect to Cartesian components of the density gradient $\boldsymbol{\nabla}\rho$ are given by the following expression:

$$\begin{aligned} \frac{\partial^2}{\partial\nabla_i\rho_\sigma \partial\nabla_j\rho_{\sigma'}} &= \delta_{ij} \left(\frac{\partial}{\partial\gamma_{\sigma'\sigma}} + \frac{\partial}{\partial\gamma_{\sigma\sigma'}} \right) \\ &+ \sum_{\tau\tau'} \nabla_i\rho_\tau \nabla_j\rho_{\tau'} \\ &\times \left(\frac{\partial^2}{\partial\gamma_{\sigma\tau}\partial\gamma_{\sigma'\tau'}} + \frac{\partial^2}{\partial\gamma_{\tau\sigma}\partial\gamma_{\sigma'\tau'}} + \frac{\partial^2}{\partial\gamma_{\sigma\tau}\partial\gamma_{\tau'\sigma'}} + \frac{\partial^2}{\partial\gamma_{\tau\sigma}\partial\gamma_{\tau'\sigma'}} \right) \end{aligned} \tag{D.3}$$

Appendix E

Balance between orbital and auxiliary basis sets

The equation for the exchange energy density of the X_α exchange functional, when $\alpha = 2/3$, [20, 60–62] is

$$\epsilon_{X_\alpha} = -\frac{3}{4}\left(\frac{3}{\pi}\right)^{1/3}\rho^{4/3}. \tag{E.1}$$

The potential response kernel is the second-order derivative of the LDA exchange energy density ϵ_{X_α}:

$$f_{X_\alpha} = -\frac{1}{3}\left(\frac{3}{\pi}\right)^{1/3}\rho^{-2/3}. \tag{E.2}$$

The electron density in the case of a Slater-type orbital basis sets is of the general atomic form

$$\rho \;=\; e^{-\zeta r}, \tag{E.3}$$

and in the case of a Gaussian-type orbital basis sets is of the atomic form

$$\rho = e^{-\gamma r^2}. \tag{E.4}$$

Substituting Eq. (E.3) into Eq. (E.2), we obtain:

$$C_1 \int r^2 dr e^{-\alpha r^2} e^{\frac{2}{3}\zeta r} e^{-\beta r^2} = C_1 \int r^2 dr e^{-(\alpha+\beta)r^2 + \frac{2}{3}\zeta r}. \tag{E.5}$$

This integral is well defined, because $|-(\alpha+\beta)r^2| > |2\zeta r/3|$ for $r \to \infty$.

In the case of Gaussian-type functions, we substitute Eq. (E.4) into Eq. (E.2), and obtain:

$$C_1 \int r^2 dr e^{-\alpha r^2} e^{\frac{2}{3}\gamma r^2} e^{-\beta r^2} = C_1 \int r^2 e^{-(\alpha+\beta)r^2 + \frac{2}{3}\gamma r^2}. \tag{E.6}$$

This integral converges if $\gamma < 3(\alpha+\beta)/2$. Therefore there should be a balance between

fitting basis sets (α, β) of the auxiliary basis set and the exponents (γ) of the orbital basis set. To avoid this restriction we decided to implement an accurate numerical quadrature of the exchange-correlation kernel on a grid, see Sec. 3.3.4.

Appendix F

Flowchart of the TDDFT module of PARAGAUSS

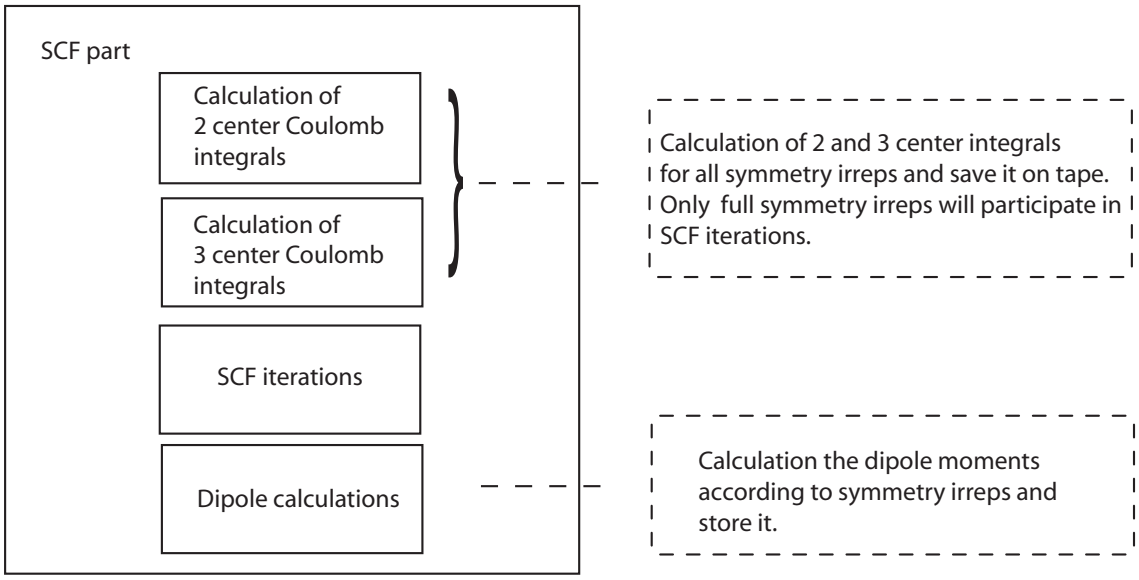

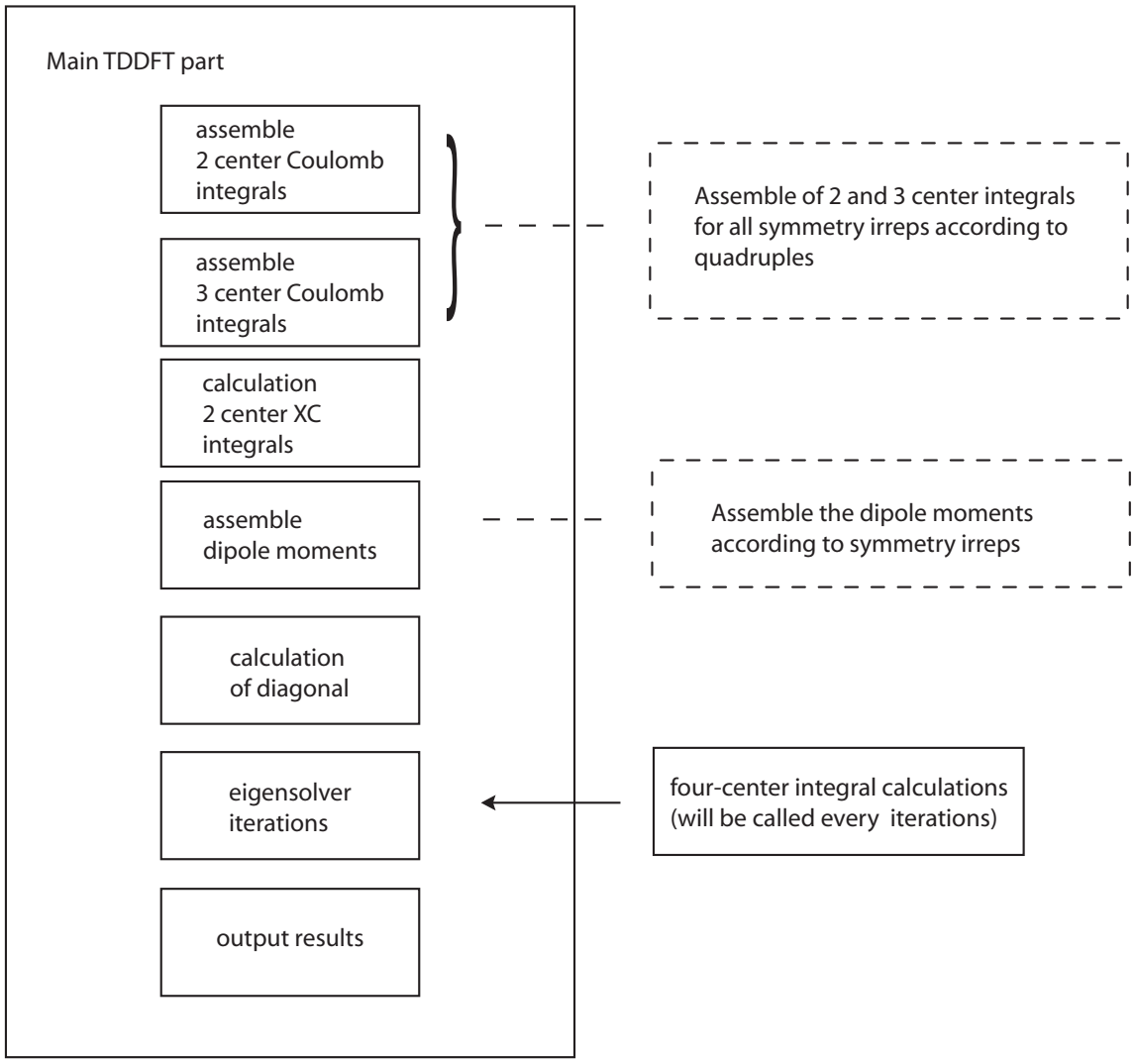
Main TDDFT part
assemble 2 center Coulomb integrals
assemble 3 center Coulomb integrals
calculation 2 center XC integrals
assemble dipole moments
calculation of diagonal
eigensolver iterations
output results
Assemble of 2 and 3 center integrals for all symmetry irreps according to quadruples
Assemble the dipole moments according to symmetry irreps
four-center integral calculations (will be called every iterations)

Appendix G

Usaging the TDDFT module of PARAGAUSS

Overview

The response formalism of the time dependent density functional theory (TDDFT), which is now a part of the PARAGAUSS [22] code, allows to calculate:

- closed-shell case: vertical singlet - singlet (S→S) and singlet - triplet (S→T) electron excitation energy,
- open-shell case: vertical excitation energy for the different electronic transitions,
- oscillator strengths.

After the calculation of the ground state of the system, the so-called "integrals" part of the calculation, PARAGAUSS [22] starts the TDDFT part, which is a parallel code for calculating excitation energies of large systems using an iterative Davidson-type eigensolver [48, 49, 51]. Optionally, the oscillator strengths can be calculated as well. In this appendix we will discuss typical strategies and suggestions for TDDFT calculations. Also we will explain in detail, how to use TDDFT on such a system as H_2O, Au, Au_2. Then we will try to answer some important questions concerning TDDFT calculations, convergency problems and the fitting basis set. We will explain all the command lines of the RESPONSE part of the input file of PARAGAUSS.

Typical strategies for using TDDFT in PARAGAUSS

With the new version of PARAGAUSS it is no more required to calculate the integrals separately after the ground state calculations. PARAGAUSS will start the TDDFT subroutines automatically (of course if one intends to calculate with TDDFT). The TDDFT part will calculate the desired response properties.

A typical calculation of the vertical excitation energies would proceed like this:
Standard PARAGAUSS preparation:

- choosing the appropriate symmetry for the system
- optimization of the geometry (optional, one could use the experimental one)
- choosing an appropriate exchange-correlation functional
- for the open-shell there is no need to specify the type of the transitions

TDDFT specification:

- for a closed-shell system one should decide to calculate singlet-singlet (S→S) or singlet-triplet (S→T) excitation or both types of transitions
- for oscillator strength calculations the dipole moments should be calculated as well
- how many levels of the vertical excitation energies need to be calculated?
- depending on the desired accuracy one could involve cutoffs for the core levels and/or the unoccupied levels.

Some useful notes for TDDFT calculations, before the initial run:

Normally the calculation of TDDFT system with heavy atoms and with large basis sets is time and memory consuming. It is advisable to calculate such a system on machines with sufficient amount of memory. The necessary integrals can be stored and used for further calculations, e. g. if one wants to calculate the same system, but only valence electron transitions, or to calculate singlet-triplet transitions in additional.

One should check the exchange-correlation potential for TDDFT. It is possible to use one exchange-correlation potential for the SCF and another for the TDDFT part of the calculation. One should be careful!

The initial PARAGAUSS run

Choose a suitable version of PARAGAUSS, build a suitable input file according to the rules of PARAGAUSS.

Command line parameters relevant for response calculations: `[ -datadir <dir> ]`. The results can be found in the output directory.

Examples: Au calculation, symmetry I_h, open shell; Au_2 calculations, symmetry D_{8h}, closed-shell S→S and S→T transitions, H_2O calculation, symmetry C_{2v}, closed shell S→S and S→T transitions

Prerequisites:

- A directory with a batch files `samples/script`

- In that directory *inputs* `Au/input, Au2/input, h2o/input`

A suitable batch script then looks like this:

```
opt01:/home/<your dir>> cat script
#!/bin/csh
#$ -cwd
#$ -q short
#$ -pe make 1
cd <work directory>
ttfs_V3.0 $1 -vers V<new version> -mpi -datadir $1.resp
```

It is submitted using the `qsub` command,

```
qsub script Au
```

In general the qsub command takes the following syntax:

```
Usage: qsub [ options ] [ command | -- [ command_args ]] job.name
```

Having submitted the job you can check its status using the `qstat -f` command, which will create an output like this on the screen:

```
opt01 /home/<you dir>> qstat -f
queuename         qtype used/tot. load_avg arch          states
---------------------------------------------------------------
opt01...            BIP   0/1       0.00     lx24-amd64    d
---------------------------------------------------------------
                          ..........
---------------------------------------------------------------
short...            BIP   0/1       0.00     lx24-amd64
################################################################
 - PENDING JOBS - PENDING JOBS - PENDING JOBS - PENDING JOBS
################################################################
17354 0.60500 scriptQ  genest    qw    06/14/2005 11:10:52     6
18078 0.55668 scr2_opt bussai    qw    06/28/2005 16:49:19     2
18090 0.55444 scr2_opt bussai    qw    06/29/2005 09:18:12     2
                             ..........
```

Possible queues on Opteron clusters are as follows:

Queue	Slots	Limit	Purpose
short	1	1 hour	Queue for short jobs. Please use normally not more than 1 slots

opt01 - opt09	2	not limited	Prioritized queue for parallel jobs with up to 4 GB memory
opt10 - opt33	2	not limited	Prioritized queue for parallel jobs with up to 2 GB memory
opt34 - opt39	4	not limited	Prioritized queue for parallel jobs with up to 8 GB memory
quad1 - quad3	4	not limited	Prioritized queue for parallel jobs with up to 16 GB memory
quad4	8	not limited	Prioritized queue for parallel jobs with up to 16 GB memory

After the run the output files are located in the directory `Au` for gold atom and `Au2` for gold molecule, `h2o` for water. In the start directory, in which the batch file `script` is located, now also the files with the redirected standard output and standard error can be found.

Open-shell example: Au atom

A very simple system that one can calculate is an atom, e.g. the Au atom. It is an open-shell system, the system is well studied [122]. We will calculate the system with help of I_h symmetry, but one could choose any other symmetry (C_1, O_h, ... etc).

One of the possible variations of input file is shown on the next table:

&TASKS **TASK = "Response"** **DIPOLE = TRUE** /TASK	In the TASKS part of the input, we choose dipole calculation for the oscillator strength and "Response" for the TDDFT.
&MAIN_OPTIONS **SPIN_RESTRICTED = FALSE** /MAIN_OPTIONS	Here we have a choice to calculate either open shell or closed shell. Let us start with the open shell, later we will calculate closed shell systems.

&SYMMETRY_GROUP **POINT_GROUP = "IH"** /SYMMETRY_GROUP	The point group I_h, better to use the optimal point group of symmetry for each system, it allows to calculate faster and in a very efficient way.
&UNIQUE_ATOM **NAME = "Au"** **Z = 79.0** **N_EQUAL_ATOMS = 1** /UNIQUE_ATOM **0.0 0.0 0.0**	Only one unique atom "Au" is present, it is situated in the center of coordinate system (0.0,0.0,0.0). The nuclear charge is 79.0.
&RESPONSE_CONTROL **TARGET = "SSST"** **XALPHA_RESP = F** **VWN_RESP = F** **BECKEX_RESP = T** **PERDEWC_RESP = T** **noRI = T** **CALC_ALL = F** **CALC_N_LOW = 30** **CALC_OSC_STRENGTH = T** /RESPONSE_CONTROL	Here we want to specify what exactly we need to calculate: in the field target, for example, we can put "SS" for singlet - singlet transition or "ST" for singlet - triplet transitions or "SSST" to calculate both cases (for open shell this field can be omitted), also we will turn on the BP GGA exchange-correlation functionals (BECKEX_RESP and PERDEWC_RESP fields). We will calculate the gold atom without resolution of the identity for exchange-correlation functionals to avoid the numerical instabilities (for more information see Sec. 3.3.4); therefore we set the noRI field to TRUE. We will calculate the first 30 transitions; CALC_ALL is FALSE and CALC_N_LOW equal 30. We want to calculate the oscillator strengths as well; CALC_OSC_STRENGTH is TRUE.

&XC_CONTROL **xc = "bp"** /XC_CONTROL	For the ground state calculation we choose the BP GGA exchange-correlation functional [13, 14].

After finishing the calculations, we obtain **output** and **exc_SS_#irrep.dat** files in our work directory `samples/Au`. The begin of response part of the **output** file is as follows:

```
response_main: main response calculations (START)
  init_start: call df_data_read_header()
  init_start: call df_data_read_header()
    df_data_read_header: read header of interface file...
    TDDFT: HEADER
      *     proceeding open   shell...
      *     IRREPS             =   5
      *     EXCHANGE           = "BECKE"
      *     CORRELATION        = "PERDEW"
      *     MAX_ITER           =    30
      *     CALC_ALL           = FALSE
      *     LANCZOS            = FALSE
      *     noRI               =  TRUE
      *     S_APP              = FALSE
      *     CALC_N_LOW         =    30
      *     MAX_SP_TRANS       =    10
      *     CALC_OSC_STR       =  TRUE
  init_start: call df_data_read_eps_eta()
    dav_solve_main: call Davidson iterative eigensolver...
Iteration   1
Iteration   2
Iteration   3
Iteration   4
    dav_solve_main: after call of DVDSON
       Davidson eigensolver converged:
       Matrix accesses       :  4
       Matrix-Vector products:  65
```

This section of the output file contains the following information: what system we calculated (open-shell system in our case), how many irreducible representations

(irreps) our system has (five), which kind of exchange-correlation functionals do we use for response calculations (BP GGA [13, 14]), and some necessary commands (e.g., CALC_ALL and CALC_OSC_STR), how many transitions we need to calculate (30), etc. Also it contains the information about the calculation, iterations and some eigensolver data.

The output and the files **exc_SS_#irrep.dat** contain the information about transitions:

```
======== EXCITATIONS AND OSCILLATOR STRENGTHS S->S ==========
 SP N SYM  ENERGY INIT  FINA AMPLT OSCSTR   OSCX   ...  DELTA
            [eV]                    [au]    [au]         [eV]
 B  1  AG  6.1614 6AG   7AG   0.99 0.0000 0.0000       6.2093
 B  1  AG         6AG   8AG  -0.11                     6.7136
 A  1  AG         3HG   4HG  -0.01                    10.0548
 B  1  AG         3HG   4HG   0.01                    10.0847
 B  1  AG         3HG   5HG   0.01                    19.3564
 A  1  AG         3HG   5HG  -0.01                    19.6716
 B  1  AG         6AG   9AG  -0.01                     8.4445
 A  1  AG         3HG   6HG   0.00                    50.2848
 B  1  AG         3HG   6HG   0.00                    49.9864
 B  1  AG        4T1U  5T1U   0.00                    59.3133
===
 B  2  AG  6.6719 6AG   8AG  -0.99 0.0000 0.0000       6.7136
 B  2  AG         6AG   7AG  -0.11                     6.2093
 A  2  AG         3HG   4HG   0.02                    10.0548
 B  2  AG         3HG   4HG  -0.02                    10.0847
 B  2  AG         3HG   5HG  -0.01                    19.3564
 A  2  AG         3HG   5HG   0.01                    19.6716
 B  2  AG         6AG   9AG  -0.01                     8.4445
 B  2  AG         3HG   6HG   0.00                    49.9864
 A  2  AG         3HG   6HG   0.00                    50.2848
 B  2  AG        4T1U  5T1U   0.00                    59.3133
...
```

Here **SP** refers to the spin (A or B), for the closed-shell calculation spin is only A. **N** is the number of the transition, in the case of our input for Au atom the number will be from 1 to 30. **SYM** is the symmetry term of the final state. **ENERGY** is the transition energy given in eV. **INIT** and **FINA** refers to the transition irreps and the indices of orbitals, transition goes from **INIT**(initial) to **FINA**(final). **AMPLT**(amplitude) is the eigenvectors, it refers to the contributions of the different transitions to corresponding energy. The quantities **OSCSTR**, **OSCX**, **OSCY**, **OSCZ** are the oscillator strengths and the X, Y and Z contributions to the oscillator strength, respectively. **DELTA** is the

exact difference between the energy of the target orbital and the source orbital, it was implemented mostly for debugging, but it is sometimes useful.

The eigensolver finds the solution of the eigenvalue problem,

$$Ax_i = \lambda_i x_i, \tag{G.1}$$

where λ_i are a few of the lowest or highest (optional) eigenvalues of matrix A, and x_i their corresponding eigenvectors.

The Davidson eigensolver provides an iterative solution [48,49,51]:

```
     Eigenvalues          Eigval Differences       Residuals
0.512683121683425D-01     0.3865033293D-12     0.5919909716D-06
0.601155754186356D-01     0.1448841047D-13     0.9477959485D-06
0.957791792117141D-01     0.3474720511D-12     0.1528327442D-05
0.132130325552504D+00     0.7202849428D-12     0.1022594699D-03
0.162329702998792D+00     0.9872935802D-12     0.1746734014D-03
0.468099075147801D+00     0.2132183319D-12     0.6274785392D-06
0.776733552973428D+00     0.1698641228D-12     0.1566062548D-04
  ...
```

The relevant information for deciding if and how well the iteration converged one can find in the output file. One sees here each **eigenvalue** λ_i and the **eigenvalues difference** $||x_i^{(j)} - x_i^{(j-1)}||$ which is an unbiased measure of the eigenvector convergence. The second measure is provided by the **residuals,**

$$||Res(x_i^{(j)})|| \simeq ||A - \lambda_i|| \, ||x_i^{(j)} - x_i||. \tag{G.2}$$

The residual norm is a useful convergence criterion, but it does not measure the relative error.

The strategies of convergence will be explained below.

Closed-shell examples: Au_2 and H_2O molecules

As another example we discuss the Au_2 molecule. It is a closed-shell system. For Au_2 we will use the point group D_{8h}. The system is also well studied [123].

&MAIN_OPTIONS **SPIN_RESTRICTED = TRUE** /MAIN_OPTIONS	The field SPIN_RESTRICTED is TRUE. We will calculate a closed-shell system.

&SYMMETRY_GROUP **POINT_GROUP = "D8H"** /SYMMETRY_GROUP	The point group symmetry is D_{8h}.
&UNIQUE_ATOM **NAME = "Au"** **Z = 79.0** **N_EQUAL_ATOMS = 2** /UNIQUE_ATOM **0.0 0.0 2.382**	We have to put only one Au atom, the second will be generated according to the symmetry rules.
&RESPONSE_CONTROL **TARGET = "SSST"** /RESPONSE_CONTROL	Here it is important to set the TARGET field. In our case we want to calculate both type of transitions (S→S and S→T). By default we will calculate only S→S transitions.

When the calculation is finished, we obtain the files **output, exc_SS_** or **exc_ST_#irrep.dat** in our work directory `samples/Au2`.

The output will contain not only S→S transitions, but also S→T transitions. The different transitions will be separated as follows:

```
======== EXCITATIONS AND OSCILLATOR STRENGTHS S->S ========
 ......
======== EXCITATIONS AND OSCILLATOR STRENGTHS S->T ========
 ......
```

Another example which can be found in example suite is the molecule H_2O. The geometry of H_2O, was taken from Ref. [124]. H_2O is a closed-shell system and the point group symmetry of a water molecule is C_{2v}. All TDDFT fields in the input file can be chosen as for Au_2.

How to avoid problems and carry out TDDFT calculations in an efficient way

In this section we will describe the strategy of stability and efficiency. Also we will summarize our own experience with TDDFT calculations and try to answer common questions, which could be very helpful when starting TDDFT calculations.

What should I do if the eigensolver did not converge?

First of all, one should check the **eigval difference** (most important) and the **residuals**. According to those data one could analyze how close the eigenvalues are to the expected precision. If one puts the **eigensolver_criterion** to 10^{-7} a.u. but some eigenvalues converged to 10^{-5} a.u, it could be also a good convergency for almost all tasks.

Another possibility for saving time is to introduce a cutoff of occupied and unoccupied orbitals. Normally the core electrons do not affect much the excitations of the valence electrons, see Sec. 3.5, but is prudent to test the influence of the cutoff for each target system first. If one can exclude the core electrons and possibly high unoccupied orbitals without much influence on the results, the convergence may improve and the calculations will be faster and more efficient.

The last possibility is to increase the number of iterations for the eigensolver.

What should I do if I observe numerical instability?

During our work with TDDFT code we found two reasons of numerical instability. First, it is the numerical instability due to the fitting basis set. PARAGAUSS uses the same fitting basis set for SCF calculations and for TDDFT calculations. Symmetry calculations in TDDFT are very sensitive to the fitting basis set. A large fitting basis set could cause a numerical instability. Reasons are not fully clarified yet.

A second reason for numerical instability is the usage of the resolution of the identity for the exchange-correlation kernel, see Section 3.1.1. It is not always possible to rely on TDDFT results obtained with the resolution of the identity (RI-TDDFT), see Section 3.1.1. For extended system we observed artifacts resulting in unstable or even imaginary transition energies when applying the RI-TDDFT method. We were motivated to implement an accurate numerical quadrature scheme for the exchange-correlation response kernel, see Section 3.3.4. This approach avoids the usage of an auxiliary basis set and the results become numerically stable. To avoid such a numerical instabilities it is necessary to set the “noRI” field to “TRUE”.

How can I construct the appropriate fit basis?

Unfortunately, there is no universal recipe for creating an appropriate fitting basis, which will allow one to avoid numerical instabilities for all systems. Therefore, we normally use the procedure which was explained in Ref. [11]. This procedure is used for normal PARAGAUSS calculations and it can be used for TDDFT calculations as well. The scheme is as follows:

- The exponents for the $s(r^2)$-type functions are obtained by multiplying the $s(p)$-type exponents of the orbital basis by a factor of 2.
- The exponents for the p-type polarization functions are taken as geometric sequence $a_n = q^n a_0$ with $q = 2.5$ and $a_0 = \lambda \cdot 0.04$, where the scaling factor λ is used to model the contraction of the electron density with increasing nuclear charge Z. For carbon $\lambda_C = 1.0$ was chosen, and for other atoms X

$$\lambda_X = \lambda_C \cdot (\frac{r_s(C)}{r_s(X)})^2$$

  was used, where $r_s(C)$ and $r_s(X)$ are the effective atomic radii determined by J. Slater [125].
- Finally, the d-type exponents are obtained by simply doubling the p-type exponents.

The problem of auxiliary basis sets deserves to be investigated further.

PARAGAUSS input for TDDFT

The TASK field:

NAME	DEFAULT VALUE	DESCRIPTION
TASK	"Response"	Calculate response
DIPOLE	TRUE	Need to be TRUE for dipole calculations, the dipoles are necessary for oscillator strengths

The RESPONSE field:

NAME	DEFAULT VALUE	DESCRIPTION

TARGET	"SS"	only need to be specified for closed shell: SS, ST or SSST transition
XALPHA_RESP	TRUE	EXCHANGE = X_α
VWN_RESP	FALSE	CORRELATION = VWN
BECKEX_RESP	FALSE	EXCHANGE = BECKE
PERDEWC_RESP	FALSE	CORRELATION = PERDEW
PW91X_RESP	FALSE	EXCHANGE = PW91
PW91C_RESP	FALSE	CORRELATION = PW91
PBEX_RESP	FALSE	EXCHANGE = PBE
PBEC_RESP	FALSE	CORRELATION = PBE
REVPBEX_RESP	FALSE	EXCHANGE = PBEN
PBENX_RESP	FALSE	EXCHANGE = revPBE
PW_LDAC_RESP	FALSE	CORRELATION = PW(LDA)
CALC_ALL	FALSE	if TRUE all transitions will be calculated
LANCZOS	FALSE	if TRUE the Lanczos eigensolver procedure will be started instead of Davidson (**be careful, the options did not tested properly**)
SAVED_XC	FALSE	if TRUE the program will take the exchange correlation integrals which were stored previously
SAVED_2C_Q	FALSE	The same as for SAVED_XC, but for two-center Coulomb integrals
SAVED_3C_Q	FALSE	The same as for SAVED_XC, but for three-center Coulomb integrals
noRI	FALSE	if TRUE it will turn the resolution of identity procedure for XC integrals off

S_APP	FALSE	if TRUE it will turn the simple approximation on (**warning: it is only for debugging!**)
CALC_N_LOW	30	Number of lowest excitations to be calculated
MAX_SP_TRANS	10	the number of single-particle transitions (eigenvectors) to be printed in the output
MAX_ITER	30	Maximal number of iterations in the convergence cycle
CALC_OSC_STRENGTH	FALSE	if TRUE the oscillator strength will be calculated
RHO_CUTOFF	10^{-16}	if the electron density $\rho(r) \leq$RHO_CUTOFF then $f_{\mathrm{XC}}[\rho(r)] := 0$
EIGENSOLVE_CRITERION	10^{-16}	convergence criterion for eigensolver
UNOCCUPIED_LEVEL_CRITERION	10^{-10}	If fractional charges η are allowed for single MO orbitals, in this case the response module uses $\eta_0$criterion in such a way (occupation): fully: $\eta \geq 2 - \eta_0$ partially: $\eta_0 < \eta < 2 - \eta_0$ empty: $\eta \leq \eta_0$
LIMIT_UNOCCUPIED_LEVELS	FALSE	if TRUE then only a "lower part" of the MO spectrum will be used for calculating the integrals
MAX_LEVEL_INDEX	-1	the index of the largest allowed virtual orbital
MIN_LEVEL_ENERGY	-10^3	the lowest allowed orbital energy in eV (considered only if MAX_LEVEL_INDEX = -1)
MAX_LEVEL_ENERGY	10^3	the largest allowed orbital energy in eV (considered only if MAX_LEVEL_INDEX = -1)
NUM_SPECTRUM_LEVELS	300	The number of levels can be adjusted by this parameter

Appendix H

Basis sets

Table H.1: Orbital basis of Cu (Z=29) (16s,13p,7d)
Reference: s, p, d [87]
Contraction: (16s13p7d $\rightarrow$ 7s5p4d)

	s	p	d
α_1	0.012237	0.021537	0.042600
α_2	0.040791	0.046199	0.149100
α_3	0.113303	0.099100	0.528322
α_4	0.330500	0.265000	1.727430
α_5	0.964080	0.711445	5.103920
α_6	2.578480	1.906670	15.074700
α_7	9.393570	4.693820	53.647800
α_8	22.298300	11.743500	
α_9	67.359100	27.055100	
α_{10}	158.399000	65.323900	
α_{11}	395.099000	172.195000	
α_{12}	1071.970000	532.106000	
α_{13}	3239.820000	2245.290000	
α_{14}	11373.400000		
α_{15}	50072.900000		
α_{16}	337200.000000		

Table H.2: Orbital basis of Ag (Z=47) (19s15p9d)
Reference: s, p, d [88]
Contraction: (19s15p9d →8s6p5d)

	s	p	d
α_1	0.014877	0.012615	0.110795
α_2	0.041876	0.032649	0.288070
α_3	0.117872	0.084500	0.836802
α_4	0.237900	0.218700	2.133270
α_5	0.480114	0.565839	5.101889
α_6	1.094527	1.464069	11.892642
α_7	2.137443	3.394228	28.986678
α_8	5.641230	7.419325	77.125699
α_9	11.102996	15.808571	260.669120
α_{10}	30.194935	34.255544	
α_{11}	67.292480	74.964904	
α_{12}	173.467880	175.506230	
α_{13}	393.966470	458.347310	
α_{14}	954.427580	1426.664200	
α_{15}	2531.374300	6116.674200	
α_{16}	7559.239300		
α_{17}	26465.705000		
α_{18}	116697.350000		
α_{19}	782615.550000		

Table H.3: Orbital basis of Au (Z=79) ($22s20p11d7f$)
Reference: s, p, d, f [89]
Contraction: ($22s20p11d7f \rightarrow 9s7p6d4f$)

	s	p	d	f
α_1	0.004545	0.001644	0.560000	0.170000
α_2	0.010000	0.003781	0.140000	0.420000
α_3	0.022000	0.008696	0.350000	1.100000
α_4	0.056000	0.020000	0.880000	3.338172
α_5	0.140000	0.046000	2.200000	9.912050
α_6	0.340000	0.100000	5.546597	27.750359
α_7	0.840000	0.210000	14.003830	86.824371
α_8	2.100000	0.455000	36.861912	
α_9	5.153470	1.000000	90.5377960	
α_{10}	13.352700	2.250000	243.203201	
α_{11}	26.245510	4.956507	816.721557	
α_{12}	58.480511	10.799290		
α_{13}	113.614098	26.133190		
α_{14}	233.439102	55.268070		
α_{15}	621.276978	127.800003		
α_{16}	1429.497930	285.456513		
α_{17}	3491.379880	677.790772		
α_{18}	9358.392580	1773.843990		
α_{19}	28274.941400	54591.240200		
α_{20}	99928.789100	23072.800800		
α_{21}	446529.500000			
α_{22}	3095417.000000			

Table H.4: Orbital basis of O (Z=8) ($13s8p1d$)
Reference: s, p, d [30]
Contraction: ($13s8p1d \rightarrow 6s5p1d$)

	s	p	d
α_1	0.028000	0.016000	0.350000
α_2	0.055000	0.035000	
α_3	0.107685	0.074345	
α_4	0.366937	0.236822	
α_5	1.140320	0.747159	
α_6	2.431070	2.337090	
α_7	5.182860	7.914690	
α_8	13.672800	35.296900	
α_9	37.635700		
α_{10}	113.263000		
α_{11}	394.270000		
α_{12}	1723.170000		
α_{13}	11496.600000		

Table H.5: Orbital basis of Mg (Z=12) (15s10p1d)
Reference: s, p, d [30]
Contraction: (15s10p1d →6s5p1d)

	s	p	d
α_1	0.025820	0.038910	0.293000
α_2	0.059280	0.090400	
α_3	0.136120	0.210050	
α_4	0.284090	0.488050	
α_5	0.592910	1.304830	
α_6	1.526710	3.500190	
α_7	4.089940	9.441500	
α_8	9.937210	26.175400	
α_9	28.131900	80.877000	
α_{10}	79.727200	337.610000	
α_{11}	236.710000		
α_{12}	727.345000		
α_{13}	2005.820000		
α_{14}	6406.130000		
α_{15}	39283.400000		

Bibliography

[1] L. A. Peysler, A. E. Vinson, A. P. Bartko, and R. M. Dickson, Science **291**, 103 (2001).

[2] C. Mayer, R. Palkovits, G. Bauer, and T. Schalkhammer, J. Nanoparticle Res. **3**, 361 (2001).

[3] U. Kreibig and M. Vollmer, *Optical Properties of Metal Clusters* (Springer, Berlin, 1995).

[4] M. Haruta, N. Yamada, T. Kobayashi, and S. Iijima, S. J. Catal. **115**, 301 (1989).

[5] J. P. Wilcoxon and B. L. Abrams, Chem. Soc. Rev. **35**, 1162 (2006).

[6] E. Hutter and J. H. Fendler, Adv. Mater. **16**, 1685 (2004).

[7] M. A. L. Marques and E. K. U. Gross, Annu. Rev. Phys. Chem. **55**, 427 (2004).

[8] E. Runge and E. K. U. Gross, Phys. Rev. Lett. **52**, 997 (1984).

[9] M. E. Casida, in *Recent Developments and Applications of Modern Density Functional Theory*, edited by J. M. Seminario (Elsevier, Amsterdam, 1996), Vol. 4, pp. 391–439.

[10] M. A. L. Marques and E. K. U. Gross, in *A Primer in Density Functional Theory, Lecture Notes in Physics*, edited by C. Fiolhais, F. Nogueira, and M. A. L. Marques (Springer, Berlin, 2003), Vol. 620, pp. 144–184.

[11] H. Heinze, Dissertation, Technische Universität München, 2000.

[12] E. Gross, J. Dobson, and M. Petersilka, in *Topics in Current Chemistry*, edited by R. Nalewajski (Springer-Verlag, Berlin, Heidelberg, 1996), Vol. 181, Chap. 2, p. 81.

[13] A. D. Becke, Phys. Rev. B **38**, 3098 (1988).

[14] J. P. Perdew, Phys. Rev. B **33**, 8822 (1986).

[15] J. P. Perdew, J. A. Chevary, S. H. Vosko, K. A. Jackson, M. R. Pederson, D. J. Singh, and C. Fiolhais, Phys. Rev. B **46**, 6671 (1992).

[16] J. P. Perdew and Y. Wang, Phys. Rev. B **45**, 13244 (1992).

[17] J. P. Perdew, K. Burke, and M. Ernzernhof, Phys. Rev. Lett. **77**, 3865 (1996).

[18] Y. Zhang and W. Yang, Phys. Rev. Lett. **88**, 890 (1998).

[19] B. Hammer, L. B. Hansen, and J. K. Norskov, Phys. Rev. B **59**, 7413 (1999).

[20] R. G. Parr and W. Yang, *Density Functional Theory of Atoms and Molecules* (Oxford University Press, New York, 1989).

[21] S. H. Vosko, L. Wilk, and M. Nusair, Can. J. Phys. **58**, 1200 (1980).

[22] T. Belling, T. Grauschopf, S. Krüger, F. Nörtemann, M. Staufer, M. Mayer, V. A. Nasluzov, U. Birkenheuer, A. Hu, A. V. Matveev, A. V. Shor, M. S. K. Fuchs-Rohr, K. M. Neyman, D. I. Ganyushin, T. Kerdcharoen, A. Woiterski, S. Majumder, and N. Rösch, PARAGAUSS, Version 3.1, Technische Universität München, 2006.

[23] M. Mayer, Dissertation, Technische Universität München, 1999.

[24] A. V. Matveev, Dissertation, Technische Universität München, 2003.

[25] A. V. Matveev, M. Mayer, and N. Rösch, Comp. Phys. Comm. **160**, 91 (2004).

[26] E. J. Baerends, D. E. Ellis, and P. Ros, Chem. Phys. **2**, 41 (1973).

[27] R. Ahlrichs, M. Bär, M. Häser, H. Horn, and C. Kölmel, Chem. Phys. Lett. **162**, 165 (1989).

[28] G. Fronzoni, R. D. Francesco, M. Stener, and P. Decleva, J. Chem. Phys. **126**, 134308 (2007).

[29] G. Fronzoni, M. Stener, P. Decleva, F. Wang, T. Ziegler, E. van Lenthe, and E. J. Baerends, Chem. Phys. Lett. **416**, 56 (2005).

[30] K. M. Neyman, C. Inntam, V. A. Nasluzov, R. Kosarev, and N. Rösch, Appl. Phys. A **78**, 823 (2004).

[31] K. M. Neyman, C. Inntam, A. V. Matveev, V. A. Nasluzov, and N. Rösch, J. Am. Chem. Soc. **127**, 11652 (2005).

[32] C. Inntam, L. V. Moskaleva, K. M. Neyman, V. A. Nasluzov, and N. Rösch, Appl. Phys. A **13**, 277 (2006).

[33] C. Inntam, L. V. Moskaleva, I. V. Yudanov, K. M. Neyman, and N. Rösch, Chem. Phys. Lett. **417**, 515 (2006).

[34] K. M. Neyman, C. Inntam, L. V. Moskaleva, and N. Rösch, Chem. Eur. J. **13**, 277 (2006).

[35] I. N. Levine, *Quantum Chemistry* (Prentice Hall, Englewood Cliffs, New Jersey, 1991).

[36] L. S. Pontryagin, *Ordinary Differential Equations* (Addison-Wesley, Reading, MA, 1962).

[37] A. Görling, Phys. Rev. A **55**, 2630 (1997).

[38] K. Yoshida, *Functional Analysis* (Springer, Berlin, New York, 1995).

[39] L. D. Landau and E. M. Lifshitz, *Mechanics and Electrodynamics* (Elsevier, Amsterdam, 1972).

[40] R. W. Ditchburn, *Light, 3rd ed.* (Academic, New York, 1976).

[41] A. Corney, *Atomic and Laser Spectroscopy* (Clarendon, Oxford, 1977).

[42] R. C. Hilborn, Am. J. Phys. **50**, 982 (1982).

[43] J. Q. Chen, J. Ping, and F. Wang, *Group Representation Theory for Physicists* (World Scientific Publishing, Singapore, 2002).

[44] C. V. Alsenoy, J. Comp. Chem. **9**, 620 (1988).

[45] R. A. Kendall and H. A. Früchtl, Theor. Chem. Acc. **97**, 158 (1997).

[46] A. Görling, H. H. Heinze, S. P. Ruzankin, M. Staufer, and N. Rösch, J. Chem. Phys. **110**, 2785 (1999).

[47] H. H. Heinze, A. Görling, and N. Rösch, J. Chem. Phys. **113**, 2088 (2000).

[48] E. R. Davidson, J. Comput. Phys. **17**, 87 (1975).

[49] E. R. Davidson, Comput. Phys. Comm. **53**, 49 (1989).

[50] R. B. Morgan and D. S. Scott, SIAM J. Sci. Comp. **14**, 585 (1993).

[51] A. Stathopoulos and C. Fischer, Comput. Phys. Comm. **79**, 268 (1994).

[52] T. Belling, Dissertation, Technische Universität München, 1998.

[53] M. Staufer, Dissertation, Technische Universität München, 1999.

[54] A. Görling, Dissertation, Technische Universität München, 1990.

[55] R. Bauernschmitt and R. Ahlrichs, Chem. Phys. Lett. **256**, 454 (1996).

[56] BLAS: Basic Linear Algebra Subprogramm, University of Tennessee, Oak Ridge National Laboratory, Numerical Algorithms Group Ltd, 1997.

[57] V. I. Lebedev, Sib. Math. J. **18**, 99 (1977).

[58] G. L. Oliver and J. P. Perdew, Phys. Rev. A **20**, 397 (1979).

[59] M. Rasolt and D. J. W. Geldart, Phys. Rev. B **34**, 1325 (1986).

[60] J. C. Slater, Phys. Rev. **81**, 385 (1951).

[61] P. Hohenberg and W. Kohn, Phys. Rev. **136**, B864 (1964).

[62] W. Kohn and L. J. Sham, Phys. Rev. **140**, A1133 (1965).

[63] R. van Leeuwen and E. J. Baerends, Phys. Rev. A **49**, 2421 (1994).

[64] E. van Lenthe E. J. Baerends, J. Comput. Chem. **24**, 1142 (2003).

[65] J. Haase and M. Winnewisser, Z. Naturforsch. **23a**, 61 (1968).

[66] R. W. G. Wycoff, *Crystal Structures* (Interscience, New York, 1964).

[67] N. Rösch, G. N. Vayssilov, and K. M. Neyman, in *Host/Guest Systems Based on Nanoporous Crystals*, edited by F. Laeri, F. Schüth, U. Simon, and M. Wark (Wiley-VCH, Weinheim, 2003), pp. 339–350.

[68] N. Rösch, V. A. Nasluzov, K. M. Neyman, G. Pacchioni, and G. N. Vayssilov, in *Theoretical and Computational Chemistry Series*, edited by J. Leszczynski (Elsevier, Amsterdam, 2004), Vol. 15, pp. 367–450.

[69] K. M. Neyman, G. N. Vayssilov, and N. Rösch, J. Organomet. Chem. **689**, 4384 (2004).

[70] J. Guzman and B. C. Gates, Dalton. Trans. 3303 (2003).

[71] G. Pacchioni, in *Nanocatalysis*, edited by U. Heiz and U. Landman (Springer, Amsterdam, 2004), pp. 103–240.

[72] U. Heiz and W.-D. Schneider, J. Phys. D **33**, R85 (2000).

[73] *Nanocatalysis*, edited by U. Heiz and U. Landman (Springer, Amsterdam, 2004).

[74] C. D. Valentin, A. Scagnelli, G. Pacchioni, T. Risse, and H.-J. Freund, Surf. Sci. **600**, 2434 (2006).

[75] M. Yulikov, M. Sterrer, M. Heyde, H.-P. Rust, T. Risse, H.-J. Freund, G. Pacchioni, and A. Scagnelli, Phys. Rev. Lett. **96**, 146804:1 (2006).

[76] C. Kohl, F. Calvayrac, P.-G. Reinhard, and E. Suraud, Surf. Sci. **405**, 74 (1998).

[77] A. D. Vitto, C. Sousa, F. Illas, and G. Pacchioni, J. Chem. Phys. **121**, 7457 (2004).

[78] M. Walter and H. Häkkinen, Phys. Rev. B **72**, 205440:1 (2005).

[79] J.-M. Antonietti, M. Michalski, U. Heiz, J. Jones, K. H. Lim, N. Rösch, A. D. Vitto, and G. Pacchioni, Phys. Rev. Lett. **94**, 213402 1 (2005).

[80] A. D. Vitto, G. Pacchioni, K. H. Lim, N. Rösch, J.-M. Antonietti, M. Michalski, U. Heiz, and J. Jones, J. Phys. Chem. B **109**, 19876 (2005).

[81] S. Gilb, K. Jacobson, D. Schoos, F. Furche, R. Ahlrics, and M. M. Kappes, J. Chem. Phys. **16**, 4619 (2004).

[82] M. A. L. Marques, C. A. Ullrich, F. Nogueira, A. Rubio, K. Burke, and E. K. U. Gross, *Time-Dependent Density Functional Theory, Lecture Notes in Physics* (Springer, Berlin, 2006), Vol. 706.

[83] T. Belling, T. Grauschopf, S. Krüger, M. Mayer, F. Nörtemann, M. Staufer, C. Zenger, and N. Rösch, in *Lecture Notes in Computational Science and Engineering*, edited by H.-J. Bungartz, F. Durst, and C. Zenger (Springer, Heidelberg, 1999), Vol. 8, pp. 441–455.

[84] B. I. Dunlap and N. Rösch, Adv. Quant. Chem. **21**, 317 (1990).

[85] O. D. Häberlen and N. Rösch, Chem. Phys. Lett. **199**, 491 (1992).

[86] N. Rösch, A. V. Matveev, V. A. Nasluzov, K. M. Neyman, L. V. Moskaleva, and S. Krüger, in *Theoretical and Computational Chemistry Series*, edited by P. Schwerdtfeger (Elsevier, Amsterdam, 2004), Vol. 14, pp. 656–722.

[87] A. J. Wachter, J. Chem. Phys. **52**, 1033 (1970).

[88] R. Poirer, R. Kari, and I. G. Csizimadia, *Handbook of Gaussian Basis Sets* (Elsevier, Amsterdam, 1985).

[89] B. Hess. Private communication to N. Rösch.

[90] A. D. Becke, J. Chem. Phys. **88**, 2547 (1988).

[91] V. A. Nasluzov, V. V. Rivanenkov, A. B. Gordienko, K. M. Neyman, U. Birkenheuer, and N. Rösch, J. Chem. Phys. **115**, 8157 (2001).

[92] V. A. Nasluzov, V. V. Rivanenkov, V. V. Shor, K. M. Neyman, U. Birkenheuer, and N. Rösch, Int. J. Quantum Chem. **90**, 386 (2002).

[93] R. L. Martin, J. Chem. Phys. **118**, 4775 (2003).

[94] A. T. Amos and G. G. Hall, Proc. Roy. Soc. **A263**, 483 (1961).

[95] I. Yudanov, G. Pacchioni, K. M. Neyman, and N. Rösch, J. Phys. Chem. B **101**, 2786 (1997).

[96] K. M. Neyman, S. Vent, G. Pacchioni, and N. Rösch, Nuovo Cim. D **19**, 1743 (1997).

[97] A. M. Ferrari, C. Xiao, K. M. Neyman, G. Pacchioni, and N. Rösch, Phys. Chem. Chem. Phys. **1**, 4655 (1999).

[98] V. Musolino, A. Seloni, and R. Car, Phys. Rev. Lett. **83**, 3242 (1999).

[99] A. Bogicevic and D. R. Jennison, Surf. Sci. **437**, L741 (1999).

[100] A. Bogicevic and D. R. Jennison, Surf. Sci. **515**, L481 (2002).

[101] R. Coquet, G. J. Hutchings, S. H. Taylor, and D. J. Willock, J. Mater. Chem. **16**, 1978 (2006).

[102] R. Barnett and U. Landman, Phys. Rev. B **48**, 2081 (1993).

[103] C. E. Moore, *Atomic Energy Levels* (National Bureau of Standards Reference Data Series, U.S. GPO: Washington DC, 1952), Vol. II and III, reprint of NBS Circular No. 467.

[104] J. C. Pickerling and V. Zillio, Eur. Phys. J. D **13**, 181 (2001).

[105] L. Tjeng, A. Vos, and G. Sawatzky, Surf. Sci. **235**, 269 (1990).

[106] P. Pyykkö, Chem. Rev. **88**, 563 (1988).

[107] C. N. Berglund and W. E. Spicer, Phys. Rev. **136**, A1044 (1964).

[108] C. Pampuch, O. Rader, T. Kachel, W. Gudat, C. Carbone, R. Kläsges, G. Bihlmayer, S. Blügel, and W. Eberhardt, Phys. Rev. Lett. **85**, 2561 (2000).

[109] C. Lee, W. Yang, and R. G. Parr, Phys. Rev. B **37**, 785 (1988).

[110] A. V. Matveev, K. M. Neyman, I. V. Yudanov, and N. Rösch, Surf. Sci. **426**, 123 (1999).

[111] T. A. Albright, J. K. Burdett, and M.-H. Whangbo, *Orbital Interactions in Chemistry* (Wiley, New York, 1985).

[112] M. D. Morse, Chem. Rev. **86**, 1049 (1986).

[113] M. Witko and H. O. Beckmann, Mol. Phys. **86**, 945 (1982).

[114] K. K. Das and K. Balasubramanian, J. Mol. Spectrosc. **140**, 280 (1990).

[115] J. Lochet, J. Phys. B **11**, L55 (1978).

[116] J. G. McCeffrey, R. R. Bennett, M. D. Morse, and W. H. Breckenridge, J. Chem. Phys. **91**, 91 (1989).

[117] R. H. Page and C. S. Gudeman, J. Chem. Phys. **94**, 39 (1991).

[118] L. L. Ames and R. F. Barrow, Trans. Farad. Soc. **63**, 39 (1967).

[119] B. Simard and P. A. Nackett, J. Mol. Spectrosc. **142**, 310 (1990).

[120] V. Bonacic-Koutecky, J. Pittner, and J. Boiron, J. Chem. Phys. **110**, 3876 (1999).

[121] V. Beutel, H.-G. Krämer, G. L. Bhale, M. Kuhn, K. Weyers, and W. Demtröder, J. Chem. Phys. **98**, 2699 (1993).

[122] C. E. Moore, *Atomic Energy Levels* (Natl. Bur. Stand., Washington, DC, 1952), Vol. II-III, p. 35.

[123] X. Wang, X. Wan, H. Zhou, S. Takami, M. Kubo, and A. Miyamoto, J. Mol. Struct. (Theochem) **579**, 221 (2002).

[124] H. Sekino and R. J. Bartlett, J. Chem. Phys. **85**, 976 (1986).

[125] J. C. Slater, Phys. Rev. **36**, 57 (1930).